Technische Universität München
Fakultät für Physik

Max-Planck-Institut für Astrophysik

The Study of Gravitational Waves from Three-Dimensional Simulations of Core-Collapse Supernovae

Haakon Andresen

Vollständiger Abdruck der von der Fakultät für Physik der Technischen Universität München zur Erlangung des akademischen Grades eines

Doktors der Naturwissenschaften (Dr. rer. nat.)

genehmigten Dissertation.

Vorsitzender:		Prof. Dr. Lothar Oberauer
Prüfer der Dissertation:	1.	Apl. Prof. Dr. Ewald Müller
	2.	Prof. Dr. Björn Garbrecht

Die Dissertation wurde am 08.03.2017 bei der Technischen Universität München eingereicht und durch die Fakultät für Physik am 15.05.2017 angenommen.

Contents

1. Introduction **1**

2. Gravitational waves in a nutshell **3**
2.1. Linearised theory 3
2.2. The transverse-traceless gauge 4
2.3. Generation of gravitational waves 6

3. Supernovae **13**
3.1. Classifying supernovae 13
3.2. Iron-core supernovae 14
3.2.1. Shell burning in massive stars 14
3.2.2. Iron-core collapse 15
3.2.3. Shock revival: the neutrino heating mechanism 16
3.3. The post-bounce phase 16
3.3.1. The gain layer, cooling layer, and the three layers of the Proto-neutron star 17
3.3.2. The standing accretion shock instability 18
3.4. Three-dimensional simulations 19

4. Numerical simulations of core-collapse supernovae **21**
4.1. Prometheus 21
4.1.1. Hydrodynamics 22
4.1.2. Equation of state 23
4.1.3. Self gravity - the effective potential 23
4.2. Vertex 24
4.3. Grid setup 25
4.3.1. Spherical polar grid 25
4.3.2. Yin-Yang grid 26

5. Signal analysis **27**
5.1. Fourier analysis 27
5.1.1. Continuous and discrete Fourier transforms 27
5.2. The short-time Fourier transform 28
5.3. The Nyquist frequency and aliasing 28
5.4. The spectral energy density of a discrete time signal 29

6. Gravitational waves from three-dimensional core-collapse simulations 31
6.1. Introduction . . . 31
6.2. Supernova Models . . . 34
6.2.1. Three-dimensional models . . . 34
6.2.2. Two-dimensional models . . . 36
6.3. Structure and origin of the gravitational wave signal . . . 38
6.3.1. Gravitational wave extraction . . . 38
6.3.2. Overview of waveforms . . . 39
6.3.3. Spatial location of underlying hydrodynamical instabilities . . . 42
6.3.4. Origin of high-frequency emission . . . 46
6.3.5. Comparison of high-frequency emission in two and three dimensions 50
6.3.6. Origin of the Low-Frequency Signal . . . 55
6.3.7. Comparison of the exploding and non-exploding 20 solar mass models 61
6.4. Detection prospects . . . 62
6.4.1. General considerations . . . 62
6.4.2. Detection prospects for simulated models . . . 65
6.4.3. Detection prospects with AdvLIGO . . . 66
6.4.4. Detection prospects with the Einstein telescope . . . 66
6.4.5. Interpretation of a prospective detection . . . 67
6.5. Conclusions . . . 68

7. The effects of rotation 73
7.1. Supernova Models . . . 74
7.2. Results . . . 81
7.2.1. Qualitative description of the gravitational wave signals . . . 81
7.3. Excitation of gravitational waves . . . 85
7.4. The standing accretion shock instability, rotation, and resolution . . . 88
7.5. Detection prospects . . . 89
7.6. Core bounce signal . . . 90
7.7. Conclusion and discussion . . . 91

8. Conclusions 95
8.1. Summary and discussion . . . 95
8.2. Uncertainties . . . 97
8.3. Outlook . . . 99

A. List of conventions 101

B. List of acronyms 103

C. Acknowledgements 105

Bibliography 107

1. Introduction

We recently experienced the first direct detection of gravitational waves (Abbott et al., 2016), which marks the beginning of the era of gravitational wave astronomy. Gravitational waves can provide us with unique insights where traditional photon based astronomy fails. An example of such a case is core-collapse supernovae. Electromagnetic radiation created in the core of a massive star during collapse is absorbed by the stellar envelope and we are not able to directly probe the workings of a core with photometric observations. Gravitational waves, and also neutrinos, on the other hand, can propagate freely through the material surrounding the core and could, if detected, provide us with direct information about the nature of core-collapse supernovae.

In this thesis, we will analyse the gravitational wave signals from seven three-dimensional simulations of core-collapse supernovae. The goal is to connect features in the signal to physical processes taking place in the simulations. We will compare the results to those of two-dimensional studies and analyse the differences between previous studies and our results in detail. The main results of this work will be discussed in chapters 6, and 7. Both chapters are led by an introduction that discusses the relevant literature and motivates the work presented in the corresponding chapter. In chapter 6 we study four non-rotating progenitors and focus on the underlying hydrodynamic instabilities responsible for gravitational wave emission, we will also dedicate a large portion of this chapter to discussing the differences between the signals presented in this thesis and those from two-dimensional models found in the literature. Then, in chapter 7 we will discuss how slow to moderate progenitor rotation influences the emission of gravitational waves. In both chapters, we assess the detection prospects of the models.

Before we discuss the gravitational wave signals, we will go through the basics theory of gravitational waves in chapter 2, here we will describe how the gravitational wave signal is extracted from numerical simulations. In chapter 3 we outline the current core-collapse paradigm. The numerical methods used to simulated the models are discussed in chapter 4. Then, in chapter 5 we go through the tools and techniques used to analyse the signal. The next two chapters are dedicated to the actual study of the gravitational waves from the simulations. In the last chapter, we will summarise and discuss the results, before giving a short outlook of the field.

In short, we will attempt to find the complicated answer to the simple question:

What can we learn about the explosion mechanism of core-collapse supernovae from observing the gravitational waves they emit?

2. Gravitational waves in a nutshell

In this chapter we will discuss the theory of gravitational waves (GWs). The derivations largely follow Maggiore (2007).

2.1. Linearised theory

One of the most straightforward ways to understand GWs is to expand the Einstein equations around Minkowski space. Mathematically this means that we write the metric tensor, $g_{\mu\nu}$, as

$$g_{\mu\nu} = \eta_{\mu\nu} + h_{\mu\nu}, \tag{2.1}$$

where $\eta_{\mu\nu}$ is the Minkowski metric tensor and $h_{\mu\nu}$ is some small perturbation satisfying

$$|h_{\mu\nu}| \ll 1. \tag{2.2}$$

The condition given by Eq. 2.2 will not hold in a arbitrary reference frame. Therefore, by imposing the smallness condition on $h_{\mu\nu}$ we implicitly chose a frame where the numerical value of the components of $h_{\mu\nu}$ is much smaller than one, in the region of space which we are interested in. In linearised theory we use the Minkowski metric tensor to lower and raise indices.

The field equations of general relativity can be written in terms of the Ricci tensor, $R_{\mu\nu}$, the Ricci scalar, R, the metric tensor, and the energy-momentum tensor, $T_{\mu\nu}$, as follows

$$R_{\mu\nu} - \frac{1}{2} g_{\mu\nu} R = \frac{8\pi G}{c^4} T_{\mu\nu}. \tag{2.3}$$

Before linerisaing the Einstein equations, by combining Eq. 2.1 and Eq. 2.3, we introduce some simplifying notation. Introducing the quantity

$$h = \eta^{\mu\nu} h_{\mu\nu}, \tag{2.4}$$

and

$$\bar{h}_{\mu\nu} = h_{\mu\nu} - \frac{1}{2} \eta_{\mu\nu} h, \tag{2.5}$$

will allow us to write the equations in a more compact form that is easier to work with. By inserting the expression for the metric tensor (Eq. 2.1) into Eq. 2.3 and expand to linear order in $h_{\mu\nu}$ we find the linearised version of the Einstein equations

$$\partial_\gamma \partial^\gamma \bar{h}_{\mu\nu} + \eta_{\mu\nu} \partial^\rho \partial^\sigma \bar{h}_{\rho\sigma} - \partial^\sigma \partial_\nu \bar{h}_{\mu\sigma} - \partial^\sigma \partial_\mu \bar{h}_{\nu\sigma} = -\frac{16\pi G}{c^4} T_{\mu\nu}. \tag{2.6}$$

We can simplify Eq. 2.6 by using the gauge freedom of linearised theory to impose the Lorentz gauge

$$\partial^\nu \bar{h}_{\mu\nu} = 0. \tag{2.7}$$

Under this gauge condition Eq. 2.6 reduces to a wave equation

$$\partial_\gamma \partial^\gamma \bar{h}_{\mu\nu} = -\frac{16\pi G}{c^4} T_{\mu\nu}, \tag{2.8}$$

since every term, except the first one, on the left hand side vanishes.

Eq. 2.8 further simplifies when we are outside of the sources generating GWs, in vacuum the energy-momentum tensor is zero and we get

$$\partial_\gamma \partial^\gamma \bar{h}_{\mu\nu} = 0, \tag{2.9}$$

which can be rewritten as

$$\frac{1}{c^2} \partial_t^2 \bar{h}_{\mu\nu} = [\partial_x^2 + \partial_y^2 + \partial_z^2] \bar{h}_{\mu\nu}. \tag{2.10}$$

If we compare this expression for $\bar{h}_{\mu\nu}$ to a traditional wave equation, for example that of a sound wave propagating though a fluid or a electromagnetic wave through vacuum, is becomes clear that GWs propagate through spacetime at the speed of light in a wave-like fashion.

2.2. The transverse-traceless gauge

Even though we introduced the Lorentz gauge above, we have not completely removed all non-physical degrees of freedom in the linearised field equations. In vacuum, where the energy-momentum tensor vanishes and Eq. 2.9 holds, it is possible to simplify the expression for $h_{\mu\nu}$. The transverse-traceless gauge (we will denote the transverse-traceless gauge with TT and quantities with a TT are understood to be in the TT-gauge) imposed the following conditions

$$h^{0\mu} = 0, \qquad h^i_i = 0, \qquad \text{and} \qquad \partial^j h_{ij} = 0. \tag{2.11}$$

The solutions to Eq. 2.9 are plane wave solutions and in the TT-gauge the solution for a plane wave propagating along the z-axis is given by

$$h_{ij}^{TT} = \begin{pmatrix} h_+ & h_\times & 0 \\ h_\times & -h_+ & 0 \\ 0 & 0 & 0 \end{pmatrix}_{ij} \cos[\omega(t - z/c)]. \tag{2.12}$$

Here t denotes time, ω the angular frequency of the wave, h_+ denotes the strain of the plus-polarised mode and $h_\times$ is the strain amplitude of the cross-polarised mode. To prove that we can impose Eq. 2.11 we start by realising that the Lorentz gauge does not completely remove all the superfluous degrees of freedom in the theory. Consider the coordinate transformation

$$x^\mu \to x^{'\mu} = x^\mu + \epsilon^\mu, \tag{2.13}$$

where ϵ^μ satisfies $\partial_\gamma \partial^\gamma \epsilon^\mu = 0$, and $|\partial_\nu \epsilon_\mu|$ is at the most on the order of smallness as $|h_{\mu\nu}|$. Under an arbitrary coordinate transformation $x^\mu \to x^{'\mu}(x)$ the second rank tensor $h_{\mu\nu}$ transforms as

$$h_{\mu\nu} \to h'_{\mu\nu} = \frac{\partial x^\gamma}{\partial x'^\mu} \frac{\partial x^\sigma}{\partial x'^\nu} h_{\gamma\sigma}. \tag{2.14}$$

Evaluating Eq. 2.14 for the coordinate transformation given by Eq. 2.13 gives

$$h_{\mu\nu} \to h'_{\mu\nu} = h_{\mu\nu} - (\partial_\mu \epsilon_\nu + \partial_\nu \epsilon_\mu). \tag{2.15}$$

By combining Eq. 2.15 and Eq. 2.5 we find that under Eq. 2.13 $\bar{h}_{\mu\nu}$ transforms as

$$\bar{h}_{\mu\nu} \to \bar{h}'_{\mu\nu} = h_{\mu\nu} - (\partial_\mu \epsilon_\nu + \partial_\nu \epsilon_\mu - \eta_{\mu\nu} \partial_\gamma \epsilon^\gamma). \tag{2.16}$$

By applying ∂_μ to Eq. 2.13 we find

$$\partial_\mu x^{'\mu} = \partial_\mu x^\mu + \partial_\mu \epsilon^\mu. \tag{2.17}$$

Since we have required that $|\partial_\mu \epsilon^\mu| \ll 1$, Eq. 2.17 implies that

$$\partial_\mu x^{'\mu} = \frac{\partial x^{'\mu}}{\partial x^\mu} = 1. \tag{2.18}$$

This means that under the transformation given by Eq. 2.13 the derivatives transform as

$$\partial_\mu \to \partial'_\mu = \partial_\mu. \tag{2.19}$$

We can now calculate how the Lorentz gauge conditions (Eq. 2.7) transform under Eq. 2.13 and we find:

$$\begin{aligned} \partial^\nu \bar{h}_{\mu\nu} &\to (\partial^\nu \bar{h}_{\mu\nu})' \\ &= \partial^\nu \left[\bar{h}_{\mu\nu} - (\partial_\mu \epsilon_\nu + \partial_\nu \epsilon_\mu - \eta_{\mu\nu} \partial_\gamma \epsilon^\gamma) \right] \\ &= \partial^\nu \bar{h}_{\mu\nu} - \partial^\gamma \partial_\gamma \epsilon_\mu = 0. \end{aligned} \tag{2.20}$$

Because we demanded that $\partial_\gamma \partial^\gamma \epsilon^\mu = 0$, we can now directly see that the transformation does not break the Lorentz gauge condition. In other words, we are free to perform the coordinate transformation given by Eq. 2.13.

Instead of thinking about how $\bar{h}_{\mu\nu}$ transforms under Eq. 2.13 we can also construct the functions

$$\epsilon_{\mu\nu} \equiv \partial_\mu \epsilon_\nu + \partial_\nu \epsilon_\mu - \eta_{\mu\nu} \partial_\gamma \epsilon^\gamma \tag{2.21}$$

from our four independent functions ϵ_μ and are free to subtract these functions from $\bar{h}_{\mu\nu}$ without breaking the gauge condition set by Eq. 2.7. The tool we use to impose these four conditions is the coordinate transform given by Eq. 2.13, with the constraints on ϵ_μ and its derivatives specified above. With this freedom, we can now choose the four functions such that they impose four simplifying conditions on $h_{\mu\nu}$. In the TT-gauge the four functions are chosen in such a way that the trace of $\bar{h}_{\mu\nu}$ is zero and $h^{0i} = 0$. Note that if the trace of $\bar{h}_{\mu\nu}$ vanishes $\bar{h}_{\mu\nu} = h_{\mu\nu}$, and we will usually write $h_{\mu\nu}$ instead of $\bar{h}_{\mu\nu}$ when we are in the TT-gauge. These four conditions, together with the Lorentz gauge, define the TT-gauge and result in the conditions given by Eq. 2.11.

2.3. Generation of gravitational waves

We turn now to the generation of gravitational waves. In the linearised theory framework, we start by writing down the solution of Eq. 2.8 for a generic source under the assumption that the gravitational field generated by the source is weak enough to justify the expansion around flat spacetime.

As for any wave equation, the solution of Eq. 2.8 can be found by integrating over the source

$$\bar{h}_{\mu\nu}(t, \mathbf{x}) = \frac{4G}{c^4} \int \mathrm{d}^3 x' \frac{T_{\mu\nu}(t - |\mathbf{x} - \mathbf{x}'|/c)}{|\mathbf{x} - \mathbf{x}'|}. \tag{2.22}$$

Far way from the source at a distance D, if the velocities, v, within the source are small compared to the speed of light, Eq. 2.22 reduces to the famous Einstein quadrupole formula. In the TT-gauge the quadrupole formula can be written as follows

$$h_{\mu\nu}(t, \mathbf{x}) = \frac{1}{D} \frac{4G}{c^4} \left[P_{im} P_{jn} - \frac{1}{2} P_{ij} P_{mn} \right] \ddot{Q}_{ij}(t - d/c), \tag{2.23}$$

where Q_{ij} is the mass quadrupole moment which to leading order in v/c and in Cartesian coordinates is given by

$$Q_{ij} = \int \mathrm{d}^3 x \rho(t, \mathbf{x}) \left[x_i x_j - \frac{1}{3} \delta^{ij} x_l x^l \right]. \tag{2.24}$$

$P_{ij} = \delta_{ij} - \hat{n}_i \hat{n}_j$ is the projection operator onto the plane transverse to the direction the wave is propagating, $\hat{n}_i = x_i / \sqrt{x_j x^j}$. To find the equation describing h_+ and $h_\times$ for a wave propagating in the general direction $\hat{n}$ we first consider a wave propagating along the z-axis in a coordinate system with Cartesian coordinates $(x,\, y,\, z)$ and spherical polar coordinates $(r,\, \theta,\, \phi)$. If $\hat{n} = \hat{z}$ then P_{ij} becomes

$$P_{ij} = \begin{pmatrix} 1 & 0 & 0 \\ 0 & 1 & 0 \\ 0 & 0 & 0 \end{pmatrix}_{ij} , \tag{2.25}$$

and we find that

$$\left[P_{im} P_{jn} - \frac{1}{2} P_{ij} P_{mn} \right] \ddot{Q}_{ij} = \begin{pmatrix} (\ddot{Q}_{11} - \ddot{Q}_{22})/2 & \ddot{Q}_{12} & 0 \\ \ddot{Q}_{21} & (\ddot{Q}_{22} - \ddot{Q}_{11})/2 & 0 \\ 0 & 0 & 0 \end{pmatrix}_{ij} . \tag{2.26}$$

By comparing Eq. 2.12 and Eq. 2.26 we see that

$$\begin{aligned} h_{+}^{TT} &= \frac{G}{c^4 D} (\ddot{Q}_{11} - \ddot{Q}_{22}) \\ h_{\times}^{TT} &= \frac{2G}{c^4 D} \ddot{Q}_{12}. \end{aligned} \tag{2.27}$$

Now consider a wave propagating in the direction given by $\hat{n'} = (\sin\theta \sin\phi,\, \sin\theta\cos\phi,\, \cos\theta)$. We can view this as a wave propagating along the z'-axis of a coordinate system, with axes $(x',\, y',\, z')$, that has been constructed by rotating the original system about the z-axis by an angle ϕ and then about the x-axis by an angle θ. The rotation matrix R of the two consecutive rotations is

$$R = \begin{pmatrix} \cos\phi & \sin\phi & 0 \\ -\sin\phi & \cos\phi & 0 \\ 0 & 0 & 0 \end{pmatrix} \begin{pmatrix} 0 & 0 & 0 \\ 0 & \cos\theta & \sin\theta \\ 0 & -\sin\theta & \cos\theta \end{pmatrix} . \tag{2.28}$$

Since $\hat{n'} = \hat{z'}$ we can use the result from Eq. 2.27, but we have to transform the components of $\ddot{Q}$ from the old system $(x,\, y,\, z)$ into our new coordinate system $(x',\, y',\, z')$. Under the rotations described by Eq. 2.28 the quadrupole moment transforms as follows

$$\ddot{Q}_{ij} \to \ddot{Q}'_{ij} = (RQR^T)_{ij}, \tag{2.29}$$

where R^T denotes the transposed matrix R. After some straightforward, but cumbersome, algebra we arrive at

$$\begin{aligned} h_{+}^{TT} = \frac{G}{c^4 D} \Big[& \ddot{Q}_{11}(\cos^2\phi - \sin^2\phi\cos^2\theta) \\ & + \ddot{Q}_{22}(\sin^2\phi - \cos^2\phi\cos^2\theta) - \ddot{Q}_{33}\sin^2\theta \\ & - \ddot{Q}_{12}(1 + \cos^2\theta) + \ddot{Q}_{13}\sin\phi\sin 2\theta \\ & + \ddot{Q}_{23}\cos\phi\sin 2\theta \Big] \end{aligned} \tag{2.30}$$

and

$$h_{\times}^{TT} = \frac{G}{c^4 D}\Big[(\ddot{Q}_{11} - \ddot{Q}_{22})\sin 2\phi\cos\theta + \ddot{Q}_{12}\cos\theta\cos 2\phi - \ddot{Q}_{13}\cos\phi\sin\theta + 2\ddot{Q}_{23}\sin\phi\sin\theta\Big]. \tag{2.31}$$

Eq. 2.31 and Eq. 2.30 tell us is how the waveforms of the emitted gravitational wave (GW) signal depend on the observers location relative to the source. If we calculate $\ddot{Q}_{ij}$ in a given coordinate system, when dealing with simulations it is often convenient to calculate the quadrupole moment in the coordinate system of the simulations. We can then use Eq. 2.31 and Eq. 2.30 to compute the signal for an observer situated along the direction $\hat{n} = (\sin\theta\sin\phi,\ \sin\theta\cos\phi,\ \cos\theta)$.

In principle, we have all the ingredients we need to calculate the gravitational quadrupole radiation as observed by a distant observer for a slow-moving source. However, we are required to calculate the second time derivative of Q_{ij}. In theory this is not a problem, but when dealing with simulations it is difficult to achieve accurate result when performing direct numerical differentiation of the quadrupole moment. Furthermore, in Eq. 2.24 the terms $\rho x_i x_j \mathrm{d}V$ will give large weight to slow moving low-density fluid elements far away from the regions where GWs are actually produced. On the other hand, the second time derivative of these contributions will be small, because faster moving and the denser matter will contribute more to the GW amplitudes. Again, this is not problematic in theory, but when numerically computing the integral and second-order time derivatives the exact cancellation of the large average value and the rate of change of the quadrupole moment is hard to achieve. We can circumvent these problems by using the Euler equations to rewrite Eq. 2.24. This allows us to eliminate the time derivatives completely and to write the quadrupole moment in terms of quantities which are more closely connected to the regions of the simulation where GWs are produced (Oohara et al., 1997, Finn, 1989, Blanchet et al., 1990).

The standard Euler equations of a self-gravitating fluid are

$$\partial_t\rho + \partial_i(\rho v^i) = 0, \tag{2.32a}$$

$$\partial_t(\rho v^i) + \partial_j(\rho v^i v^j) = -\partial_i p - \rho\partial_i\Phi, \tag{2.32b}$$

$$\partial_t(\rho\varepsilon) + \partial_i(\rho\varepsilon v^i) = -p\partial_i v^i, \tag{2.32c}$$

where p, v^i, ε, and ρ are the pressure, the velocity components, the internal energy density, and the mass density of the fluid, respectively. The Newtonian potential is denoted by Φ, and we have neglected any radiation back-reaction.

Taking the first time derivative of Eq. 2.24 yields

$$\begin{aligned}\frac{\mathrm{d}}{\mathrm{dt}}Q_{ij} &= \frac{\mathrm{d}}{\mathrm{dt}}\int \mathrm{d}^3x\rho\left[x_ix_j - \frac{1}{3}\delta^{ij}x_lx^l\right] \\ &= \int \mathrm{d}^3x\left[x_ix_j - \frac{1}{3}\delta^{ij}x_lx^l\right]\partial_t\rho \\ &= -\int \mathrm{d}^3x\left[x_ix_j - \frac{1}{3}\delta^{ij}x_lx^l\right]\partial_k(\rho v^k), \end{aligned} \tag{2.33}$$

where we used Eq. 2.32a in the last line to replace $\partial_t\rho$ with $-\partial_k(\rho v^k)$. Now we integrate Eq. 2.33 by parts and use the fact that astrophysical GW sources have finite sizes to discard the boundary terms. We find that

$$\begin{aligned}\frac{\mathrm{d}}{\mathrm{dt}}Q_{ij} &= \int \mathrm{d}^3x\rho v^k\partial_k\left[x_ix_j - \frac{1}{3}\delta^{ij}x_lx^l\right] \\ &= \int \mathrm{d}^3x\rho v^k\left[\partial_kx_ix_j - \frac{1}{3}\delta^{ij}\partial_k(x_lx^l)\right] \\ &= \int \mathrm{d}^3x\rho\left[x_iv_j + v_ix_j - \frac{2}{3}\delta^{ij}v_lx^l\right], \end{aligned} \tag{2.34}$$

where we integrated the first line by parts to get to the second line, and when going from the second to the third line we used the fact that $\partial_kx_i = \delta^{ki}$. We have now removed the first time derivative from Eq. 2.24, and we have replaced one power of x^i with v^i which reduces the weight given to slow moving regions. Next we take the time derivative of Eq. 2.34, which yields

$$\begin{aligned}\frac{\mathrm{d}^2}{\mathrm{dt}^2}Q_{ij} &= \frac{\mathrm{d}}{\mathrm{dt}}\int \mathrm{d}^3x\rho\left[x_iv_j + v_ix_j - \frac{2}{3}\delta^{ij}v_lx^l\right], \\ &= \int \mathrm{d}^3x\left[x_i(\partial_t\rho v_j) + (\partial_t\rho v_i)x_j - \frac{2}{3}\delta^{ij}\partial_t(\rho v_l)x^l\right]. \end{aligned} \tag{2.35}$$

Now we use Eq. 2.32b to remove $\partial_t\rho v_i$ and we get

$$\begin{aligned}\frac{\mathrm{d}^2}{\mathrm{dt}^2}Q_{ij} = \int \mathrm{d}^3x\Big[&x_i(-\partial_jp - \rho\partial_j\Phi - \partial_k(\rho v_jv_k)) \\ &+ x_j(-\partial_ip - \rho\partial_i\Phi - \partial_k(\rho v_iv_k)) \\ &- \frac{2}{3}\delta^{ij}x^l(-\partial_lp - \rho\partial_l\Phi - \partial_k(\rho v_lv_k))\Big]. \end{aligned} \tag{2.36}$$

After integrating by parts terms of the form ∂_ip and $\partial_k(\rho v_iv_k)$ we are left with

$$\begin{aligned}\frac{\mathrm{d}^2}{\mathrm{dt}^2}Q_{ij} = \int \mathrm{d}^3x\rho\Big[&2v_iv_j - x_i\partial_j\Phi - x_j\partial_i\Phi \\ &- \frac{2}{3}\delta^{ij}(\rho v_lv_l - \rho x_l\partial_l\Phi)\Big]. \end{aligned} \tag{2.37}$$

Note that the terms containing the pressure in Eq. 2.36 cancel. The last step is to write Eq. 2.37 in a slightly more compact form

$$\ddot{Q}_{ij} = \mathrm{STF}\left[2\int \mathrm{d}^3x\rho\Big(v_iv_j - x_i\partial_j\Phi\Big)\right]. \tag{2.38}$$

Here STF denotes the projection operator onto the symmetric trace-free part, $\mathrm{STF}[A_{ij}] = \frac{1}{2}A_{ij} + \frac{1}{2}A_{ji} - \frac{1}{3}\delta_{ij}A_{ll}$. We have also adopted the notation that $\dot{x}$ represents the first time derivative of x, $\ddot{x}$ the second time derivative, and so on. In the end, we are left with an expression for the second time derivative of the quadrupole moment that depends on first-order spatial derivatives of the gravitational potential and the Cartesian velocity components. These terms have larger numerical values in the regions of the simulation generating most of the GWs, which is an advantage when numerically calculating the integral in Eq. 2.38. We have also eliminated the troublesome second-order time derivatives and arrived at a formula that is much more suited for computing waveforms in numerical studies than our starting point.

Note that in axisymmetry the only independent component of $h^{TT}_{\mu\nu}$ is

$$\mathbf{h}^{TT}_{\theta\theta} = \frac{1}{8}\sqrt{\frac{15}{\pi}}\sin^2\theta\frac{A^{\mathrm{E2}}_{20}}{D}, \tag{2.39}$$

where D is the distance to the source, θ is the inclination angle of the observer with respect to the axis of symmetry, and A^{E2}_{20} represents the only non-zero quadrupole amplitude. In spherical coordinates A^{E2}_{20} can be expressed as follows

$$\begin{aligned} A^{\mathrm{E2}}_{20}(t) = \frac{G}{c^4}\frac{16\pi^{3/2}}{\sqrt{15}}\int_{-1}^{1}\int_{0}^{\infty}\rho\,\big[v_r^2(3z^2-1)+ \\ v_\theta^2(2-3z^2) - v_\phi^2 - 6v_rv_\theta z\sqrt{1-z^2} + \\ r\partial_r\Phi(3z^2-1) + 3\partial_\theta z\sqrt{1-z^2}\Phi\Big]\, r^2dr\,dz. \end{aligned} \tag{2.40}$$

Here, v_i and ∂_i $(i = r, \theta, \phi)$ represent the velocity components and derivatives, respectively, along the basis vectors of the spherical coordinate system, and $z \equiv \cos\theta$. For details we refer the reader to Müller & Janka (1997).

In the quadrupole framework the energy, E, radiated by GWs is given by

$$E = \frac{G}{5c^5}\int \mathrm{d}t\,\dddot{Q}_{ij}\dddot{Q}_{ij}, \tag{2.41}$$

and the spectral energy density of the GWs is given by

$$\begin{aligned} \frac{\mathrm{d}E}{\mathrm{d}f} &= \frac{2G}{5c^5}(2\pi f)^2\tilde{\ddot{Q}}_{ij}\tilde{\ddot{Q}}_{ij} \\ &= \frac{2c^3}{5G}(2\pi f)^2\Bigg[|\tilde{\ddot{Q}}_{xx}|^2 + |\tilde{\ddot{Q}}_{yy}|^2 + |\tilde{\ddot{Q}}_{zz}|^2 \\ &+ 2\big(|\tilde{\ddot{Q}}_{xy}|^2 + |\tilde{\ddot{Q}}_{xz}|^2 + |\tilde{\ddot{Q}}_{yz}|^2\big)\Bigg], \end{aligned} \tag{2.42}$$

where a tilde denotes a Fourier transform, and f is the frequency. We define the Fourier transform as follows:

$$\tilde{\ddot{Q}}_{ij}(f) = \int_{-\infty}^{\infty} \ddot{Q}_{ij}(t) e^{-2\pi i f t} \mathrm{d}t. \tag{2.43}$$

For a discrete time series the Fourier transform is replaced by the discrete Fourier transform (DFT). We define the DFT, $\widetilde{X}_k$, as follows:

$$\widetilde{X}_k(f_k) = \frac{1}{M} \sum_{m=1}^{M} x_m e^{-2\pi i k m/M}, \tag{2.44}$$

Here, x_m is the time series obtained by sampling the underlying continuous signal at M discrete times. $f_k = k/T$ is the frequency of bin k, where T is the duration of the signal.

We will repeat these definitions and discuss our Fourier analysis in detail in a later chapter.

3. Supernovae

The history of supernovae starts, as most astrophysical objects, with observations of strong electromagnetic events in the night sky. Supernovae are some of the most energetic events known to astronomers and throughout history, some have been clearly visible by naked eye and could be seen even during the day (see Hamacher (2014) and references therein). The Crab supernova was in 1054 described by Chinese astronomers (Ho, 1962, Shen, 1969).

> *... it was visible by day, like Venus; pointed rays shot out from it on all sides; the color was reddish-white. Altogether it was visible for 23 days.*

3.1. Classifying supernovae

In the modern era observations of supernovae continually improved. In 1941 German-American astronomer Rudolph Minkowski (Minkowski, 1941) found that not all supernovae show hydrogen lines in their spectra and he consequently divided supernovae into two types based on the presence of hydrogen (Type II) or lack of hydrogen lines (Type I). Later it was recognized that there were variations of spectra and, light curve of supernovae within these two classes and a set of subclasses was devised. Type I supernovae were divided into type Ia, Ib, and Ic, where the nebular spectrum of types Ib and Ic was found to be similar to those of type II supernovae. Two examples of the type II sub-classes are types II-L and II-P. After reaching the maximum luminosity, the light curves of type II-P supernovae settles onto a plateau and their luminosity reminds almost constant for several months. The luminosity of Type II-L, on the other hand, decline almost linearly. For a detailed review of the classification system see Cappellaro & Turatto (2001).

The similarities between the nebular spectra of type II and type Ib/c supernovae already hints at a similar explosion mechanism. From a theoretical standpoint, one might say that a classification based on physical processes powering the supernovae is more prudent. Already in 1960 Hoyle & Fowler (1960) suggested that type II supernovae result from the implosion of stellar cores and that type I is produced by igniting degenerate stellar material. Today it is understood that that type Ia supernovae result from the thermonuclear explosions of white dwarfs. In other words, the ignition of degenerate stellar material. Furthermore, we now know that type II and type Ib/c supernovae are the result of the gravitational collapse, the implosion, of stellar cores. The latter category are known as core-collapse supernovae. The subject of this thesis is the GWs generated during the collapse and subsequent explosion of a specific sub-type of core-collapse supernova, the "Iron-core supernova", and we, therefore, constrain our attention to this class of supernovae. The interested reader is referred to Janka (2012) for a comprehensive description of the possible explosion mechanisms.

3.2. Iron-core supernovae

3.2.1. Shell burning in massive stars

When a massive star nears the end of its life, and has depleted most of the hydrogen in the central core, hydrogen burning ceases and the gravitational pull is no longer balanced by thermal and radiation pressure resulting from nuclear fusion. The consequence is that the core starts to contract, the contraction is eventually halted when the pressure and temperature in the core become large enough for helium burning to set in. The layer right outside of the helium burning core is still rich in hydrogen and so hydrogen burning develops in a layer around the core. The burning of helium in the core stabilises the star, for a while. However, the helium fuel eventually runs out and the process repeats itself, only this time the contraction continues until carbon ignites in the inner core.

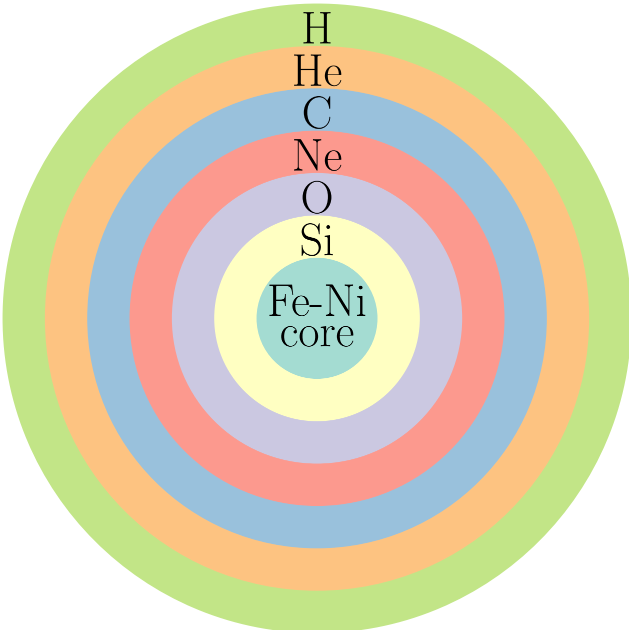

Figure 3.1.: Schematic representation of the shell structure of a massive star right before the onset of core-collapse. The stellar core consists of consecutive layers burning heavier and heavier elements and an inner iron-nickel core.

The process of burning heavier and heavier elements in the core continues up to silicon. The end products of silicon burning are iron-group elements and since nuclear fusion of iron-group elements does not release any energy the cycle stops at silicon. The end result of this process is an onion like shell structure consisting of consecutive layers burning heavier and heavier elements. In the centre of this onion is an ever growing core consisting of iron and nickel (henceforth referred to as the "iron-core"), it grows due to the accretion of the ashes produced by the continued burning of silicon in the layer above. A depiction of this shell structure can be seen in Fig. 3.1. The star remains in this state for a while, until the central iron-core has accumulated so much matter that its mass exceeds the Chandrasekhar mass and the inevitable gravitational collapse of the core begins.

3.2.2. Iron-core collapse

The collapse of the iron-core is triggered and accelerated by two processes. Firstly, rising temperatures increase the rate of photo-dissociation of iron-group nuclei. The nuclei are converted into free nucleons and alpha particles, which is a process that consumes thermal energy. Secondly, as the core density increases electron capture on heavy nuclei becomes more frequent. Free electrons are capture by protons in the nuclei and a neutrons and anti-electron neutrinos are produced:

$$p + e^- \to n + \bar{\nu}_e, \tag{3.1}$$

where p^+, e^-, n and $\bar{\nu}_e$ represents a proton, an electron, a neutron and an anti-electron neutrino, respectively. The neutrinos escape the core and in the process carry with them energy and lepton number. Before the onset of collapse it was pressure from degenerate electrons that was supporting the core. When he lepton number decreases the pressure also decreases, and this leads to an acceleration of the collapse. Effectively what is happening is that the Chandrasekhar mass of the core is reduced.

The rapid deleptonisation of the iron-core eventually slows down and virtually stops for the duration of the collapse. At densities around 10^{12} g/cm^3 the mean free path of the neutrinos become so short that the time they need to diffuse out of the core is larger than the time-scale of the collapse. The collapse continues until the central iron-core reaches nuclear densities, around 2.7×10^{14}g/cm^3, at this point the repulsive forces between nuclei leads to a sudden stiffening of the equation of state (EoS) and the collapse of the inner iron-core comes to an abrupt halt.

However, due to its high inertia the inner core contracts beyond the equilibrium point of the gravitational pull and the new source of pressure. This leads to a recoil and as the inner region of the iron-core expands outwards it crashes into the infalling material above it. This event is the so-called core bounce and it launches a sound wave into the outer iron-core, that steepens into a shock wave when it reaches the supersonically infalling layers of the outer core.

As the shock propagates outwards through the dense stellar material it loses about 10^{51} erg of energy per 0.1 $M_\odot$of iron-core material that falls through the shock front, due to the dissociation of heavy nuclei into free nucleons. Eventually, the density ahead of the shock drops below $\sim 10^{11}$ g/cm^3 and the neutrinos behind the shock can suddenly escape. This leads to a burst of neutrino emission and a significant loss of energy for the shock. After a few milliseconds (ms) the shock has lost so much energy that it stalls at a radius between 100 and 200 km and turns into an accretion shock.

3.2.3. Shock revival: the neutrino heating mechanism

It was initially thought that the shock would not stall, but rather propagate throughout the mantle of the star and disrupt it in the process. This mechanism is known as the bounce-shock or prompt-shock mechanism. As mentioned above, the shock only propagates outwards a for a few ms before losing most of its energy and stagnating. The failure of the bonce-shock mechanism can be viewed as a consequence of its failure to account for anything else than purely hydrodynamical effects. Most of the gravitational binding energy released during the collapse is stored in the form of trapped neutrinos and tapping into this energy reservoir might provide the energy needed to revive the stalled shock. Already in 1966 Colgate & White (1966) proposed that neutrinos cold be the principle actor in the drama unfolding deep within the star. Later this idea was revisited and expanded upon by Wilson (1985) who formulated the so-called "delayed neutrino-driven explosion mechanism".

At the same time as the shock is initially launched a hot proto-neutron star (PNS) forms in the center of the star. The gravitational binding energy released during the collapse is converted into thermal energy. The PNS mainly cools through emission of neutrinos, which first slowly diffuse through the optically thick inner-core before breaking out of the so-called neutrinosphere and streaming away from the core. The neutrinosphere is defined by the radius where the core becomes optically thin to neutrinos. A secondary source of neutrinos is the matter falling through the stalled shock and accreting onto the PNS, which releases neutrinos as the material settles onto the PNS. The capture of electrons and positrons on free nuclei is the main source of neutrinos in the hot accretion layer around the PNS. This means that electron and anti-electron neutrinos make up a large fraction of the neutrino emission generated by PNS accretion.

The material falling through the shock also exerts the ram pressure that must somehow be counteracted to relaunch the shock. As neutrinos stream away from the core a small fraction of their energy is deposited into the stellar material behind the shock, because this material is not perfectly optically thin to neutrinos. It is this energy deposition that is thought to balance and eventually overcome the ram pressure of the infalling of the material, leading to the successful revival of the stalled shock.

3.3. The post-bounce phase

The phase between core bounce and shock revival is a crucial time period for the delayed neutrino-driven explosion mechanism. The focus of this thesis is to study what we can learn about core collapse supernovae by observing the gravitational wave (GW) signal they produce. Specifically, this work focuses on fingerprints of hydrodynamical processes operating during the post-bounce phase. In this section, we discuss our current understanding of the properties of the region behind the stalled shock front, consisting of the PNS and the region between the PNS and the shock front (known as the post-shock volume/region/layer).

3.3.1. The gain layer, cooling layer, and the three layers of the Proto-neutron star

The fact that the mean free path of the neutrinos increases with radius means that neutrino diffusion more effectively carries away lepton number and entropy in the outer regions of the PNS core. This leads to the establishment of negative entropy and composition gradients, which in turn creates a convectively unstable region located between the surface and the inner PNS core (see Fig. 3.2).

The heating of the stellar material in the post-shock region is dominated by charged-current reactions

$$\begin{aligned} n + \nu_e &\to p + e^-, \\ p + \bar{\nu}_e &\to n + e^+, \end{aligned} \tag{3.2}$$

and cooling by the corresponding inverse interactions

$$\begin{aligned} p + e^- &\to n + \nu_e, \\ n + e^+ &\to p + \bar{\nu}_e. \end{aligned} \tag{3.3}$$

The neutrino-cooling rate, caused by the reactions described by Eq. 3.3, depends on the temperature to the sixth power, $\sim T^6$. Since the temperature of the convectively mixed post-shock layer drops roughly as $\sim 1/r$ (Janka, 2012) the cooling efficiency drops as $\sim r^{-6}$ The heating rate, on the other hand, drops off only as radius squared, $\sim r^{-2}$. As a result, there exists a radius where heating and cooling effects balance each other. This radius is called the "gain radius". Below the gain radius neutrino cooling dominates and above there is a net heating by neutrinos. The neutrino heating from below makes the gain layer unstable to large-scale convective activity. The high-entropy bubbles that are created by convection push the shock front outwards. This prolongs the time it takes for the stellar matter to be advected through the layer, which enhances the heating done by neutrinos. Convection also transports heated material away from the gain radius and prevents it from falling down into the cooling layer. The end result is that the matter falling through the shock spends considerably more time in the gain layer than it would without the development of convection. This favours the delayed neutrino-driven explosion mechanism and has been studied by several authors (see for example Herant et al. (1994), Burrows et al. (1995), Janka & Müller (1996), Foglizzo et al. (2006), Müller et al. (2012b)). In Fig. 3.2 we see a schematic depiction, not to scale, of the region behind the stalled shock. The PNS is indicated by the grey region, the cooling layer by the light blue and the light red region indicates the gain layer. The circles with arrows indicate convection. The dark red curve at the edge of the gain layer indicates the shock front, with its large-scale and small-scale deformations.

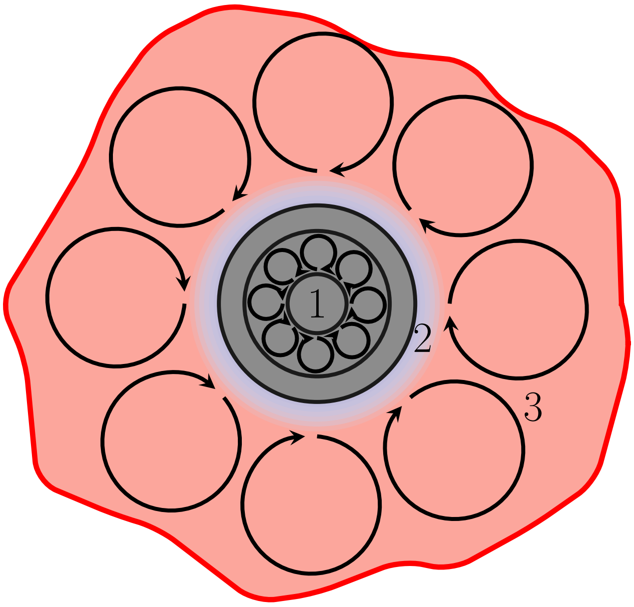

1: Proto-neutron star. 2: Cooling layer. 3: Gain layer.

Figure 3.2.: Schematic representation of the region behind the shock. The grey region indicates the PNS, the light blue region shows the cooling layer and the gain layer is indicated by the light red region. The dark red boundary shows the shock front with its large and small scale deformations. Circular arrows indicate the two regions that are convectively active.

3.3.2. The standing accretion shock instability

Another instability that can develop and be beneficial for the explosion mechanism is the so-called standing accretion shock instability (SASI), which manifests itself in large-scale sloshing and spiral motions of the shock (Blondin et al., 2003, Blondin & Mezzacappa, 2006, Foglizzo et al., 2007, Ohnishi et al., 2006; 2008, Scheck et al., 2008, Guilet & Foglizzo, 2012, Foglizzo et al., 2015). The SASI develops through an advective-acoustic cycle, entropy and vorticity perturbations from the shock are advected through the post-shock layer and when they are decelerated at the PNS surface they are converted into pressure waves that propagate out towards the shock front. Once these acoustic waves hit the stalled shock they perturb it, completing the feedback cycle. The large-scale deformation of the shock pushes the average radius outwards and therefore enhances neutrino heating.

3.4. Three-dimensional simulations

After promising results from two-dimensional (2D) simulations supernova modelers experienced initial setbacks in three-dimensional (3D) (Hanke et al., 2012; 2013). Now, however, we are starting to see the emergence of the first generation of successful 3D simulations of explosions with three-flavour multi-group neutrino transport, culminating in the recent models of the Garching and Oak Ridge groups (Melson et al., 2015a;b, Lentz et al., 2015) with their rigorous treatment of the transport and neutrino microphysics in addition to many more obtained with more approximate transport schemes, as for example the studies of Takiwaki et al. (2012; 2014), Müller (2015) and Roberts et al. (2016). Takiwaki et al. (2012; 2014) employ the isotropic diffusion source approximation (Liebendörfer et al., 2009) and use further approximations to treat heavy lepton neutrinos. Takiwaki et al. (2014) employ a leakage scheme to account for heavy lepton neutrinos and Takiwaki et al. (2012) neglect the effect of these neutrinos altogether. Müller (2015) utilises the stationary fast multi-group transport scheme of Müller & Janka (2015), which solves the Boltzmann equation at high optical depths in a two-stream approximation and matches the solution to an analytic variable Eddington factor closure at low optical depths. Roberts et al. (2016) employ a full 3D two-moment (M1) solver in general relativistic simulations, but ignore velocity-dependent terms. On the other hand, it has proven difficult to consistently relaunch the stalled supernova shock in full 3D simulations. Numerical modeling of core-supernovae is an active field of research and as of now there is no consensus of what exactly is the key to successful 3D explosions.

4. Numerical simulations of core-collapse supernovae

The GW signals presented in this thesis are based on supernova simulations that were performed with the code Prometheus-Vertex. The simulations were carried out by members of the Garching-group (Hanke (2014), Melson (2016), Summa (2017)). In this chapter, we describe the code that was used. We will describe the details of individual models in later chapters. Prometheus-Vertex solves the combined problems of hydrodynamics and neutrino radiation transport. The code has been specifically developed for the core-collapse problem, the first version was designed in 2002 by Rampp & Janka (2002)

4.1. Prometheus

The hydrodynamics of the stellar collapse is solved with a version of the well-established Prometheus code (Müller et al., 1991, Fryxell et al., 1991). It solves the non-relativistic equations of hydrodynamics for the flow of an inviscid self-gravitating ideal fluid in spherical coordinates (r, θ, ϕ).

4.1.1. Hydrodynamics

In spherical coordinates the Euler equations of hydrodynamics are

$$\partial_t \rho + \frac{1}{r^2}\partial_r(r^2 \rho v_r) + \frac{1}{r\sin\theta}\Big[\partial_\theta(\rho\sin\theta v_\theta) + \partial_\phi(\rho v_\phi)\Big] = 0, \tag{4.1}$$

$$\partial_t(\rho v_r) + \frac{1}{r\sin\theta}\Big[\partial_\theta(\rho\sin\theta v_\theta v_r) + \partial_\phi(\rho v_\phi v_r)\Big] +$$
$$\frac{1}{r^2}\partial_r(r^2\rho v_r^2) - \rho\frac{v_\theta^2 + v_\phi^2}{r} + \partial_r p = -\rho\partial_r\Phi + Q_{M_r}, \tag{4.2a}$$

$$\partial_t(\rho v_\theta) + \frac{1}{r^2}\partial_r(r^2\rho v_r v_\theta) + \frac{1}{r\sin\theta}\Big[\partial_\theta(\rho\sin\theta v_\theta^2) + \partial_\phi(\rho v_\phi v_\theta)\Big]$$
$$+ \rho\frac{v_\theta v_r - v_\phi^2/\tan\theta}{r} + \frac{1}{r}\partial_\theta p = -\frac{\rho}{r}\partial_\theta\Phi + Q_{M_\theta}, \tag{4.2b}$$

$$\partial_t(\rho v_\phi) + \frac{1}{r\sin\theta}\Big[\partial_\theta(\rho\sin\theta v_\theta v_\phi) + \partial_\phi(\rho v_\phi^2) + \partial_\phi p\Big]$$
$$+ \frac{1}{r^2}\partial_r(r^2\rho v_r v_\phi) + \rho\frac{v_\theta v_\phi/\tan\theta + v_\phi v_r}{r} = -\frac{1}{r\sin\theta}\partial_\phi\Phi + Q_{M_\phi}, \tag{4.2c}$$

$$\partial_t e + \frac{1}{r^2}\partial_r(r^2 v_r(e+p)) + \frac{1}{r\sin\theta}\Big[\partial_\theta(\sin\theta v_\theta(e+p)) + \partial_\phi(v_\phi(e+p))\Big]$$
$$= -\rho v_r\partial_r\Phi - \rho\frac{v_\theta}{r}\partial_\theta\Phi - \frac{v_\phi}{r\sin\theta}\partial_\phi\Phi + Q_E + v_r Q_{M_r} + v_\theta Q_{M_\theta} + v_\phi Q_{M_\phi}. \tag{4.4}$$

Here p is pressure, ρ is density, e is the specific total (internal plus kinetic) energy, Φ is the gravitational potential and v_r, v_θ, and v_ϕ are the velocity components in the spherical coordinate basis. The source terms Q_{M_r}, Q_{M_θ}, and Q_{M_ϕ} represent momentum transfer by neutrinos, in the radial, polar, and azimuthal direction, respectively. Energy transport by neutrinos is represented by the source term Q_{M_E}. These source terms are calculated by the neutrino-transport module VERTEX, which we will discuss later in this chapter. The above equations have to be closed by an EoS, which generally will depend on density, internal energy, and the chemical composition of the stellar matter. This means that one has to track two additional quantities, the mass fractions of various nuclear species, denoted by X_i, and the electron fraction Y_e. We, therefore, have to solve two additional conservation equations:

$$\partial_t(\rho X_i) + \frac{1}{r^2}\partial_r(r^2\rho v_r X_i) + \frac{1}{r\sin\theta}\Big[\partial_\theta(\rho\sin\theta v_\theta X_i) + \partial_\phi(\rho v_\phi X_i)\Big] = \varsigma_i, \tag{4.5}$$

$$\partial_t(\rho Y_e) + \frac{1}{r^2}\partial_r(r^2\rho v_r Y_e) + \frac{1}{r\sin\theta}\Big[\partial_\theta(\rho\sin\theta v_\theta Y_e) + \partial_\phi(\rho v_\phi Y_e)\Big] = Q_{Y_e}. \tag{4.6}$$

The two source terms ς_i and Q_{Y_e} represent the change of composition of species i due nuclear reactions and the change in electron fraction caused by emission and absorption of electron and anti-electron neutrinos, respectively. If the fluid reaches nuclear statistical equilibrium, the chemical composition is fully determined by the EoS, through the electron fraction, density, and temperature.

PROMETHEUS solves the system of equations by means of a dimensionally-split implementation of the piecewise parabolic method of Colella & Woodward (1984). The scheme is time-explicit and it is accurate to third-order in space (for equidistant grids) and second-order in time. The Riemann solver implemented in the code exactly solves one-dimensional (1D) Riemann problems in so-called sweeps that have been obtained from the full three-dimensional (3D) equations by Strang-splitting (Strang, 1968). When strong shocks are encountered the solver switches to the "HLLE" solver (Einfeldt, 1988), in order to avoid the so-called "even-odd decoupling", which occurs when shocks are aligned with coordinate lines (Quirk, 1994, Kifonidis et al., 2003), and creates artificial oscillations. PROMETHEUS employs the consistent multi-fluid advection method of Plewa & Müller (1999) to ensure that the advection all the nuclear species is calculated accurately.

4.1.2. Equation of state

The models that this work is based on uses two different prescriptions for the EoS. A "high-density" EoS is used for the inner hot region of the core, while a "low-density" EoS is used for the low-density regions of the simulation volume. The two are separated by a density threshold, after core bounce this threshold is set to $\rho_T = 10^{11}$ g/cm^3. In the high-density regime the tabular EoS of Lattimer & Swesty (1991) with a nuclear incompressibility of 220 MeV is used. Below the threshold, in the low-density regime, the EoS describes nuclei as classical Boltzmann gases and electrons and positrons as Fermi gases with arbitrary degeneracy levels. The EoS also includes the effect of photons, wich are treated as an ideal gas with an adiabatic index of 4/3 (Janka, 1999).

4.1.3. Self gravity - the effective potential

Self-gravity is treated using the monopole approximation and the effects of general relativity are accounted for in an approximate fashion by means of a pseudo-relativistic effective potential (case A of Marek et al. (2006)). The effective potential includes general relativistic effects and takes into account the contributions from the pressure and energy of the medium. In the case of a monopole potential, the terms involving non-radial derivatives of the potential in the Euler equations vanish.

4.2. Vertex

The VERTEX code calculates the source terms on the right-hand side of the Euler equations by treating the neutrinos as a radiation field. The problem we need to solve is to find the phase-space distribution function $f(\mathbf{r}, \mathbf{q}, t)$ of the neutrinos. Essentially we want to find the number of neutrinos with momentum $\mathbf{q}$ at position $\mathbf{r}$, in other words the number of particles in the phase-space volume $\mathrm{d}\mathbf{q}\mathrm{d}\mathbf{r}$.

It is common to work in terms of the specific intensity $\mathfrak{I}(\mathbf{r}, \hat{n}, \xi, t)$, which is defined such that the amount of energy $d\xi$ transported in the energy interval $(\xi, \xi + \mathrm{d}\xi)$, by neutrinos propagating into the solid angle $\mathrm{d}\Omega$ in the direction $\hat{n}$, through a surface of area $\mathrm{d}A$, with normal vector $\hat{A} = \mathbf{r}/|\mathbf{r}|$, during the time interval $\mathrm{d}t$ is

$$d\xi = \mathfrak{I}(\mathbf{r}, \hat{n}, \xi, t)\, \hat{n} \cdot \hat{A}\, \mathrm{d}\xi\, \mathrm{d}A\, \mathrm{d}\Omega\, \mathrm{d}t. \tag{4.7}$$

The neutrino distribution function and the specific neutrino intensity are related as follows

$$\mathfrak{I}(\mathbf{r}, \hat{n}, \xi, t) = \frac{\xi^3}{h^3 c^2} f(\mathbf{r}, \hat{n}, \xi, t). \tag{4.8}$$

The evolution of the specific neutrino intensity are calculated by solving the Boltzmann equation

$$\frac{1}{c}\partial_t \mathfrak{I} + \hat{n}_i \partial_i \mathfrak{I} = \mathfrak{C}[\mathfrak{I}]. \tag{4.9}$$

The right hand side of Eq. 4.9 is a source term that describes scattering, emission and absorption of neutrinos (the so-called collision integral). $\mathfrak{C}[\mathfrak{I}]$ will in general depend on integrals of the specific neutrino intensity, which makes the problem difficult to solve numerically. A common strategy is to expand the specific neutrino intensity into angular moments

$$\mathfrak{L}(\mathbf{r}, \xi, t) \equiv \frac{1}{4\pi}\int \mathfrak{I}\, \mathrm{d}\Omega \qquad (0^{\mathrm{th}} - order), \tag{4.10}$$

$$\mathfrak{H}_i(\mathbf{r}, \xi, t) \equiv \frac{1}{4\pi}\int \mathfrak{I}\, \hat{n}_i\, \mathrm{d}\Omega \qquad (1^{\mathrm{st}} - order), \tag{4.11}$$

$$\mathfrak{K}_{ij}(\mathbf{r}, \xi, t) \equiv \frac{1}{4\pi}\int \mathfrak{I}\, \hat{n}_i\, \hat{n}_j\, \mathrm{d}\Omega \qquad (2^{\mathrm{nd}} - \mathrm{order}), \tag{4.12}$$

$$\vdots$$

and then solve the equations that arises when inserting these moments into Eq. 4.9

$$\frac{1}{c}\partial_t \mathfrak{L} + \partial_i \mathfrak{H}_i = \frac{1}{4\pi}\int \mathfrak{C}[\mathfrak{I}]\mathrm{d}\Omega, \tag{4.13}$$

$$\frac{1}{c}\partial_t \mathfrak{H}_i + \partial_i \mathfrak{K}_{ij} = \frac{1}{4\pi}\int \mathfrak{C}[\mathfrak{I}]\hat{n}_i\mathrm{d}\Omega. \tag{4.14}$$

$$\vdots$$

We see from these equations that the evolution of the k^{th}-order moment depends on $(k+1)^{\text{th}}$-order moment.

The version of VERTEX that is implemented into PROMETHEUS-VERTEX uses the so-called"ray-by-ray-plus" approximation of Buras et al. (2006a) (see Hanke (2014) for details about the implementation). For each angular direction of the computational grid a spherical symmetric radiation problem is solved with the "ray-by-ray-plus" method, by assuming that the radiation field is symmetric around the propagation direction of the rays. In other words, the code traces one "ray" per angular bin, this is what is known as the "ray-by-ray" method. In this case the angular moments of the specific neutrino intensity can be fully represented by scalars. Furthermore, the expansion of the specific neutrino intensity is truncated at 1^{st}-order and closed with a variable Eddington factor method. The two Eddington factors that are needed to close the system are the ratio of the 0^{th}-order and the 3^{rd}-order scalar angular moments, and the ratio of the 0^{th}-order and the 4^{th}-order scalar angular moments. The two factors are calculated from a simplified version of the Boltzmann equation in an iterative process until convergence within an acceptable error is reached. Buras et al. (2006b) found that it is necessary to take non-radial advection of neutrinos, and non-radial neutrino pressure gradients into account to avoid unphysical convection in the PNS. The inclusion of these terms is what is meant by the "plus" in "ray-by-ray plus".

VERTEX solves the neutrino transport problem for three neutrino species, ν_e, $\bar{\nu}_e$, and a species ν_X representing all heavy flavor neutrinos. For the models that make the basis of this work, the neutrinos were binned into 12 logarithmically spaced energy bins ranging from 0 to 380 MeV. A more detailed description of the numerical implementation, neutrino physics, and VERTEX in general can be found in Rampp & Janka (2002), Hanke (2014), and Melson (2016).

4.3. Grid setup

Since stars are, at least to lowest order, spherically symmetric objects it is advantageous to use spherical coordinates when performing numerical simulations. PROMETHEUS-VERTEX can use two different spherical grids.

4.3.1. Spherical polar grid

The first grid available in PROMETHEUS-VERTEX is a standard spherical polar grid, with mesh points $r_n \in [0, R]$, $\theta_n \in [0, \pi]$, and $\phi_n \in [0, 2\pi]$. The grid is logarithmically spaced in radius, and the angular points are spaced equidistantly. The "standard" spherical polar grid has a few shortcomings that can be problematic when performing numerical simulations. The grid contains coordinate singularities at the poles ($\theta = 0$ and $\theta = \pi$), and the zones in the ϕ-direction become smaller and smaller as one approaches the poles. This causes strong constraints on the size of the time step, and can lead to numerical artifacts near the poles (Wongwathanarat et al., 2010a, Müller, 2015).

4.3.2. Yin-Yang grid

To avoid the problems encountered at the poles of a standard spherical grid, Kageyama & Sato (2004) proposed to construct a grid from two geometrically identical subgrids (called Yin and Yang). The two sub-grids are both spherical and have identical local coordinates, their mesh points are defined as follows

$$r_n^Y \in [0, R], \tag{4.15}$$
$$\theta_n^Y \in [pi/4, 3\pi/4], \tag{4.16}$$
$$\phi_n^Y \in [-3pi/4, 3\pi/4]. \tag{4.17}$$

Here the superscript Y referrers to either the *Yin* or *Yang*. While the two grids have identical local coordinates, they are rotated with respect to each other in such a way to cover the whole sphere. If the Cartesian coordinates of the *Yin* grid are $(x^{Yin}, y^{Yin}, z^{Yin})$ then the local Cartesian coordinates of the *Yang* grid are

$$(x^{Yang}, y^{Yang}, z^{Yang}) = (-x^{Yin}, z^{Yin}, y^{Yin}). \tag{4.18}$$

The *Yang* grid is rotated by 90 degrees around the x-axis, and by 180 degrees around the y-axis of the *Yin* grid. This corresponds to the rotation matrix

$$R = \begin{pmatrix} -1 & 0 & 0 \\ 0 & 0 & 1 \\ 0 & 1 & 0 \end{pmatrix}. \tag{4.19}$$

With this prescription we avoid the problems that arise near the poles of a standard spherical grid. For more details about the implementation of the *Yin-Yang* grid in PROMETHEUS-VERTEX see Melson (2016).

5. Signal analysis

5.1. Fourier analysis

In order to study the frequency structure of a time signal it is common to approximate the signal as a sum of trigonometric functions. Two examples of such analysis are Fourier series and Fourier transforms. In this chapter we will mainly focus on the latter and discuss the tools used for signal analysis in this thesis.

5.1.1. Continuous and discrete Fourier transforms

We define the continuous Fourier transform (FT) of a continuous time signal $x(t)$ as

$$\widetilde{x}(f) = \int_{-\infty}^{\infty} x(t)e^{-2\pi i f t}\mathrm{d}t. \tag{5.1}$$

The FT transforms the signal from the time domain into the frequency (f) domain. Simply put, the Fourier transformation tells us how much an oscillation of frequency f contributes to the total signal.

If the time signal is represented by a discrete time series, as is the case with data from simulations, the integral on the right-hand side of Eq. 5.1 can be estimated by numerical integration and we can derive an expression for the corresponding discrete Fourier transform (DFT). Consider the time series x_m of duration T which has been obtained by sampling the underlying continuous signal $x(t)$ at M discrete, evenly spaced, times

$$x_m = x(t_m) = x(m\,\Delta t) \qquad m = 0, 1, 2, 3, 4...M, \tag{5.2}$$

where $\Delta t(= T/M)$ is the sampling interval. The time series x_m is by construction a periodic function with period T, regardless of the true periodicity of the underlying function. This implies that $x_M = x_0$. Since our signal has period T it means that the frequency of the slowest varying oscillation we can represent is $1/T$. By the same logic the second slowest oscillation we can capture has a frequency of $1/(T - \Delta t)$ and so on. This means that the discrete signal is represented by a set of $M + 1$ frequencies

$$f_k = k/M\Delta t \qquad k = 0, 1, 2, 3, 4...M. \tag{5.3}$$

We now calculate the integral in Eq. 5.1 for a given frequency f_k using the trapezoidal rule and find

$$\begin{aligned}\int_{-\infty}^{\infty} x(t)e^{-2\pi i f_k t}\mathrm{d}t &\simeq \int_{0}^{T} x(t)e^{-2\pi i f_k t}\mathrm{d}t \\ &\approx \sum_{m=1}^{M} x_m e^{-2\pi i f_k t_m}\Delta t \\ &= \sum_{m=1}^{M} x_m e^{-2\pi i k m/M}\Delta t \equiv \widetilde{X}_k \Delta t M. \end{aligned} \tag{5.4}$$

In the last line we have defined the discrete Fourier transform (DFT) of a time series x_m

$$\widetilde{X}_k(f_k) = \frac{1}{M}\sum_{m=1}^{M} x_m e^{-2\pi i k m/M}. \tag{5.5}$$

5.2. The short-time Fourier transform

The disadvantage of the Fourier transform is that it only gives you information about the frequency spectrum of the full-time signal. If we are analysing a signal with a varying frequency structure it will be useful to extract time-frequency information about the signal. This is done by separating the signal into shorter segments and then calculating the Fourier transform of each segment. In this way, we obtain spectral information about the signal at different times.

There are several ways to segment the signal, the method used in this thesis is to slide a time-window of length τ over the time signal, $x(t)$, in an iterative process. In each iteration, the window is shifted forward in time by $\Delta\tau$. This defines a set of functions

$$S^i \equiv x(t)\big[H(t+i\Delta\tau) - H(t+\tau+i\Delta\tau)\big] \qquad i = 0,1,2,3...., \tag{5.6}$$

where $H(t)$ is the Heaviside step function. The short-time Fourier transform (STFT) of $x(t)$ is then

$$\mathrm{STFT}[x(t)] \equiv \int_{-\infty}^{\infty} S^i e^{-2\pi i f t}\mathrm{d}t = \widetilde{S^i}_k \qquad i = 0,1,2,3...., \tag{5.7}$$

5.3. The Nyquist frequency and aliasing

An important question arising when sampling a continuous time signal is how may samples are required to accurately represent the signal.

The Nyquist sampling theorem Let $x_b(t)$ be a band-limited signal, that is

$$\widetilde{x_b}(f) = 0 \quad \text{if} \quad f > f_N, \tag{5.8}$$

where f_N is the band-limit of x_b. If x_b is sampled with a sampling frequency

$$f_s \geq 2 f_N \tag{5.9}$$

then the signal is uniquely determined by its samples. The frequency f_N is referred to as the Nyquist frequency.

If a signal is sampled at a lower rate than half the Nyquist frequency, the signal will not be represented accurately, and aliasing occurs. Suppose that we sample a signal which a sampling rate f_s and the signal contains oscillations at frequencies larger than $f_s/2$. Then the DFT will not be able to distinguish between oscillations with frequencies $f_c > f_s/2$ and $f - 2f_s$. This means that oscillations at a frequency f_c will be aliased down into to the frequency

$$f_a = f_c - f_N. \tag{5.10}$$

In the case of hydrodynamic simulations, aliasing can appear when data is not saved to disk frequently enough. In large 3D simulations, it is often unfeasible to save all the hydro-data for each individual time-step. It is, therefore, common to save data to disk at a given time interval. The simulations which this work are based on saved data roughly two times per millisecond of simulated time, which results in a Nyquist frequency of 1000 Hz.

5.4. The spectral energy density of a discrete time signal

Eq. 2.42 gives the expression for the spectral energy density of a continuous time signal, it is obtained by directly applying Parseval's theorem to Eq. 2.41.

Parseval's theorem If $\widetilde{x}$ is the Fourier transform of $x(t)$ then

$$\int_{-\infty}^{\infty} |x(t)|^2 \, \mathrm{d}t = \int_{-\infty}^{\infty} |\widetilde{x}(f)|^2 \, \mathrm{d}f. \tag{5.11}$$

To derive the corresponding expression for a discrete time series, first consider the quantity

$$\Gamma = \int_{-\infty}^{\infty} |g(t)|^2 \, \mathrm{d}t = \int_{-\infty}^{\infty} |\widetilde{g}|^2 \, \mathrm{d}f. \tag{5.12}$$

Next we construct the time-series g_n by sampling $g(t)$ M times over a time period T. We then use the same procedure we used to derive Eq. 5.4, that is to approximate the integral using the trapezoidal rule. This procedure yields

$$\begin{aligned}\Gamma &= \int_{-\infty}^{\infty} |\widetilde{g}|^2 \, \mathrm{d}f \\ &\approx \sum_{k=1}^{M} \Big| \sum_{m=1}^{M} x_m e^{-2\pi i k m/M} \Delta t \Big|^2 \Delta f \\ &= \sum_{k=1}^{M} \left|\widetilde{g}_k\right|^2 T^2 \Delta f = \sum_{k=1}^{M} \left|\widetilde{g}_k\right|^2 T,\end{aligned} \tag{5.13}$$

where we have used that $\Delta f = 1/T$ and $\Delta t = T/M$ (the $1/M^2$ is absorbed into the DFT). This implies that

$$\begin{aligned}\frac{\mathrm{d}}{\mathrm{d}f}\Gamma &= \frac{\mathrm{d}}{\mathrm{d}f} \int_{-\infty}^{\infty} |\widetilde{g}|^2 \mathrm{d}f \\ &\approx \left|\widetilde{g}_k\right|^2 T^2.\end{aligned} \tag{5.14}$$

The last step is to replace the placeholder function g by $\dddot{Q}_{ij}$ and use the fact that

$$\widetilde{\dot{x}(t)} = 2\pi f \widetilde{x(t)}. \tag{5.15}$$

We then find that

$$\frac{\mathrm{d}}{\mathrm{d}f} E \approx \left[\frac{\Delta E}{\Delta f}\right]_k = \frac{2G}{5c^5} (2\pi f_k)^2 \left| \widetilde{\ddot{Q}^{ij}}_k \widetilde{\ddot{Q}^{ij}}_k \right| T^2. \tag{5.16}$$

Here we have changed the subscript ij of Q_{ij} into a superscript for better readability.

6. Gravitational waves from three-dimensional core-collapse simulations

The content of this chapter has been published in Andresen et al. (2016), with only minor modifications being made to the manuscript when adopting it for this thesis. The original manuscript text was written together with coauthors Bernhard Müller[1,2], Ewald Müller[3], and Hans-Thomas Janka[3].

[1]Astrophysics Research Centre, School of Mathematics and Physics, Queen's University Belfast, Belfast BT7 1NN, United Kingdom

[2]Monash Centre for Astrophysics, School of Physics and Astronomy, Building 79P, Monash University, Victoria 3800, Australia

[1]Max-Planck-Institut für Astrophysik, Karl-Schwarzschild-Str. 1, D-85748 Garching, Germany

6.1. Introduction

Over the last few years successful 3D simulations of core-collapse has given credence to the the delayed neutrino driven explosion mechanism. Explosions have been obtained in simulations with sophisticated transport and neutrino microphysics (Melson et al., 2015a;b, Lentz et al., 2015, Summa, 2017) and in models with more approximate prescriptions of the neutrino physics (Takiwaki et al., 2012; 2014, Müller, 2015, Roberts et al., 2016).

Hydrodynamical instabilities operating behind the stalled shock front have been found to be crucial for the success of this scenario as they help to push the shock further out by generating large Reynolds stresses (or "turbulent pressure", see Burrows et al., 1995, Murphy et al., 2013, Couch & Ott, 2015, Müller & Janka, 2015) and transporting neutrino-heated material out from the gain radius, which then allows the material to be exposed to neutrino heating over a longer "dwell time" (Buras et al., 2006b, Murphy & Burrows, 2008b). Moreover, if the instabilities lead to the formation of sufficiently large high-entropy bubbles, the buoyancy of these bubbles can become high enough to allow them to rise and expand continuously (Thompson, 2000, Dolence et al., 2013, Fernández, 2015).

Two such instabilities have been identified in simulations, namely the more familiar phenomenon of convection driven by the unstable entropy gradient arising due to neutrino heating (Bethe, 1990, Herant et al., 1994, Burrows et al., 1995, Janka & Müller, 1996, Müller & Janka, 1997), and the so-called standing accretion shock instability, which manifests itself in large-scale sloshing and spiral motions of the shock (Blondin et al., 2003, Blondin & Mezzacappa, 2006, Foglizzo et al., 2007, Ohnishi et al., 2006; 2008, Scheck et al., 2008, Guilet & Foglizzo, 2012, Foglizzo et al., 2015).

Our means to validate these numerical models by observations are limited. Classical photon-based observations of supernovae and their remnants (e.g. mixing in the envelope, see Wongwathanarat et al., 2015 and references therein; pulsar kicks, Scheck et al., 2006, Wongwathanarat et al., 2010b; 2013, Nordhaus et al., 2012) provide only relatively indirect constraints on the workings of these hydrodynamic instabilities in the inner engine of a supernova during the first second after the collapse. For a nearby, galactic supernova event, messengers from the core in the form of neutrinos and GWs could furnish us with a direct glimpse at the engine. Neutrinos, for example, could provide a smoking gun for SASI activity through fast temporal variations (Marek et al., 2009, Lund et al., 2010, Brandt et al., 2011, Tamborra et al., 2013; 2014a, Müller & Janka, 2014) and could even allow a time-dependent reconstruction of the shock trajectory (Müller & Janka, 2014).

Likewise, a detection of GWs could potentially help to unveil the multi-dimensional effects operating in the core of a supernova. The signal from the collapse and bounce of rapidly rotating iron cores and triaxial instabilities in the early post-bounce phase has long been studied in 2D (i.e. under the assumption of axisymmetry) and 3D (e.g. Ott et al., 2007, Dimmelmeier et al., 2007a; 2008, Scheidegger et al., 2008, Abdikamalov et al., 2010). Understanding the GW signal generated by convection and the SASI in the more generic case of slow or negligible rotation has proved more difficult due to a more stochastic nature of the signal. During the recent years, however, a coherent picture of GW emission has emerged from parameterised models (Murphy et al., 2009) and first-principle simulations of supernova explosions in 2D (Marek et al., 2009, Müller et al., 2013): The models typically show an early, low-frequency signal with typical frequencies of $\sim$100 Hz arising from shock oscillations that are seeded by prompt convection (Marek et al., 2009, Murphy et al., 2009, Yakunin et al., 2010, Müller et al., 2013, Yakunin et al., 2015). This signal component is followed by a high-frequency signal with stochastic amplitude modulations that is generated by forced oscillatory motions in the convectively stable neutron star surface layer (Marek et al., 2009, Murphy et al., 2009, Müller et al., 2013) with typical frequencies of 300 . . . 1000 Hz that closely trace the Brunt-Väisäla frequency in this region (Müller et al., 2013). Prior to the explosion, these oscillations, tentatively identified as $l = 2$ surface g-modes by Müller et al. (2013), are primarily driven by the downflows impinging onto the neutron star, whereas PNS convection takes over as the forcing agent a few hundred milliseconds after shock revival as accretion dies down. This high-frequency contribution dominates the energy spectrum and the total energy emitted in GWs can reach $\sim 10^{46}$ erg (Müller et al., 2013, Yakunin et al., 2015).

Since 3D supernova models have proved fundamentally different to 2D models in many respects, it stands to reason that much of what we have learned about GW emission from first-principle 2D models will need to be revised. In 2D, the inverse turbulent cascade (Kraichnan, 1967) facilitates the emergence of large-scale flow structures also in convectively-dominated models and helps to increase the kinetic energy in turbulent fluid motions in the post-shock region (Hanke et al., 2012). Furthermore, accretion downflows impact the PNS with much higher velocities in 2D than in 3D (Melson et al., 2015a) due to the inverse turbulent cascade and the stronger inhibition of Kelvin-Helmholtz instabilities at the interface of supersonic accretion downflows (Müller, 2015). In the SASI-dominated regime, on the other hand, the additional dimension allows the development of the spiral mode (Blondin & Mezzacappa, 2007, Blondin & Shaw, 2007, Fernández, 2010) in 3D, which can store more non-radial kinetic energy than pure sloshing motions in 2D (Hanke et al., 2013, Fernández, 2015), contrary to earlier findings of Iwakami et al. (2008). Such far-reaching differences between 2D and 3D cannot fail to have a significant impact on the GW signal.

While the impact of 3D effects on the GW signals from the post-bounce phase has been investigated before, all available studies have relied on a rather approximate treatment of neutrino heating and cooling such as simple light-bulb models (Müller & Janka, 1997, Kotake et al., 2009; 2011), grey neutrino transport (Fryer et al., 2004, Müller et al., 2012a), or a partial implementation of the isotropic diffusion source approximation of Liebendörfer et al. (2009) in the works of Scheidegger et al. (2008; 2010), which were also limited to the early post-bounce phase. Arguably, none of these previous studies have as yet probed precisely the regimes encountered by the best current 3D simulations (e.g. the emergence of a strong SASI spiral mode) and therefore cannot be relied upon for quantitative predictions of GW amplitudes and spectra, which are extremely sensitive to the nature of hydrodynamic instabilities, the neutrino heating, and the contraction of the PNS.

In this chapter, we present GW waveforms of the first few hundred milliseconds of the post-bounce phase computed from 3D models with multi-group neutrino transport. Waveforms have been analysed for four supernova models of progenitors with zero-age main sequence (ZAMS) masses of $11.2M_\odot$, $20M_\odot$ (for which we study an exploding and a non-exploding simulation), and $27M_\odot$. With four simulations based on these three different progenitors, we cover both the convective regime ($11.2M_\odot$) and the SASI-dominated regime ($20M_\odot$, $27M_\odot$). Our aim in studying waveforms from these progenitors is twofold: On the one hand, we shall attempt to unearth the underlying hydrodynamical phenomena responsible for the GW emission in different regions of the frequency spectrum during different phases of the evolution. We shall also compare the GW emission in 3D and 2D models, which will further illuminate dynamical differences between 2D and 3D. Furthermore, with 3D models now at hand, we are in a position to better assess the detectability of GWs from the post-bounce phase in present and future instruments than with 2D models affected by the artificial constraint of axisymmetry.

One of our key findings is that the GW signal from SASI-dominated models is clearly differentiated from convection-dominated model by strong emission in a low-frequency band around $100\ldots200\,\mathrm{Hz}$. Very recently, Kuroda et al. (2016) also studied the GW signal features (in models using grey neutrino transport) during phases of SASI activity for a $15M_\odot$ star, comparing results for three different nuclear equations of stats. Going beyond Kuroda et al. (2016), we clarify why this signature has not been seen in 2D models and point out that the hydrodynamic processes underlying this low-frequency signal are quite complex and seem to require a coupling of SASI motions to deeper layers inside the PNS. Moreover, we show that broadband low-frequency GW emission can also occur after the onset of the explosion and is therefore not an unambiguous signature of the SASI. We also provide a more critical assessment of the detectability of this new signal component, suggesting that it may only be detectable with second-generation instruments like Advanced LIGO for a very nearby event at a distance of 2 kpc or less.

Our chapter is structured as follows: We first give a brief description of the numerical setup and the extraction of GWs in Section 6.2. In Section 6.3, we present a short overview of the GW waveforms and then analyse the hydrodynamical processes contributing to different parts of the spectrum in detail. We also compare our results to recent studies based on 2D first-principle models. In Section 6.4, we discuss the detectability of the predicted GW signal from our three progenitors by Advanced LIGO (The LIGO Scientific Collaboration et al., 2015), and by the Einstein Telescope (Sathyaprakash et al., 2012) as next-generation instrument. We also comment on possible inferences from a prospective GW detection. Our conclusions and a summary of open questions for future research are presented in Section 6.5.

6.2. Supernova Models

6.2.1. Three-dimensional models

We study four 3D models based on three solar-metallicity progenitor stars with ZAMS masses of $11.2M_\odot$ (Woosley et al., 2002),$20M_\odot$ (Woosley & Heger, 2007) and $27M_\odot$ (Woosley et al., 2002). An initial grid resolution of $400 \times 88 \times 176$ zones in r, θ, and φ was used for the 3D models, and more radial grid zones were added during the simulations to maintain sufficient resolution around the PNS surface. The innermost 10 km were simulated in spherical symmetry to avoid excessive limitations on the time step when applying a spherical polar grid.

- **s11.2:** Model s11.2 (Tamborra et al., 2014b) is based on the solar-metallicity $11.2M_\odot$ progenitor of Woosley et al. (2002). This model exhibits transient shock expansion after the infall of the Si/O shell interface, but falls slightly short of an explosive runaway. After the average shock radius reaches a maximum of ≈250 km at a time of ≈200 ms after bounce, the shock recedes and shock revival is not achieved by the end of the simulation 352 ms after core bounce. The post-shock region is dominated by buoyancy-driven convection; because of the large shock radius no growth of the SASI is observed. The convective bubbles remain of moderate scale: Even during

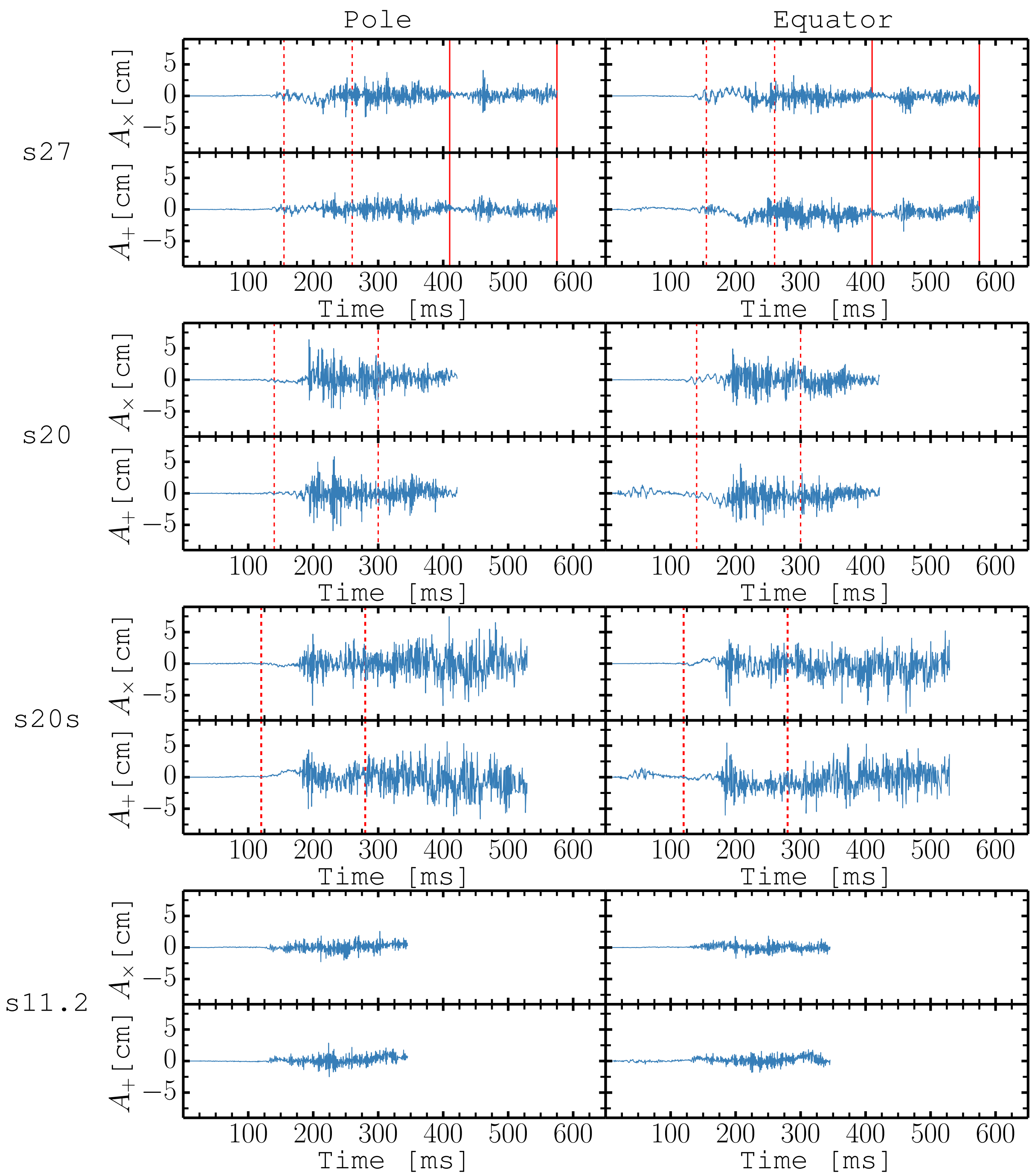

Figure 6.1.: GW amplitudes A_+ and $A_\times$ as functions of time after core bounce. From the top: s27, s20, s20s, and s11, respectively. The two columns show the amplitudes for two different viewing angles: an observer situated along the z-axis (pole; left) and an other observer along the x-axis (equator; right) of the computational grid, respectively. Episodes of strong SASI activity occur between the vertical red lines; dashed and solid lines are used for model s27 to distinguish between two different SASI episodes.

the phase of strongest shock expansion around ∼200 ms after bounce when the shock deformation is most pronounced and the kinetic energy in convection motions reaches its peak value, the bubbles subtend angles of no more than $\lesssim 60°$.

- **s20:** Model s20 is based on the $20M_\odot$ solar-metallicity progenitor of Woosley & Heger (2007) and has been discussed in greater detail in Tamborra et al. (2013; 2014a), where quasi-periodic modulations of the neutrino emission were analysed and traced back to SASI-induced variations of the mass-accretion flow to the PNS. No explosion is observed by the end of the simulation 421 ms post bounce. There is an extended phase of strong SASI activity (dominated by the spiral mode) between 120 and 280 ms after core bounce. After a period of transient shock expansion following the infall of the Si/O shell interface, SASI activity continues, but the kinetic energy in the SASI remains considerably smaller than during its peak between 200 and 250 ms.

- **s20s:** This model is based on the same $20M_\odot$ progenitor as s20, but a non-zero contribution from strange quarks to the axial-vector coupling constant, $g_\mathrm{a}^\mathrm{s} = -0.2$, from neutral-current neutrino-nucleon scattering was assumed (Melson et al., 2015b). This modification of the neutrino interaction rates results in a successful explosion (Melson et al., 2015b). Shock revival sets in around 300 ms after bounce. Prior to shock revival, the post-shock flow is dominated by large-scale SASI sloshing motions between 120 and 280 ms post-bounce. By the end of the simulation 528 ms post-bounce, the average shock radius is ≈1000 km, and a strong global asymmetry stemming from earlier SASI activity remains imprinted onto the post-shock flow. Asymmetric accretion onto the PNS still continues, but the accretion rate is reduced by a factor of ∼2 compared to model s20.

- **s27:** Our most massive model is based on the $27M_\odot$ solar-metallicity progenitor of Woosley et al. (2002) and has been discussed in greater detail in Hanke et al. (2013) and, for SASI-induced neutrino emission variations, by Tamborra et al. (2013; 2014a). Shock revival did not occur by the end of the simulation 575 ms after bounce. There are two episodes of pronounced SASI activity that are interrupted by a phase of transient shock expansion following the infall of the Si/O interface. The first SASI phase takes place between 120 and 260 ms post-bounce and the second period sets in around 410 ms post-bounce and lasts until the end of the simulation.

6.2.2. Two-dimensional models

In addition to the 3D models, we also analyse two 2D models based on the same progenitor as s27.

- **s27-2D:** Model s27-2D was simulated with the same numerical setup as s27 (see Hanke et al., 2013), with an initial grid resolution of 400×88 zones in r and θ and the innermost 10 km being simulated in spherical symmetry to allow for optimal comparison with the 3D model. SASI activity sets in about 150 ms after core bounce. Between 220 ms and 240 ms after bounce the accretion rate drops significantly after the Si/O shell interface has crossed the shock. The decreasing accretion rate leads to shock expansion, and shock revival occurs around 300 ms post bounce.

- **G27-2D:** In order to compare our results to those of a relativistic 2D simulation of the SASI-dominated s27 model, we also reanalyse the 2D model G27-2D presented by Müller et al. (2013), which was simulated with CoCoNuT-Vertex (Müller et al., 2010). CoCoNuT (Dimmelmeier et al., 2002a; 2005) uses a directionally-unsplit implementation of the piecewise parabolic method (with an approximate Riemann solver) for general relativistic hydrodynamics in spherical polar coordinates. The metric equations are solved in the extended conformal flatness approximation (Cordero-Carrión et al., 2009). The model was simulated with an initial grid resolution of 400×128 zones in r and θ, with the innermost 1.6 km being simulated in spherical symmetry to reduce time step limitations. For consistency, we recompute the GW amplitudes for this model based on the relativistic stress formula (Appendix A of Müller et al., 2013) instead of the time-integrated quadrupole formula with centred differences as originally used by Müller et al. (2013). The stress formula leads to somewhat larger amplitudes particularly at late times when central differencing is no longer fully adequate due to the increasing signal frequency.

  The model is characterised by strong post-shock convection for the first 50 ms after core bounce, which is followed by a phase of strong SASI activity. Around 120 ms after core bounce the average shock radius starts to increase steadily. The criterion for runaway shock expansion is met approximately 180 ms after bounce and the shock is successfully revived at $\sim$ 210 ms post bounce.

  The evolution of models G27-2D and s27-2D differs significantly during the pre-explosion phase: In G27-2D large-scale deformation of the shock already occurs $\sim$50 ms after bounce, without a preceding phase of hot-bubble convection (Müller et al., 2013). s27-2D develops SASI activity later: Since the average shock radius is $\sim$20-30 km larger in model s27-2D than in model G27-2D, conditions favour the development of neutrino-driven convection. Consequently, s27-2D shows an initial phase of convection before SASI activity sets in when the shock starts to retract $\sim$100-150 ms after bounce. Due to the early development of SASI activity in model G27-2D at a time when the accretion rate is high, particularly strong supersonic downflows onto the PNS develop.

  A possible reason for stronger and earlier SASI activity in model G27-2D is that, in contrast to model s27-2D, model G27-2D exhibits a phase of strong *prompt* post-shock convection (between a few ms after bounce and about 50 ms after bounce), which leaves the shock appreciably deformed with $|a_1|/a_0 \sim 0.01 - 0.02$ as shown in Fig. 7 of Müller et al. (2012c). Therefore the SASI amplitude only needs to grow by a factor of $\sim$30 to reach the non-linear regime. In Hanke et al. (2013,Fig. 2) the

$l = 1$ amplitude is much smaller at early times. Such differences in the post-bounce evolution can have a variety of reasons. Besides the pure stochasticity of simulations, the initial perturbations may also play a role: Model G27-2D was simulated in 2D from the onset of core collapse, while model s27-2D was started from a spherical model with seed perturbations imposed 15 ms after core bounce. The presence or absence of strong prompt post-shock convection also depends on the details of the entropy and electron fraction profiles, which are determined by the exact shock dynamics during the first milliseconds after core bounce. Without a very careful analysis of all the differences between the two simulations, we are not able to localise the origin of the differences between model G27-2D and model s27-2D in the different gravity treatment or any of the other aforementioned aspects.

Despite (or because of) the differences in the dynamics of the post-shock flow to s27-2D, model G27-2D is useful for illustrating the differences of the 3D model to the extreme end of the spectrum of recent 2D models in terms of peak GW amplitude and illustrates the mechanism of GW emission by stochastic surface g-mode excitation due to overshooting plumes from the gain region (Marek et al., 2009, Murphy et al., 2009, Müller et al., 2013) in the clearest form.

6.3. Structure and origin of the gravitational wave signal

The different 3D models used in our analysis probe distinctly different regimes that can be encountered in supernova cores. In this section, we will investigate how these dynamical differences are reflected in the GW signals. We also compare our 3D models to the two 2D models and investigate how and why the GW signal changes when going from 2D to 3D.

6.3.1. Gravitational wave extraction

In order to extract the GW signal from the hydrodynamical simulations, we post-process our simulations using the quadrupole stress formula (Finn, 1989, Nakamura & Oohara, 1989, Blanchet et al., 1990), see chapter 2. We disregard the contribution of anisotropic neutrino emission (Epstein, 1978) to the GW signal. Due to its low-frequency nature, it is of minor relevance for the detectability and does not affect the waveforms appreciably in the frequency range $\gtrsim 50\,\mathrm{Hz}$ that is of primary interest to us.

6.3.2. Overview of waveforms

Waveforms

Amplitudes for GWs generated by asymmetric mass motions are shown in Fig. 6.1. For each progenitor, we show two panels representing the cross and plus polarisation for two different observer positions. The two columns show the amplitudes for two different viewing angles, the right and left column representing observers situated along the z-axis (pole) and x-axis (equator) of the computational grid, respectively. * Since our (nonrotating) models do not exhibit a signal from a rotational bounce, and since (EoS-dependent) prompt post-shock convection is weak, the waveforms exhibit an initial quiescent phase. This is followed by a rather stochastic phase with amplitudes of several centimetres once convection or the SASI have fully developed. The correlation of stronger GW emission with the onset of strong, non-linear SASI activity in model s20, s20s, and s27 is illustrated by dashed and solid lines bracketing phases of particularly violent SASI oscillations.

The signal from early SASI activity triggered by prompt convection a few tens of milliseconds after bounce, which is typically rather prominent in 2D (Marek et al., 2009, Murphy & Burrows, 2008a, Yakunin et al., 2010, Müller et al., 2013, Yakunin et al., 2015), is thus strongly reduced in 3D. It is only clearly visible in the waveforms of s20 and s20s, while s11.2 and s27 only show traces of this component in some directions. The stochastic modulation of the later signal is reminiscent of 2D models, but the amplitudes are significantly lower ($\lesssim$4 cm) compared to several tens of cm in first-principle 2D models (Marek et al., 2009, Yakunin et al., 2010, Müller et al., 2013, Yakunin et al., 2015). The reduction in 3D is far stronger than could be expected from a mere projection effect (in agreement with parameterised models of Müller et al. 2012a).

Prior to a post-bounce time of ~200 ms, the waveforms for the three SASI-dominated models are clearly dominated by a low-frequency signal (in very much the same fashion as for early SASI activity a few tens of milliseconds after bounce in 2D). This already indicates that the relative importance of the low- and high-frequency components of the signal during the accretion phase is different in 3D compared to 2D, where low-frequency emission (triggered by prompt convection) only dominates for the first tens of milliseconds.

In the exploding model s20s with $g_a^s = -0.2$, we observe a tendency towards somewhat higher peak amplitudes than during the accretion phase well after the onset of the explosion (~300 ms). This tendency is, however, much less pronounced than in 2D models. The monotonous "tail" in the matter signal from anisotropic shock expansion (Murphy et al.,

*In our post-processing we chose to sample the GW signal at observer directions corresponding to cell centres of the simulation grid and as a consequence the two directions do not exactly correspond to the north pole ($\theta = 0, \phi = 0$) and the equator ($\theta = \pi, \phi = 0$), but are offset by half of the angular resolution. Hench, the coordinates of the polar and equatorial observer become $(\pi/176, \pi/176)$ and $(\pi - \pi/176, \pi/176)$, respectively.

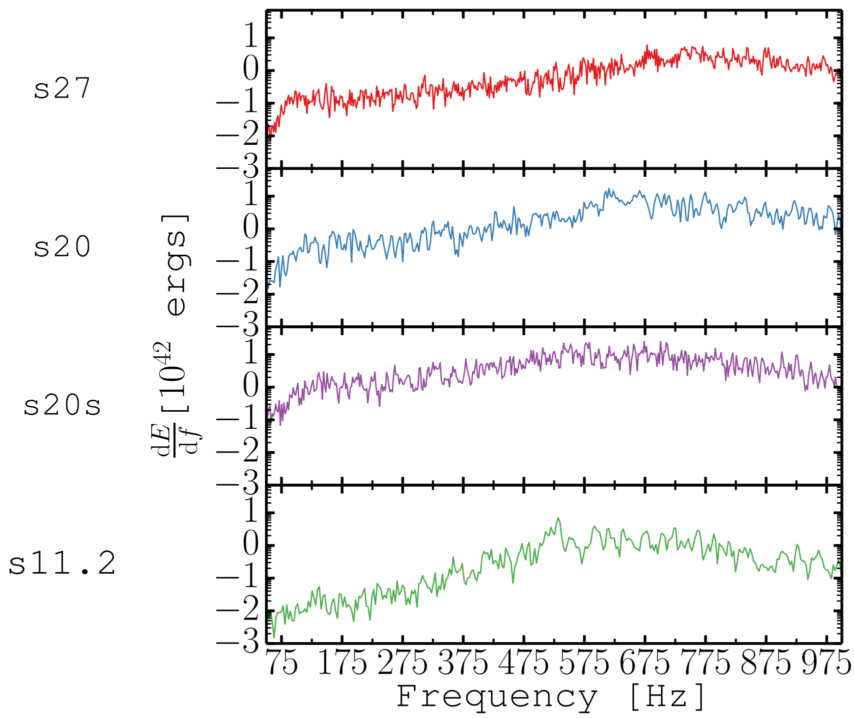

Figure 6.2.: Time-integrated GW energy spectra dE/df for models s27, s20, s11.2, and s20s (top to bottom). The spectra are computed from the Fourier transform of the entire waveform without applying a window function. The y-axis is given in a logarithmic scale.

2009, Yakunin et al., 2010) is noticeably absent, although no undue importance should be attached to this because it may take several hundreds of milliseconds for the tail to develop (Müller et al., 2013).

Energy spectra

Time-integrated energy spectra for each of the models are shown in Fig. 6.2. These are computed according to Eq. 2.42. The energy spectra of the three SASI-dominated models are relatively flat. This is significantly different from 2D models, where the energy spectra are dominated by a peak at several hundreds of Hz (Marek et al., 2009, Müller et al., 2013, Yakunin et al., 2015). Model s11.2, on the other hand, more closely resembles the 2D energy spectra, although the total energy emitted in GWs is considerably lower than in typical 2D models. In addition the peak values of dE/df are considerably higher in the SASI models than for s11.2.

The signal in the time-frequency domain

In order to dissect the signal further, we apply a short-time Fourier transform (STFT) to our waveforms. For a discrete time series the STFT is obtained by applying the discrete Fourier transform (DFT) to the signal with a sliding window (see chapter 5).

The resulting amplitude spectrograms for a sliding window of 50 ms are shown in Fig. 6.3. The spectrograms show the sum of the squared Fourier components of the cross and plus polarisation modes, $|\widetilde{A_+}|^2 + |\widetilde{A_\times}|^2$. Before applying the DFT we convolve the signal with a Kaiser window with shape parameter $\beta = 2.5$. Frequencies below 50 Hz and above 1100 Hz are filtered out of the resulting DFT. The amplitude spectrograms are computed for the same two observer directions as before.

All of the models exhibit the distinct high-frequency (here defined to be emission at frequencies greater than 250 Hz) component familiar from 2D models with a slow, secular increase in the peak frequency.

The SASI-dominated models stand apart from model s11.2 in that they show an additional low-frequency component (below 250 Hz) at late times (i.e. *not* associated with prompt convection). No such distinct low-frequency emission has been observed in spectrograms from 2D models (Murphy et al., 2009, Müller et al., 2013). The low-frequency component is clearly separated from the high-frequency emission by a "quiet zone" in the spectrograms. The frequency structure of the low-frequency component is rather complicated, and especially for models s20 and s20s it is rather broad-banded. There is also a directional dependence as can be seen, for example, from the later onset of low-frequency emission in the polar direction compared to the equatorial direction, in model s20 (second row in Fig. 6.3).

During the explosion phase, we find increased power in the high-frequency band corresponding to the increased peak amplitudes discussed in Section 6.3.2. However, the most conspicuous change after the onset of the explosion consists in a considerable increase of broadband power at low frequencies. Close inspection of Fig. 6.1 shows that the enhanced low-frequency emission can also be seen directly in the amplitudes: The amplitude "band" defined by stochastic high-frequency oscillations is clearly not centred at zero amplitude, but exhibits a significant low-frequency modulation.

Typical frequencies of the order of 100 Hz as well as a vague temporal correlation of the low-frequency emission with periods of strong sloshing/spiral motions suggest a connection with SASI activity. However, model s27 (top row in Fig. 6.3) also shows low-frequency emission during the phase between 280 ms and 350 ms after bounce when the SASI is relatively quiet. If the signal were directly due to the SASI, one would expect the phases of strong SASI and strong low-frequency emission to coincide. There may also be correlations between the low- and high-frequency emission as suggested by the fact that model s20 with the strongest low-frequency emission also exhibits the strongest high-frequency signal. Moreover, the source of enhanced low-frequency emission after shock revival is not immediately intuitive since the SASI no longer operates during this phase. This calls for a closer investigation of the hydrodynamic processes responsible for the emission of the two signal components.

6.3.3. Spatial location of underlying hydrodynamical instabilities

Which regions of the simulation volume contribute to the different GW components? The emission of GWs cannot be strictly localised, but one can nonetheless still partition the computational volume in the quadrupole formula (2.38) into different regions, and consider the formal contributions of each of these to the total signal. While this may not amount to a strict localisation of GW emission as coming from a specific region, such a partitioning nevertheless helps to detect fluid motions with the required temporal and frequency structure to account for different components of the signal in conjunction with the temporal evolution of the amplitudes and the spectral power. This procedure cannot replace a more rigorous identification of GW-emitting modes, which must, however, be left to the future.

In this work, we divide the integration volume into three layers A, B, and C (see Fig. 6.4). The PNS is split into two layers, the "convective layer" (layer A) and the convectively stable "surface layer"(layer B). The convectively stable inner core ($r < 10\,\mathrm{km}$) is not considered in our analysis because it is simulated in spherical symmetry and consequently does not contribute to the GW emission. A third layer (layer C) comprises the region between the outer boundary of the PNS (defined by a density of $10^{10}\,\mathrm{g\,cm^{-3}}$) and the outer boundary of the grid. We refer to this region as "post-shock" region because only motions in the post-shock region and the deceleration of matter at the shock effectively contribute to the signal from this layer.

The boundary between layer A and layer B is defined based on a horizontal averaging scheme from the stellar convection literature, see, e.g., Nordlund et al. (2009) and Viallet et al. (2013). We define volume-weighted horizontal averages (denoted by angled brackets) of any quantity X such as velocity, density, or pressure as follows,

$$\langle X \rangle = \frac{\int X \,\mathrm{d}\Omega}{\int \mathrm{d}\Omega}. \tag{6.1}$$

The quantity X is then decomposed into a mean and a fluctuating component,

$$X = \langle X \rangle + X'. \tag{6.2}$$

For defining the boundary between the convective region and the stable surface region, we consider the turbulent mass flux f_m,

$$f_m = \langle \rho' v_r' \rangle. \tag{6.3}$$

Inside the convective region, heavier fluid is advected downwards while fluid that is lighter than average rises upwards. The turbulent mass flux will, therefore, always be negative

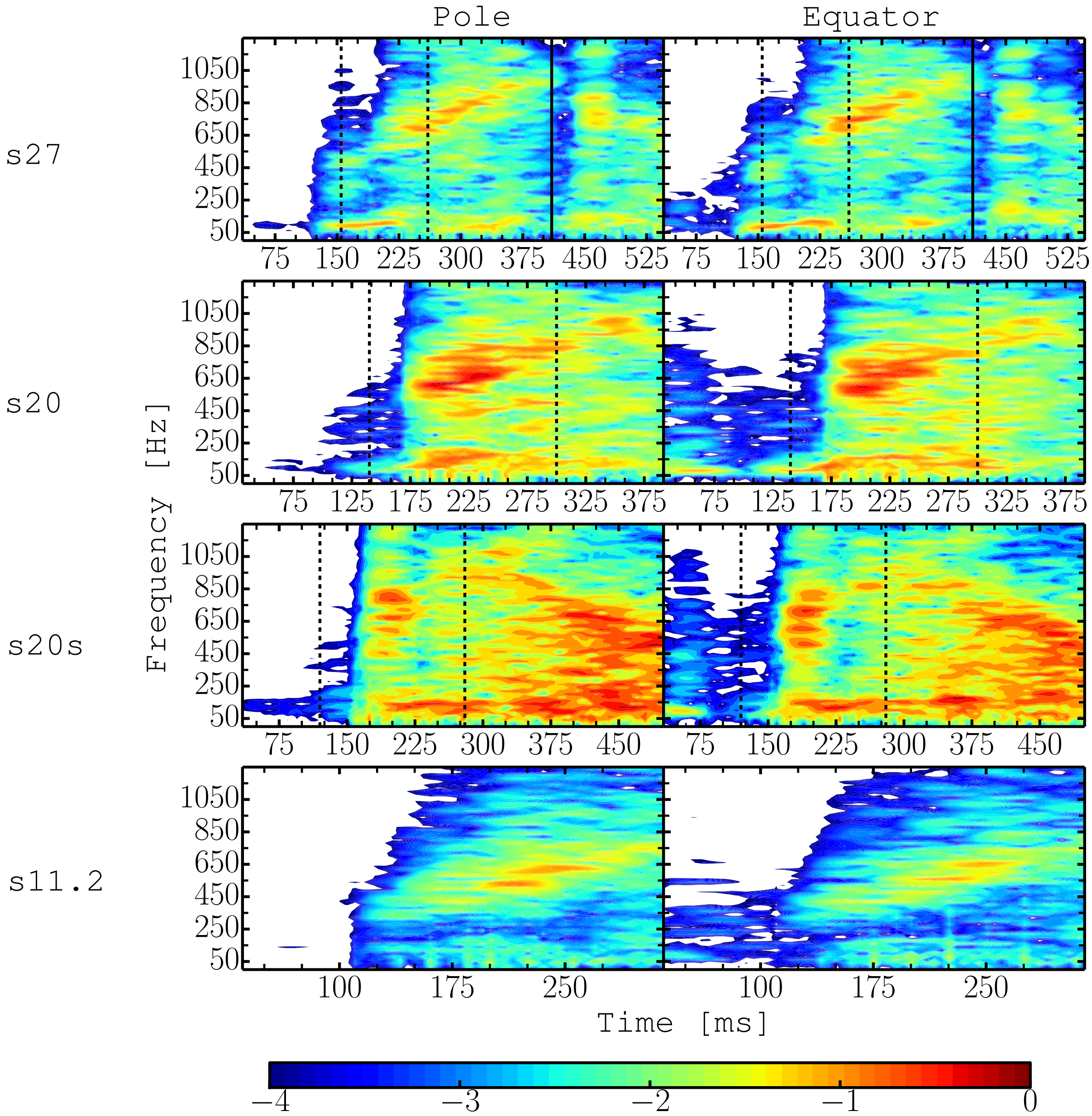

Figure 6.3.: Amplitude spectrograms for a sliding window of 50 ms and two different observer directions, summed over the two polarisation modes ($|\mathrm{STFT}[A_+]|^2 + |\mathrm{STFT}[A_\times]|^2$). The different rows show the results for models s27, s20, s20s, and s11.2. (top to bottom). The two columns shows the spectrograms for two different viewing angles, the right and left column represent observers situated along the z-axis (pole) and x-axis (equator) of the computational grid, respectively. The time is given in ms after core bounce. Vertical lines bracket SASI episodes. All panels have been normalised by the same global factor. The colour bar is given in a logarithmic scale.

in the convective layer. In the overshooting layer outside the PNS convection zone the situation is reversed, and f_m is positive as the overshooting, outward-moving plumes, are denser than their surroundings. In our calculations we include the overshooting region in layer A. To capture properly both the convective zone and the region of overshooting, we define the boundary between layer A and layer B as the radius where

$$f_m = 0.1 f_m^{\max}|_{r>r_{\max}}\,, \tag{6.4}$$

where $f_m^{\max}$ and $r_{\max}$ are the maximum value of the turbulent mass flux and the radius at which we find $f_m^{\max}$, respectively. This definition can be more easily understood with the help of a radial profile of f_m as shown in Fig. 6.5 for model s27 at a post-bounce time of 192 ms. Where necessary, we further distinguish between the convective layer (layer A1) and the overshooting layer (layer A2), which are separated by the radius where $f_m = 0$.

In Fig. 6.6,Fig. 6.7 and we plot the Fourier amplitudes of the GW amplitudes arising from each individual layer; these amplitudes are calculated from the full-time signal and for an observer situated at the pole, corresponding to the left column in Fig. 6.3. These figure has to be analysed with some care. Since we plot the square of the Fourier coefficients one can not add the values of layers A, B, and C together and recover the value for the total signal. In addition, artefacts can arise due to effects at the boundaries between layers, as in the case of model s20 (bottom panel of Fig. 6.6). There is an artificially strong peak at 160 Hz, particularly from layer B. We have confirmed that shifting the boundary between layers A and B inwards reduces this peak significantly. The exact values of the low-frequency amplitudes are sensitive to the boundary definition, but the fact that all three layers contribute to emission below 250 Hz is robust. The high-frequency component is less affected by such artefacts since the high-frequency emission is mostly confined to layer A.

The results of this dissection of the contributions to the integral in Eq. (2.38) are somewhat unexpected. The high-frequency emission mostly stems from aspherical mass motions in layer A and there is only a minor contribution from layer B, which has been posited as the crucial region for GW emission during the pre-explosion phase in works based on 2D simulations (Marek et al., 2009, Murphy et al., 2009, Müller et al., 2013). Aspherical mass motions in layer C hardly contribute to this component at all.

By contrast, *all three regions* contribute to the low-frequency signal (i.e. emission at frequencies lower than 250 Hz) to a similar degree. This is also surprising if the dominant frequency of this component appears to be set by the SASI as speculated before. In this case, one might expect that the fluid motions responsible for GW emission are propagating waves in layer C and perhaps layer B, where the conversion of vorticity perturbations into acoustic perturbations occurs in the SASI feedback cycle.

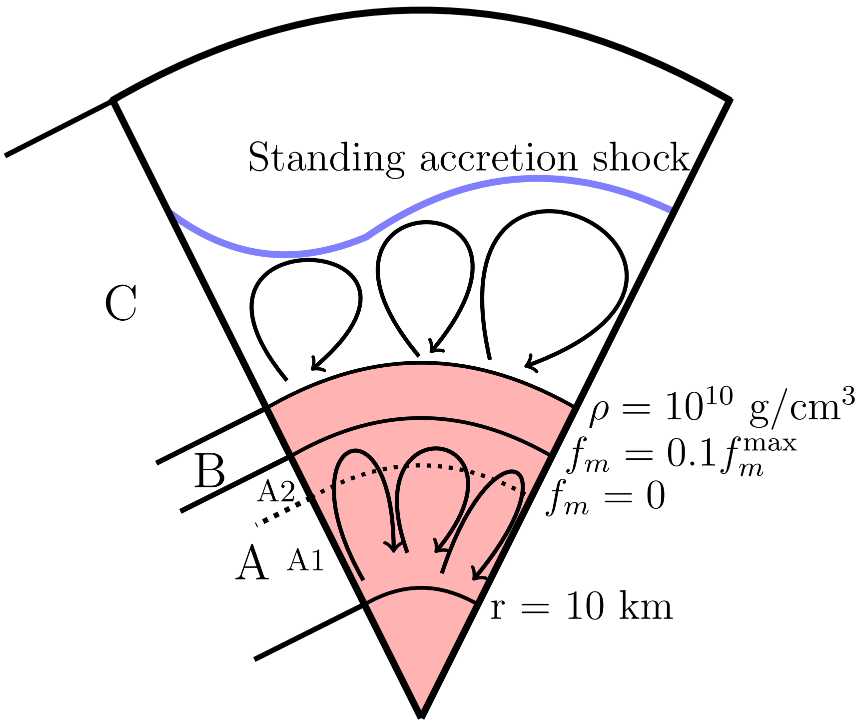

Figure 6.4.: Schematic overview of the regions of hydrodynamical activity. In Section 6.3.3 we investigate the contribution to the total GW signal from three different layers. The PNS, indicated by the shaded red area, is divided into two layers: Layer A includes the convectively unstable region in the PNS (layer A1) and the overshooting layer A2 directly above it. The boundary between the convective layer and the overshooting layer is indicated by a dashed curve within layer A. The second layer, layer B, extends from the top of the overshooting region and out to the PNS surface, defined by a fiducial density of $10^{10}\,\mathrm{g\,cm^{-3}}$. Layer C extends from the PNS surface to the outer boundary of our simulation volume. Layer C therefore includes the post-shock region, the standing accretion shock (indicated by the blue line), and the pre-shock region. Formal definitions of the boundaries between layers are given on the right hand side, see Section 6.3.3 for details.

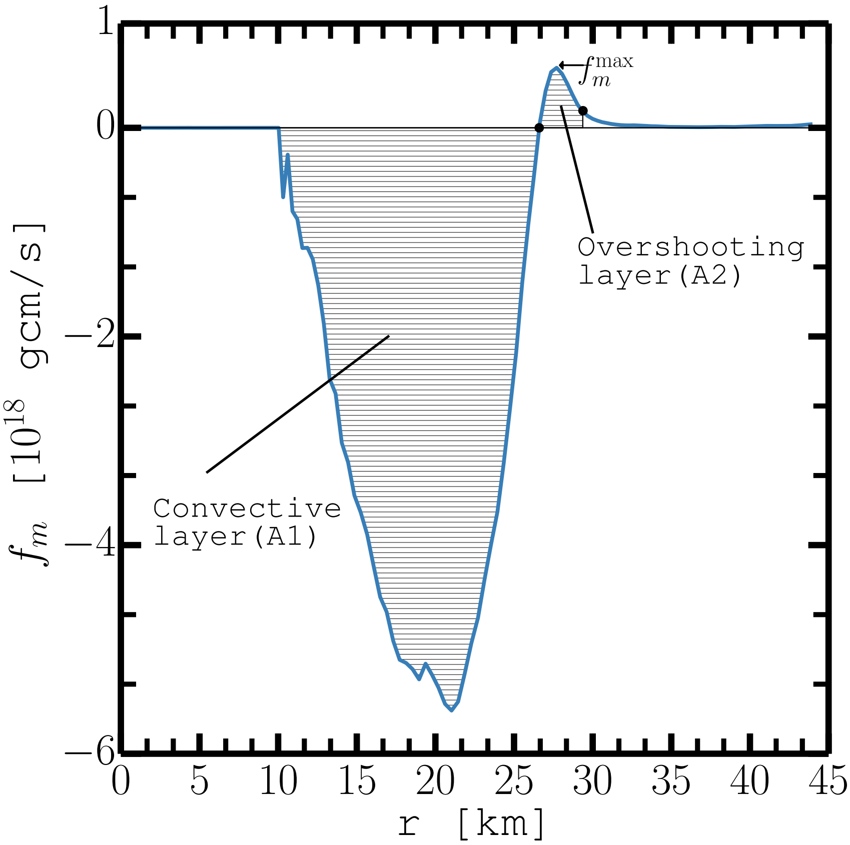

Figure 6.5.: Turbulent mass flux f_m (blue curve) for model s27, calculated 192 ms after core bounce. The shaded region indicates the convectively unstable region and the overshooting layer, which are lumped together as layer A (see Fig. 6.4).

6.3.4. Origin of high-frequency emission

What do these findings imply about the physical mechanisms that give rise to GW emission and determine their frequency? Let us first address the high-frequency signal. Recent 2D studies have connected GW emission at $\gtrsim$500 Hz to oscillatory modes (g-modes) excited either in the PNS surface (layer B) from above by downflows impinging onto the PNS (Marek et al., 2009, Murphy et al., 2009, Müller et al., 2013), or from below by PNS convection (Marek et al., 2009, Müller et al., 2012a; 2013). Prior to shock revival, the excitation of oscillations by mass motions in the gain layer was found to be dominant, with PNS convection taking over as the dominant excitation mechanism only after the onset of the explosion (Müller et al., 2012a; 2013). The typical angular frequency of such processes is roughly given by the Brunt-Väisälä frequency, N, in the convectively stable region between the gain region and the PNS convection zone,

$$N^2 = \frac{1}{\rho}\frac{\partial \Phi}{\partial r}\left[\frac{1}{c_s^2}\frac{\partial P}{\partial r} - \frac{\partial \rho}{\partial r}\right], \tag{6.5}$$

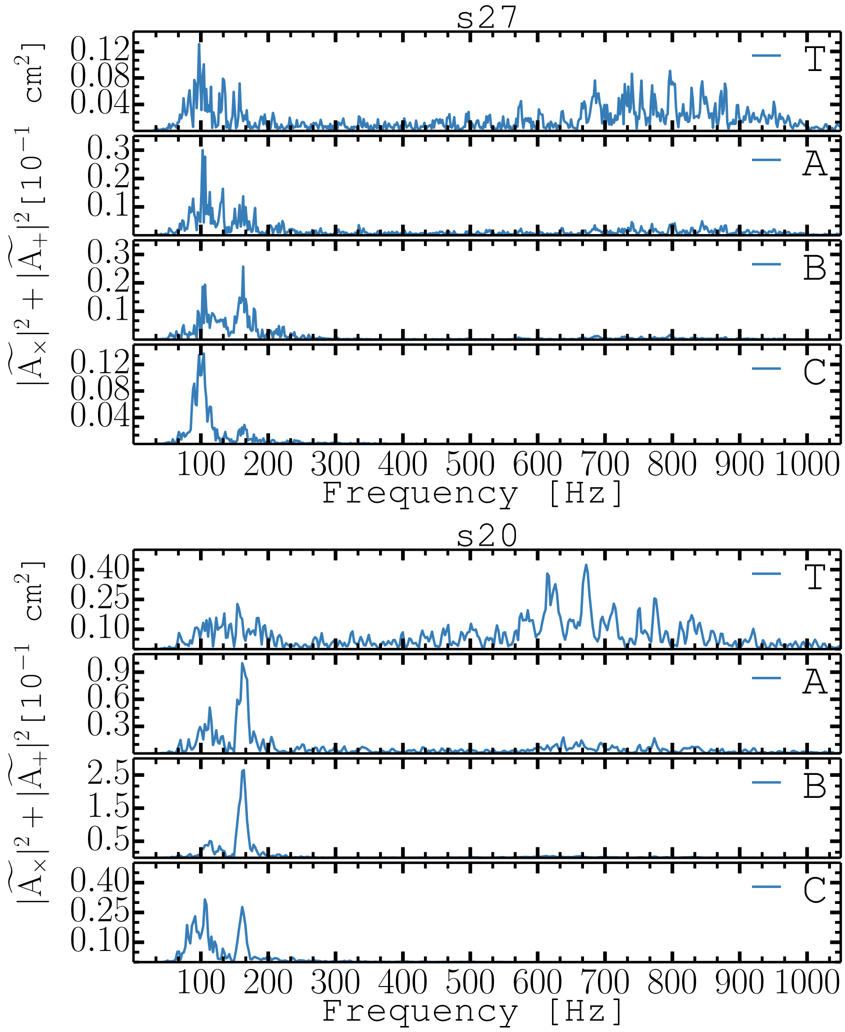

Figure 6.6.: Squared Fourier amplitudes of the total volume-integrated GW signal and of the signal contributions arising from the three different layers of the simulation volume. From the top: Total signal (T), the PNS convective region and the overshooting layer (A), the PNS surface layer (B), and the volume between the PNS surface and the outer grid boundary (C). From the top: models s27, and s20. See Fig. 6.4 for a sketch of the three regions used for this analysis. The Fourier amplitudes are calculated according to Eq. (2.44).

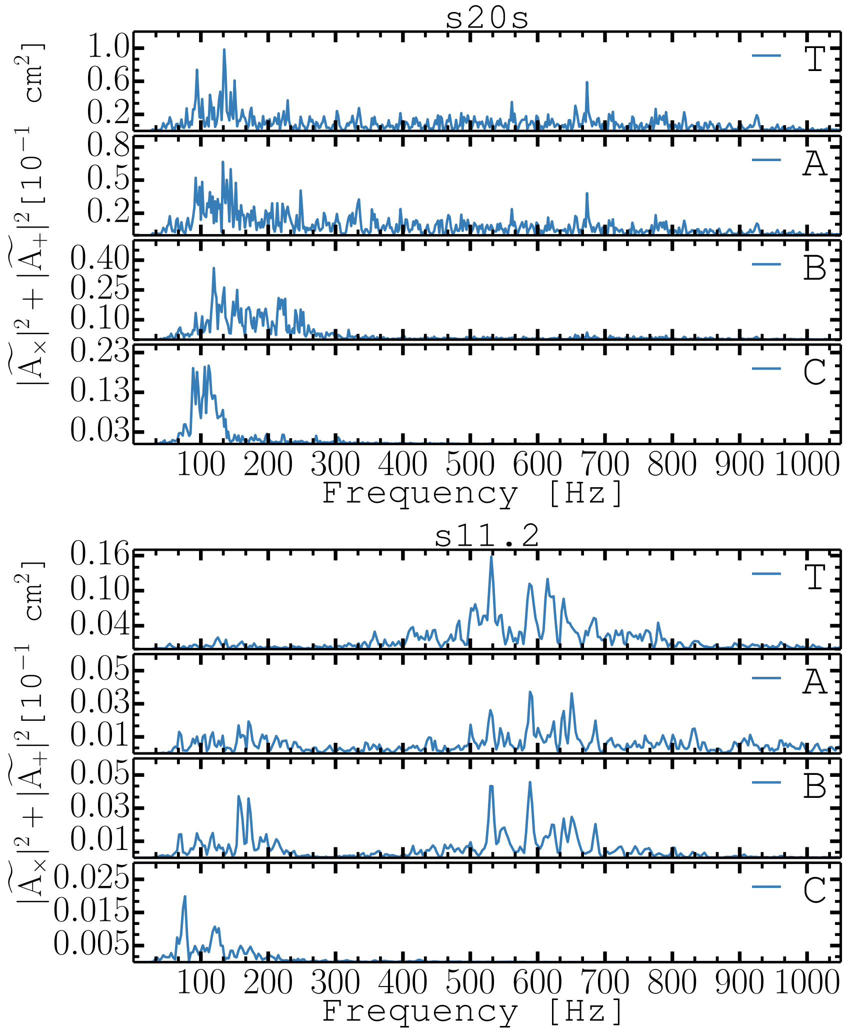

Figure 6.7.: Squared Fourier amplitudes of the total volume-integrated GW signal and of the signal contributions arising from the three different layers of the simulation volume. From the top: Total signal (T), the PNS convective region and the overshooting layer (A), the PNS surface layer (B), and the volume between the PNS surface and the outer grid boundary (C). From the top: models s20s, and s11.2. See Fig. 6.4 for a sketch of the three regions used for this analysis. The Fourier amplitudes are calculated according to Eq. (2.44).

where c_s is the sound speed. Müller et al. (2013) further investigated the dependence of this frequency on the mass M, the radius R, and the surface temperature T of the PNS to explain the secular increase of N during the contraction of the PNS and a tendency towards higher frequencies for more massive neutron stars.

Our results confirm that the peak frequency of the high-frequency GW emission is still set by the Brunt-Väisälä frequency in 3D and therefore point to a similar role of buoyancy forces in determining the spectral structure of the high-frequency component. As shown in Fig. 6.8 for model s27, we find very good agreement between the peak GW frequency, f_{peak}, and the Brunt-Väisälä frequency, N, calculated at the outer boundary of the overshooting layer (the boundary between layers A and B). Here, f_{peak} denotes the frequency with the highest Fourier amplitude above 250 Hz. Superficially, there appears to be a discrepancy at post-bounce times later than 400 ms, where f_{peak} seems to decrease again. This, however, is purely an artefact of the sampling rate of 0.5 ms in the simulations, which results in a Nyquist frequency of 1000 Hz. The peak frequency is therefore aliased into the region below 1000 Hz. If this is taken into account, there is in fact good agreement between the Brunt-Väisälä frequency of ∼1300 Hz and the aliased peak GW frequency of ∼700 Hz at the end of the simulation.

The dominant excitation mechanism for these oscillatory motions in layers A and B is, however, remarkably different from previous 2D models. While allowing for a minor contribution from PNS convection to the total signal during the pre-explosion phase, most of the signal in 2D is found to originate from oscillations in layer B that are excited by convective plumes and/or the downflows of the SASI (Marek et al., 2009, Murphy et al., 2009, Müller et al., 2013). In this case, one would expect that the excited oscillation modes have large amplitudes mostly in the surface layer and that this layer contributes significantly to the GW signal. This is not the case in 3D as shown by Fig. 6.6 and by Fig. 6.7. The dominant contribution from layer A rather suggests that oscillatory modes are predominantly excited from below by aspherical mass motions in the PNS convection zone and are confined mostly to the overshooting layer, which acts as frequency stabiliser. This assessment is also compatible with the temporal evolution of the amplitudes and the power in the spectrograms. The amplitudes (Fig. 6.1) show modest temporal variations after an initial GW-quiet phase of 150-200 ms and little response to strong activity of SASI and convection, which argues against efficient excitation of surface g-modes by motions in the gain region. The spectrograms (Fig. 6.3) point to the same conclusion, e.g. high-frequency emission is practically absent during the first phase of SASI activity in s27.

To confirm the crucial role of layer A2, we excluded this region from our analysis and found a large reduction of the energy carried away by high-frequency GWs,

$$E_{GW} \sim \int_{250\,\mathrm{Hz}}^{1100\,\mathrm{Hz}} \frac{\mathrm{d}E}{\mathrm{d}f}\,\mathrm{d}f. \tag{6.6}$$

For model s27, we find a reduction of the GW energy by roughly a factor of two when excluding the overshooting layer A2. It is remarkable that the deeper regions of the PNS

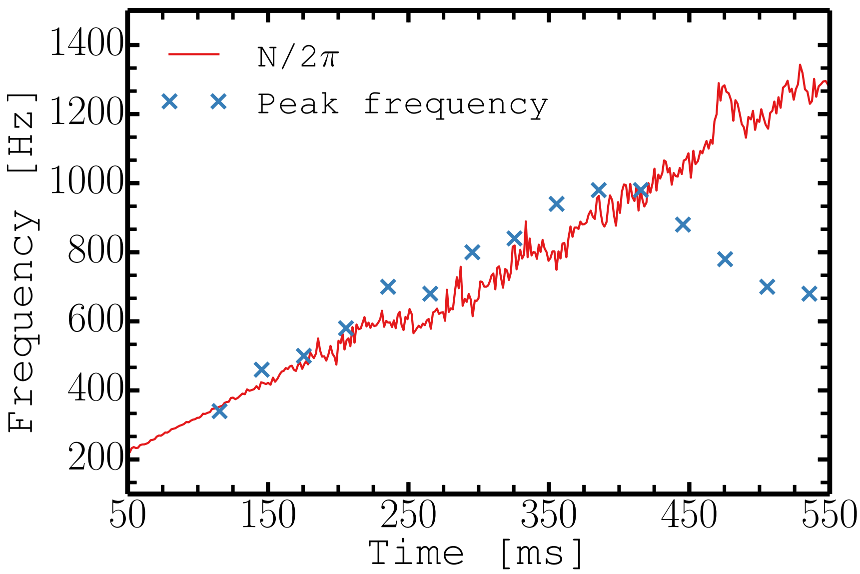

Figure 6.8.: Frequency of strongest GW emission above 250 Hz in the spectrogram of model s27 as a function of time (blue crosses). We also plot the expected characteristic frequency of GW emission excited by buoyancy effects in the PNS surface layer B and the overshooting layer A2 (red curve, see definition in Eq. (6.5). The exact value of N depends on the radius where Eq. (6.5) is evaluated, but we find similar numerical values within layers B and A2. Note that the trends seen for model s27 are common to all our models.

convection zone (layer A1) nonetheless contribute to the high-frequency signal with similar frequencies: There is no apparent reason for a correlation between the convective overturn time T_{conv} (which sets the natural frequency for GWs from the bulk of the PNS convection zone as $1/T_{\mathrm{conv}}$) and the Brunt-Väisälä frequency in the overlying stable region.

6.3.5. Comparison of high-frequency emission in two and three dimensions

To further illustrate the differences between previously published 2D waveforms and our 3D results, we re-analyse the GW signal from model G27-2D of Müller et al. (2013) using the STFT and the decomposition of the computational volume into three different regions. G27-2D is a 2D model based on the same $27M_{\odot}$ progenitor used in our simulations, with the same EoS and the same neutrino treatment, the only major difference being the treatment of GR: In G27-2D, the equations of radiation hydrodynamics in the ray-by-ray-plus approximation are solved in their general relativistic formulation assuming a conformally flat metric, whereas the pseudo-Newtonian approach of Marek et al. (2006) was used for model s27 in 3D. Fig. 6.11 shows the GW signal and amplitude spectrogram for model G27-2D. Fourier amplitudes for the signal from the three regions are shown in the bottom

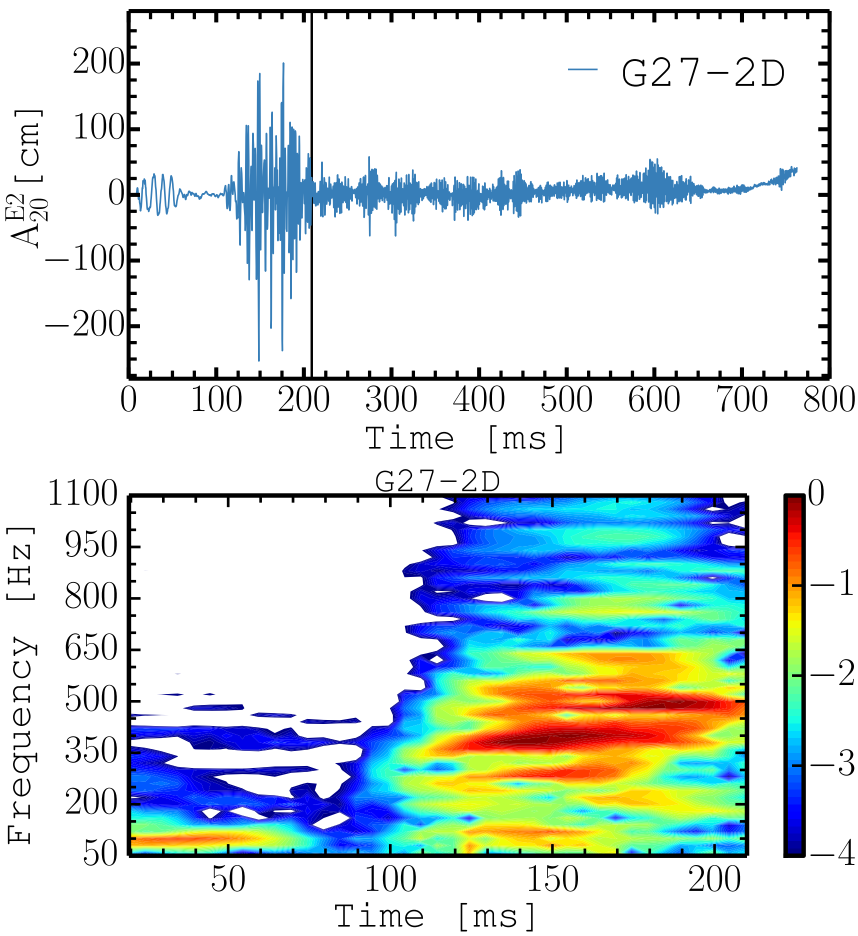

Figure 6.9.: The GW amplitude, A_{E2}^{20}, as a function of time after bounce (top) and amplitude spectrograms in in logarithmic scale (bottom) for the 2D model G27-2D. For a useful comparison with the corresponding non-exploding 3D model, we only show the spectrograms for the time between bounce and the onset of the explosion.

panel of Fig. 6.10 for the period up to the onset of the explosion 210 ms after bounce.

Comparing the spectrograms of model G27-2D with those of the 3D models (Figs. 6.3 and 6.11), we find that the "quiet zone" between the high-frequency and low-frequency components of the signal is not visible in model G27-2D, which is in agreement with the wavelet analysis of Müller et al. (2013) who also found a more broad-banded signal during phases of strong SASI and convection, with the Brunt-Väisälä frequency providing more of an upper limit rather than a sharply defined peak frequency during such phases. In model G27-2D, there is strong emission between 250 Hz and 750 Hz, and the relative contribution of the low-frequency signal below 250 Hz is smaller (which will be discussed in more detail in Section 6.3.6). The decomposition of the integration volume into three layers (bottom panel of Fig. 6.10) reveals that the main contribution to the high-frequency signal stems from the PNS surface (layer B). In addition to the broadband emission between 250 Hz

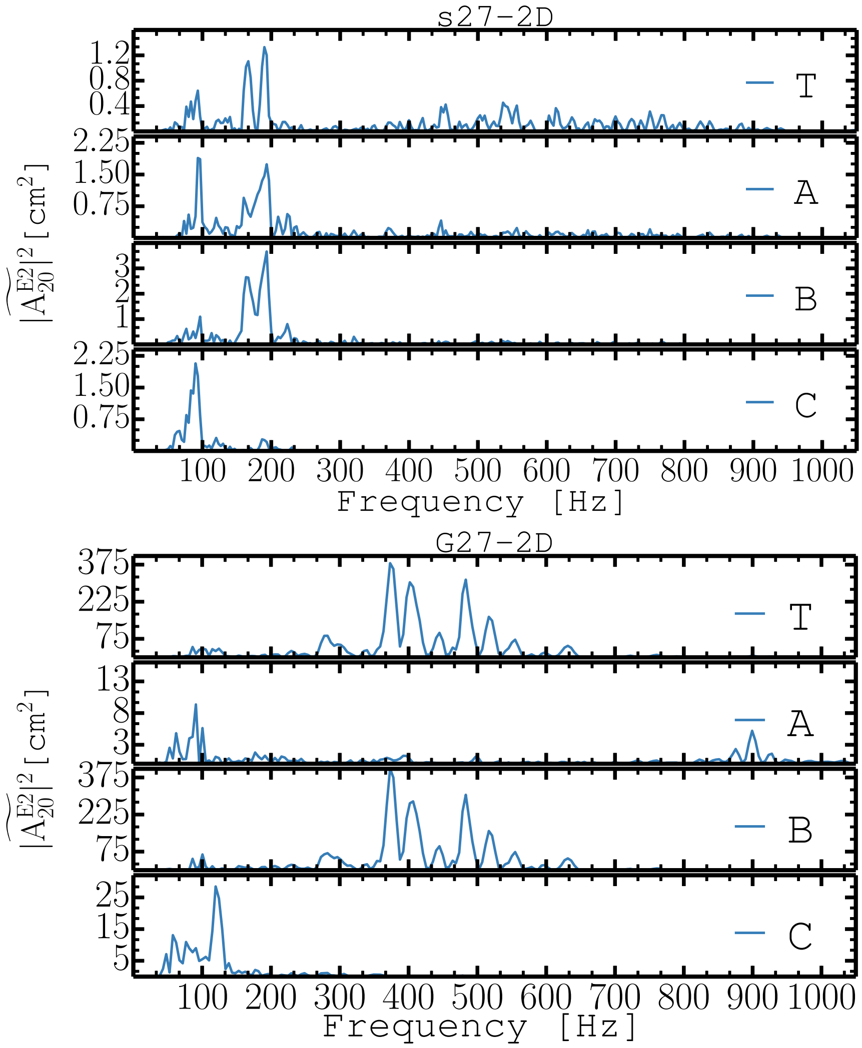

Figure 6.10.: Squared Fourier amplitudes of the total volume-integrated GW signal and of the signal arising from the three different layers of the simulation volume, for the 2D model G27-2D of Müller et al. (2013) (top) and s27-2D (bottom). From the top: total signal (T), layer A, layer B, and layer C. The Fourier amplitudes, $\widetilde{A^{20}_{E2}}$, are calculated based on Eq. (2.44), and Eq. (2.40).

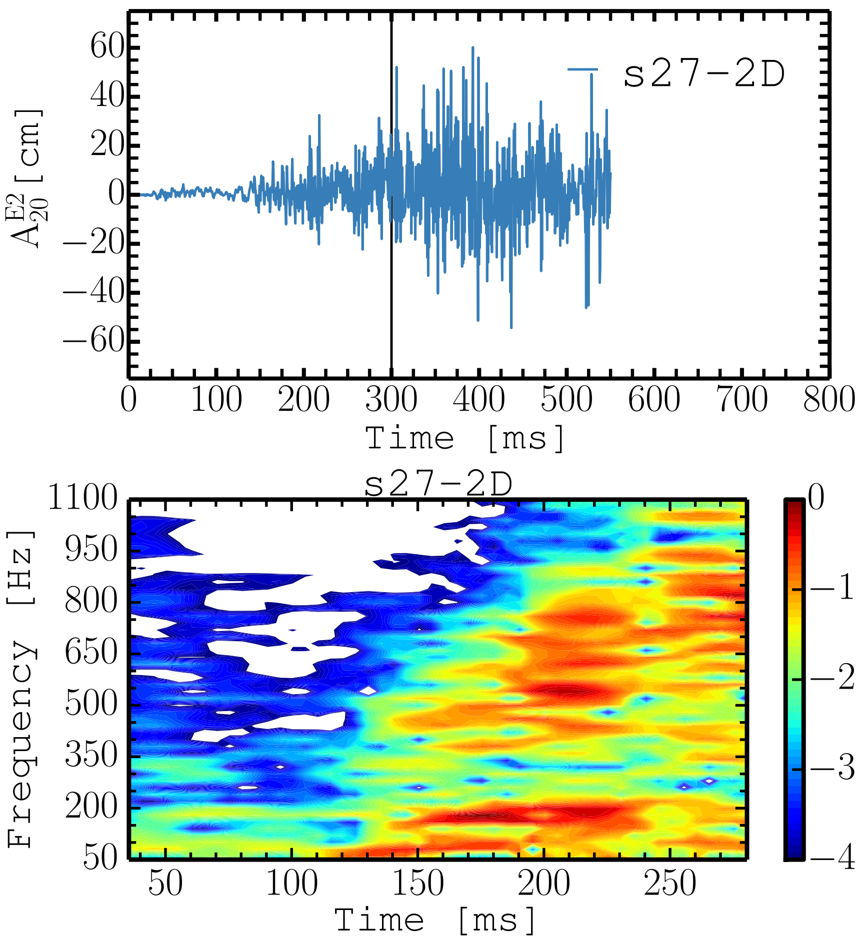

Figure 6.11.: The GW amplitude, A_{E2}^{20}, as a function of time after bounce (top) and amplitude spectrograms in in logarithmic scale (bottom) for the 2D model s27-2D. For a useful comparison with the corresponding non-exploding 3D model, we only show the spectrograms for the time between bounce and the onset of the explosion.

and 750 Hz, there are also two narrow emission peaks centred around 800 Hz and 900 Hz. This emission is the result of oscillations deep in the PNS core that are excited by PNS convection.

Different from model G27-2D and other recent 2D models found in the literature (Marek et al., 2009, Murphy et al., 2009, Müller et al., 2013), a 2D version of model s27 (model s27-2D, simulated with Prometheus-Vertex) more closely resembles the 3D models presented in our study during the pre-explosion phase (i.e. up to 300 ms after bounce) in terms of its spectrogram (top panel in Fig. 6.11) and time-integrated spectrum (left panel of Fig. 6.10). The spectrogram of the model (top panel of Fig. 6.11) shows the same two signal components that we found in our 3D models. There is a high-frequency and a low-frequency component and a frequency band separating the two components where the emission is much weaker (between 250 and 350 Hz). The *relative* contributions to the total signal from layers A, B, and C are roughly the same in models s27 and s27-2D (see top panel of Fig. 6.10 and top panel of Fig. 6.6). Judging from the time-integrated signals from the pre-explosion phase, the only noteworthy difference between models s27 and s27-2D appears to consist in an overall reduction of the amplitudes by about a factor of ten (or by a factor of 100 in squared amplitudes as shown in Figs. 6.6 and 6.10) in 3D (s27) compared to s27-2D in all regions across the entire spectrum.

The fact that the signal from layer B is not very strong in s27-2D makes it difficult to determine the impact of 2D effects on mode excitations by motions in the gain region as opposed to motions in the PNS convection zone. The modes excited by motions in the gain region need to be very strong for the emission from layer B to clearly stick out in time-integrated spectra as in G27-2D. The spectrograms, however, show that the excitation of surface g-modes by the SASI is more efficient in s27-2D than in the 3D model s27: In s27, significant emission in the high-frequency band is absent up to $\sim$210 ms after bounce despite strong SASI activity (which shows up in the low-frequency band), whereas s27-2D shows noteworthy emission in the high-frequency band during this phase. In 3D, we thus find i) a suppression of the signal originating from PNS convection (layer A) by a factor of ~ 10, and ii) an even more efficient suppression of any high-frequency GW emission due to mode excitation by the SASI in the spectrograms.

There are presumably several reasons why the excitation of oscillations in the PNS surface layer is found to be more efficient in 2D than in 3D. First, the inverse turbulent cascade (Kraichnan, 1967) and the suppression of the Kelvin-Helmholtz instability at the edge of supersonic downflows (see Müller 2015 and references therein) lead to an artificial accumulation of the turbulent energy on large scales in 2D supernova simulations (Hanke et al., 2012, Abdikamalov et al., 2015) and higher impact velocities of the downflows (Melson et al., 2015a, Müller, 2015). Thus, both the amplitudes as well as the mode overlap of the forcing with the excited $l = 2$ oscillation modes are higher in 2D. However, while the excitation of g-modes in the surface layer is strongly suppressed in 3D, there is still some residual g-mode activity (Melson et al., 2015a, Müller, 2015). Furthermore, we must also consider the frequency structure of the forcing. Fig. 6.12 shows considerable high-frequency emission from layer C in 2D, which is indicative of violent large-scale (i.e. with an $l = 2$ component) mass motions on time-scales considerably *shorter* than the SASI period or the convective overturn time-scale. The lack of such high-frequency GW activity from layer C in 3D indicates that the downflows in 3D are not as strongly distorted by intermediate-scale eddies and that they vary less on short time-scales. Fig. 4 of Melson et al. (2015a), which shows 2D and 3D simulations of a successfully exploding $9.6 M_\odot$ model, further illustrates this difference between the frequency structure of the post-shock flow in 2D and 3D: In 3D the angle-averaged radial velocity profiles of the infalling material appear smooth. On the other hand, intermediate-scale eddies with fast time variations are clearly visible in 2D. With a typical time scale on the order of $t \sim 1 \ldots 10$ ms, corresponding to a frequency range of $f \sim 100 \ldots 1000$ Hz, the eddies in 2D cause a more “impulsive” forcing with a broad frequency spectrum. The different frequency structure of the forcing in 2D and 3D is then reflected in the excited PNS surface oscillations: In 2D, where the frequency spectrum of the forcing overlaps with the natural g-mode frequency, we see *resonant* excitation of free (high-frequency) g-mode oscillations. This is not the case in 3D, but we still see strong *non-resonant* excitation of forced g-modes at low frequencies in the PNS surface (see Section 6.3.6).

It is noteworthy that some of these aforementioned effects (e.g. the different dynamics of supersonic downflows) depend on the Mach number of the flow and are therefore only relevant for the damping the excitation of surface g-modes by motions from the gain region. By contrast, Mach-number dependent effects like the inhibition of the Kelvin-Helmholtz instability in 2D will not affect the excitation of oscillation modes by PNS convection, which is strongly subsonic. This explains why 3D effects strongly quench g-mode excitation from SASI and hot-bubble convection, but lead to a more modest reduction of GW emission due to PNS convection, which therefore becomes the dominant source of high-frequency GW emission in our 3D models.

Without a 3D model corresponding to G27-2D, it is not yet possible to decide whether the suppression of surface g-mode excitation is *generically* strong enough to make it a subdominant source of GW emission. The critical feature in the post-shock flow that is responsible for strong GW emission from layer B in G27-2D is the development of very strong non-linear SASI activity with the presence of stable supersonic downflows, which reach Mach numbers of 1.5 already 110 ms after bounce. Since the coupling of perturbations in the gain region to the surface g-modes is more effective for high Mach number flow (cp. Goldreich & Kumar, 1990, Lecoanet & Quataert, 2013), and since the kinetic energy in non-radial motions reaches large values of up to 6×10^{49} erg (compared to pre-explosion values of $\lesssim 1.5 \times 10^{49}$ erg in s27 and s27-2D, cp. Hanke et al., 2013), the resulting GW amplitudes from surface g-modes in G27-2D are one order of magnitude larger than in s27-2D and two orders of magnituder larger than in s27, which only develops mildly non-linear SASI activity during the pre-explosion phase. The GW emission from layer B thus clearly dominates the time-integrated spectrum of G27-2D.

Under the conditions that obtain in model G27-2D (fully developed non-linear SASI/convection with high Mach numbers), 2D/3D differences in the behaviour of the downflows due to the inhibition of the Kelvin-Helmholtz instability in 2D tend to become more pronounced, which suggests that very little excitation of surface g-mode by the SASI may survive in 3D even for a model with similar dynamics to G27-2D. This will need to be confirmed by future 3D simulations, however.

6.3.6. Origin of the Low-Frequency Signal

The strong low-frequency signal seen in the more massive models (s20, s20s, s27) is apparently closely connected to SASI activity. Note that the convection-dominated s11.2 model

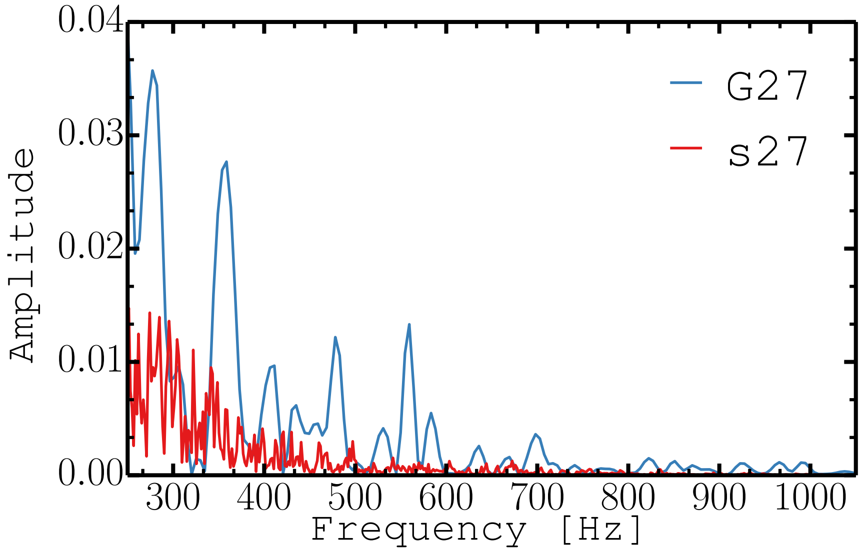

Figure 6.12.: Normalised Fourier amplitudes of the GW signal from layer C for the 2D model G27-2D and the 3D model s27. Each curve is normalised by its respective maximum to account for the difference in magnitude between 2D and 3D. Note that the maxima lie outside of the frequency domain shown in this figure.

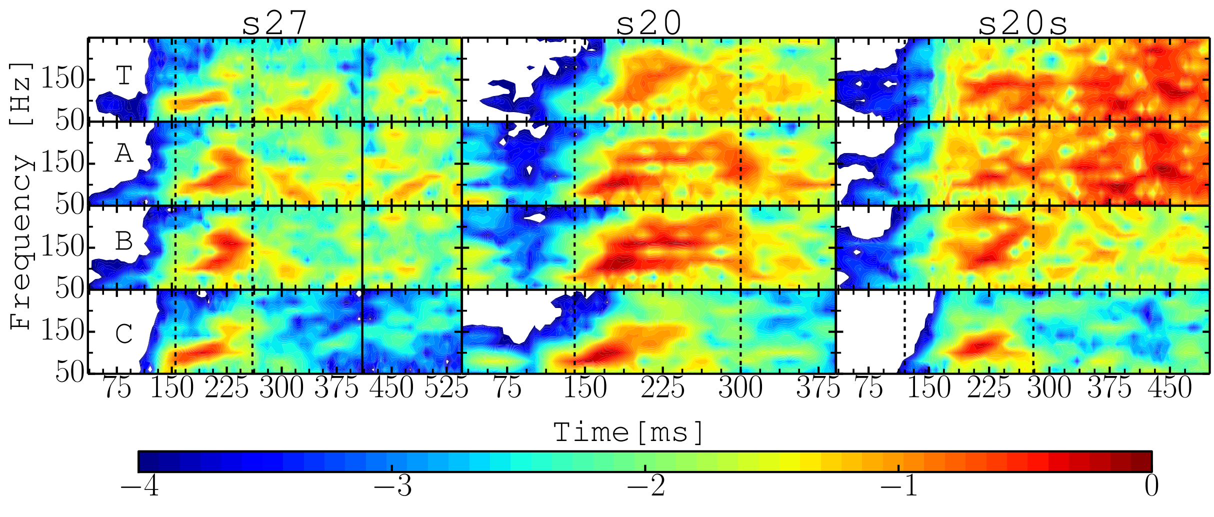

Figure 6.13.: Amplitude spectrograms, for a sliding window of 50 ms, of the low-frequency GW signal arising from the three different layers, summed over the two polarisation modes ($|\mathrm{STFT}[A_+]|^2 + |\mathrm{STFT}[A_\times]|^2$). From the top: total signal (T), layers A, B, and C. Columns are ordered by progenitor (left: s27, middle: s20, right: s20s). See Fig. 6.4 for a sketch of the three regions. The observer is chosen to be the north pole in the computational grid. As in Fig. 6.1 and Fig. 6.3, strong SASI episodes are bracketed by vertical lines. The colour scale is logarithmic and all panels have been normalised by the same global factor that has also been used for Fig. 6.3.

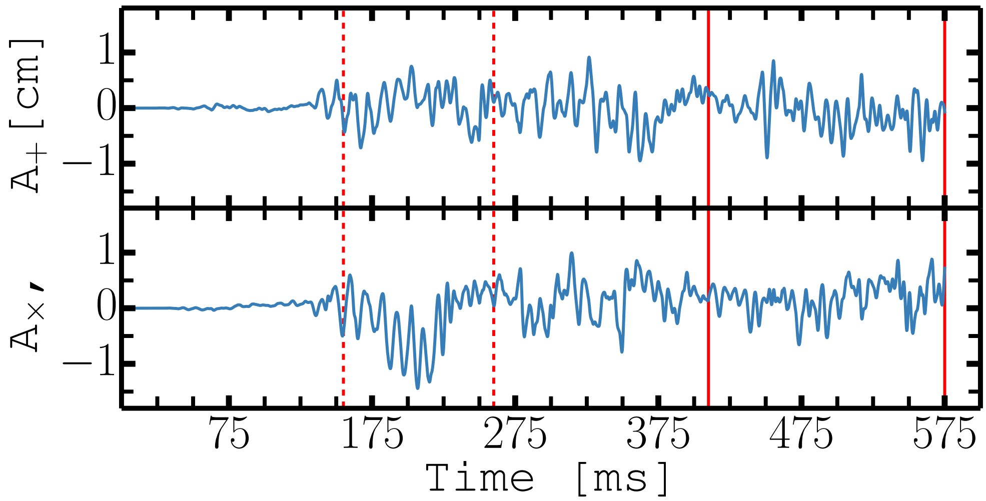

Figure 6.14.: The GW amplitudes A_+ and $A_\times$ of model s27, for an observer situated along the z-axis of the computational grid, after a low-pass filter has been applied. The time axis indicates time since core bounce.

show some stochastic low-amplitude GW emission at low frequencies (see Fig. 6.3), which is, however, much less pronounced compared to the high-frequency component. To address the origin of the low-frequency component, we show spectrograms of the GW signal below 250 Hz from each of the three analysis regions for models s20, s20s, and s27 in Fig. 6.13.

The apparent temporal correlation of the low-frequency emission with the SASI suggests the following plausible mechanism responsible for this component: Violent SASI involves the development of large-scale, large-amplitude density perturbations with the same temporal dependence as the shock oscillations. Such density perturbations $\delta\rho$ will directly contribute to the signal through the term $\rho x_i \partial_j \Phi$ in the integrand of the quadrupole formula (2.38) if the density perturbations $\delta\rho$ have an $l = 2$ (quadrupole) component $\delta\rho_2$.* Even $l = 1$ sloshing and spiral motions will develop a sizeable quadrupole component $\delta\rho_2$ in the non-linear phase. The frequency of the emitted signal will trace the frequency of the underlying SASI mode, but with frequency doubling for the $l = 1$ mode since the SASI-induced perturbation of the quadrupole moment will repeat itself after half a period as the integrand in Eq. (2.38) is invariant to a rotation by π in any direction. The contribution of the $l = 1$ and $l = 2$ modes (and possibly their overtones) explains the double-peak structure of the low-frequency signal in Figs. 6.3, 6.6, and 6.13. The amplitude arising from the term $\rho x_i \partial_j \Phi$ will be of order

$$A \sim \frac{G}{c^4} \int r \, \delta\rho_2 \frac{\partial \Phi}{\partial r} \mathrm{d}V \sim \frac{G}{c^4} \int \delta\rho_2 \frac{GM}{r} \mathrm{d}V. \tag{6.7}$$

The integral is essentially the potential energy stored in $l = 2$ density perturbations during

*Velocity perturbations will, in principle, also contribute in Eq. (2.38). Empirically, we find that their contribution to the GW amplitude is minimal, however.

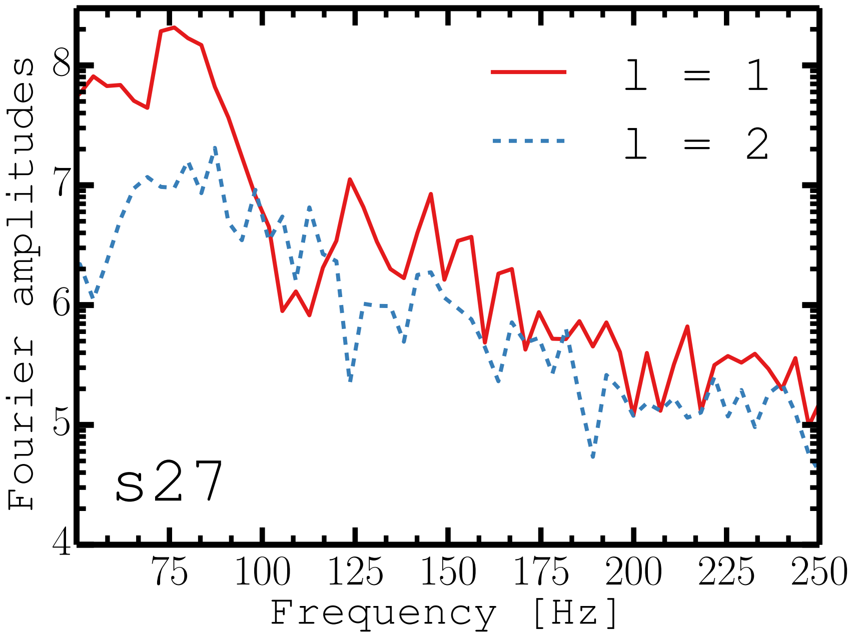

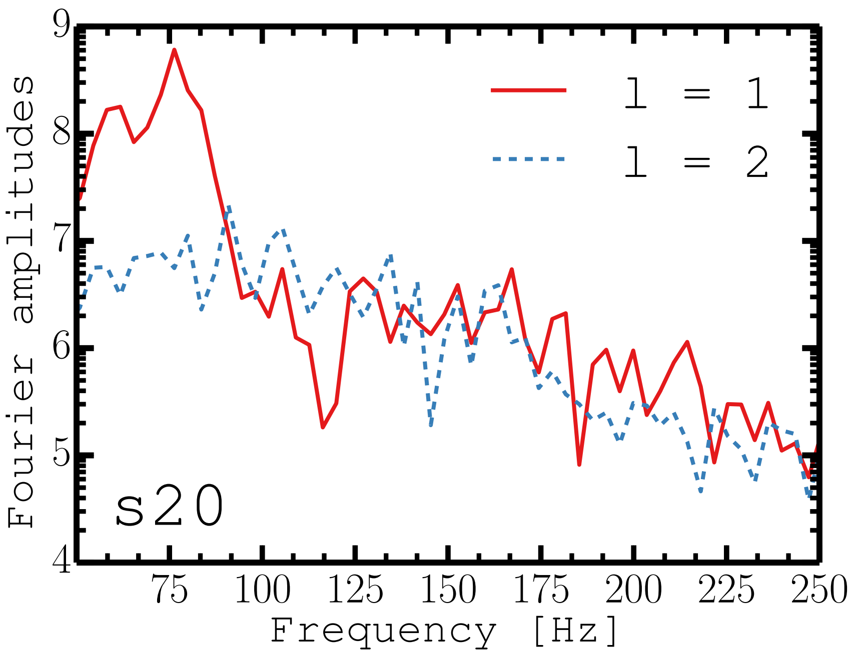

Figure 6.15.: Squared Fourier amplitudes, in logarithmic scale, for the $l = 1$ and $l = 2$ components of the expansion of the shock position into spherical harmonics. The Fourier amplitudes have been calculated for the time window between 100 ms and 350 ms after core bounce. The upper panel shows model s27 and the bottom panel the results for model s20. The curves in both panels have been normalised by the same factor.

SASI oscillations. Equating the potential energy with the kinetic energy in SASI motions and taking into account that there is only a finite overlap with $l = 2$, we find

$$A \lesssim \frac{G}{c^4} E_{\mathrm{kin,SASI}}. \tag{6.8}$$

With $E_{\mathrm{kin,SASI}} \sim 10^{49}\,\mathrm{erg}$, we obtain $A \lesssim 0.8\,\mathrm{cm}$, which is roughly compatible with the amplitudes (see Fig. 6.14).

The anisotropic modulation of the accretion by the SASI is further communicated to the PNS as material is advected downwards and settles onto the PNS surface (something which may also be viewed as non-resonant excitation of g-modes far below their eigenfrequency). As matter seeps deeper into the outer layer of the PNS (layer B) and then even further down into the interior of the PNS (layer A), it will still emit GWs if the density and entropy perturbations are not washed out completely by neutrino cooling. We have verified that relatively large density fluctuations on the percent level are maintained even in the cooling region. Since these density fluctuations still retain a temporal modulation set by the SASI, they emit GWs in a similar, albeit somewhat broader frequency range. For the same reasons as detailed above, the GWs amplitudes produced by such a non-resonant excitation of g-modes will be related to the kinetic energy stored in the mode and even a small kinetic energy $\gtrsim 10^{48}\,\mathrm{erg}$ in aspherical mass motions below the gain region is sufficient to account for the amplitudes.

The fact that the low-frequency signal from layer C is *weaker* than that from both layer A and layer B is not in conflict with this explanation because of cancellations in the integral of $\rho\,(v_i v_j - x_i \partial_j \Phi)$ over the region outside the PNS, e.g. the overdensities in the downflows can be compensated by the smaller shock radius above them.* Furthermore, we surmise that density perturbations from the $l = 1$ contribute more strongly to the GW signal as they settle deeper into the PNS, because the pure $l = 1$ angular dependence of the perturbations in the post-shock region develops a larger $l = 2$ component during the process of settling.

The crucial role of the SASI in providing a slow, non-resonant forcing of the outer regions of the PNS is also reflected in the frequency structure of the signal. In Fig. 6.15 we plot the Fourier amplitudes of the $l = 1$ and $l = 2$ components of the spherical harmonics decomposition of the shock position for the period between 100 ms and 350 ms after bounce. More precisely Fig. 6.15 shows

$$\sum_{m=-l,l} |\widetilde{a}_l^m(t)|^2 \quad (l = 1, 2), \tag{6.9}$$

where $\widetilde{a}_l^m(t)$ is the Fourier transform of

$$a_l^m(t_n) = \frac{(-1)^{|m|}}{\sqrt{4\pi(2l+1)}} \int r_{\mathrm{sh}}(\theta, \phi, t) Y_l^m \mathrm{d}\Omega. \tag{6.10}$$

*Immediately outside the minimum shock radius, the densities of unshocked material above the downflows are *lower* than in the shocked material inside the high-entropy bubbles *at a given radius*, i.e. overdensities behind the shock correspond to underdensities at larger radii.

Here, r_{sh} is the shock position (given by the Riemann-solver in our code) and Y_l^m is the spherical harmonic of degree l and order m. Details about the shock can be found in Hanke et al. (2013) for model s27, in Hanke (2014) for models s11.1 and s20 and in Melson et al. (2015b) for model s20s. The typical frequency for the $l = 1$ mode ($50 \ldots 100\,\mathrm{Hz}$) and the $l = 2$ mode ($100 \ldots 160\,\mathrm{Hz}$) of the shock are compatible with the range of low-frequency emission seen in the GW spectrograms, especially if we account for the fact that the GW signal from forced $l = 1$ motion will exhibit frequency doubling.

Since the Fourier spectra of the $l = 1$ and $l = 2$ modes as well as the GW spectrogram point towards a complicated frequency structure with peak frequencies shifting in time (due to the variation of the shock radius which sets the SASI frequencies) and contributions from different phases interfering with each other in the time-integrated spectrum, we refrain from a precise one-to-one identification of the underlying modes.

It is noteworthy that the effect of anisotropic accretion manifests itself even down to the PNS convective layer. Apparently, the eigenfunctions of the excited modes reach down quite deep through the entire surface of the PNS (layer B). However, the fact that even the deeper region of layer A (below the overshooting region) contributes to low-frequency GW emission suggests that $l = 1$ and $l = 2$ surface motions can trigger convective motions (e.g. by providing density perturbations that are then quickly amplified once they are advected into the convectively unstable region). Contrary to the mirror problem of wave excitation at convective boundaries (Goldreich & Kumar, 1990, Lecoanet & Quataert, 2013), such a coupling between the accretion flow, the surface layer, and the PNS convection has as yet been poorly explored.

While the SASI is particularly effective at generating a modulation of the accretion flow with a sizeable $l = 2$ component, large-scale convective motions in the hot-bubble region can also act as a substitute for the SASI during periods of transient shock expansion (because the typical scale of convective eddies is set by the width of the unstable region, cp. Chandrasekhar, 1961, Foglizzo et al., 2006). The result is a somewhat weaker and less sharply defined low-frequency signal, which is what we observe during the SASI-quiet periods in models s20s, s20, and s27 and also in model s11.2 (cf. Fig. 6.3).

With large-scale fluid motions in the gain region as the ultimate agent responsible for low-frequency GW emission (through forced PNS oscillations), the temporal structure of this signal component finds a natural explanation. Generally, episodes of strong SASI activity correlate with strong low-frequency GW activity. Large amplitudes of the shock oscillations are not sufficient, however; the determining factor is the kinetic energy contained in large-scale motions. For that reason, there is hardly any low-frequency emission component during the second SASI episode in model s27. During this phase, less mass is involved in SASI motions and the SASI amplitude is significantly smaller. The lack of large-scale motions with a significant $l = 2$ component also explains the weak low-frequency GW activity in model s11.2, where the post-shock flow is dominated by smaller convective bubbles and the kinetic energy in non-radial fluid motions is typically smaller than for the more massive progenitors.

6.3.7. Comparison of the exploding and non-exploding 20 solar mass models

The exploding model s20s differs only in details from its non-exploding counterpart during the accretion phase. After the onset of shock expansion strong low-frequency emission is sustained until the end of the simulation (see Fig. 6.13). This emission is connected to mass motions with a strong $l = 2$ component in layer A. In Fig. 6.16 we plot for models s20 and s20s,

$$\alpha_l = \sum_{m=-l}^{l} |\alpha_l^m(t)|^2 \quad , (l = 1, 2), \tag{6.11}$$

with

$$\alpha_l^m(t) = \frac{(-1)^{|m|}}{\sqrt{4\pi(2l+1)}} \int v_r(\theta, \phi, t) Y_l^m \mathrm{d}\Omega, \tag{6.12}$$

where v_r is the radial velocity at a radius R corresponding to an spherically averaged density of $\rho(R) = 9.5 \times 10^{13}\,\mathrm{g\,cm^{-3}}$.

In the exploding model, the $l = 2$ mode is generally stronger than in the non-exploding model and it remains strong throughout the simulation in contrast to the non-exploding model, where the $l = 2$ mode decreases in strength after the SASI-dominated phase ends. After a period of decreasing strength around 400 ms, the quadrupole mode in model s20s increases in strength and reaches amplitudes similar to those seen during the pre-explosion phase. At the same time, there is a shift in the relative strength of the $l = 1$ and $l = 2$ mode after the onset of shock expansion, While the quadrupole mode increases in strength, the dipole is relatively weak at late times. This transition into a flow pattern that is dominated by an $l = 2$ mode resonates better with the quadrupole nature of GW emission. We therefore see an increase in low-frequency emission from the unstable layer within the PNS. Such a change in the spectrum of eddy scales after shock revival could result from changes in the asymmetric accretion flow onto the PNS, or from changes in the stratification of entropy and electron fraction, but for the purpose of interpreting the GW emission, the ultimate reason is immaterial and left to more detailed future studies of the hydrodynamics of PNS convection. Aliasing of high-frequency emission may also be partly responsible for the enhanced low-frequency emission after shock revival. However, since the spectrograms in Fig. 6.3 show broadband emission, it is unlikely that the low-frequency emission we see after shock revival is caused by aliasing effects alone.

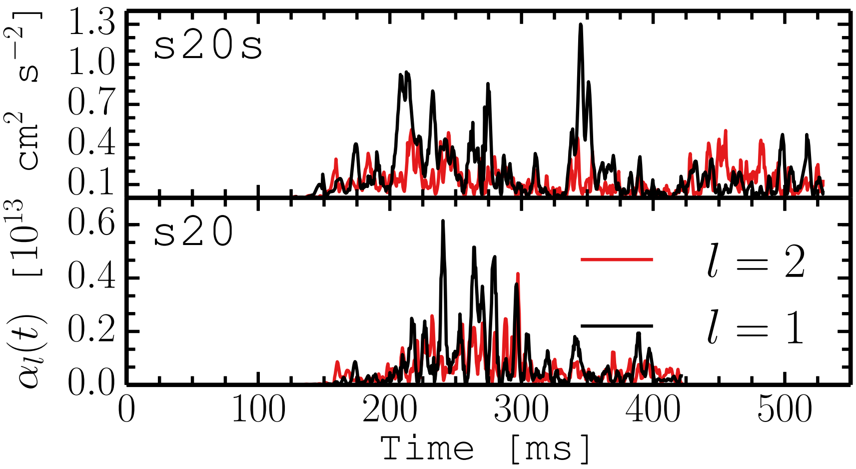

Figure 6.16.: The $l = 2$ and $l = 1$ components of the radial velocity sampled in the unstable PNS layer for the $20M_\odot$ models. The radial velocity has been sampled at a radius R given by $\rho(R) = 9.5 \times 10^{13}\,\mathrm{g\,cm^{-3}}$. The top panel shows the exploding model s20s, and the bottom panel shows the non-exploding model s20, which was only calculated to 421 ms after core bounce.

6.4. Detection prospects

With the prominent high-frequency component of the signal in 2D largely muted in 3D, it is evidently necessary to reconsider the prospects of detecting a Galactic supernova. Detailed detectability studies based on 2D waveforms (Logue et al., 2012) may now well be too optimistic after the update of the waveform predictions. While an elaborate statistical machinery is required to reliably determine signal detectability and possible inferences about core-collapse supernova physics (Logue et al., 2012, Hayama et al., 2015), we can already draw some conclusions for the waveforms presented in this paper.

6.4.1. General considerations

The detectability of the GW signal from a core-collapse supernova has often been assessed using the signal-to-noise ratio (SNR) for matched filtering. Assuming an optimally-orientated detector and a roughly isotropic frequency spectrum for different observer directions, the SNR for matched filtering is formally given by (Flanagan & Hughes, 1998,cp. their Eq. (5.2) for the second form),

$$(\mathrm{SNR})^2 = 4\int_0^\infty df \frac{|\tilde{h}(f)|^2}{S(f)} = \int_0^\infty df \frac{h_c^2}{f^2 S(f)}, \qquad (6.13)$$

Table 6.1.: Signal-to-noise ratio (SNR) for all four models. Values are given for two different frequency domains, 20 . . . 250 Hz (low-frequency) and 250 . . . 1200 Hz (high-frequency). The table shows values for two different detectors, AdvLIGO and the Einstein Telescope. For the latter we calculate the SNR for two different modes of operation (ET-B and ET-C). SNRs have been computed for a source at a distance of 10 kpc. For model s20s we only show the SNR for the low-frequency band since the high-frequency band is somewhat contaminated by aliasing effects. For s27, s20, and s11.2 we also give the ratio of the band-limited SNRs in the low- and high-frequency bands to quantify the "colour" of the GW signal.

s27	Low	High	Total	Low/High
AdVLIGO	3.7	4.5	8.8	0.82
ET-C	50.0	64.0	81.3	0.78
ET-B	78.5	73.7	107.7	1.07

s20	Low	High	Total	Low/High
AdVLIGO	7.7	9.4	0.82	0.32
ET-C	109.3	131.9	0.83	0.36
ET-B	127.0	170.6	0.74	0.42

s20s	Low	High	Total	Low/High
AdVLIGO	10.2	–	–	–
ET-C	139.7	–	–	–
ET-B	217.3	–	–	–

s11.2	Low	High	Total	Low/High
AdVLIGO	1.3	4.1	4.3	0.32
ET-C	18.1	50.9	53.9	0.35
ET-B	28.0	67.3	72.8	0.41

where

$$h_c = \sqrt{\frac{2G}{\pi^2 c^3 D^2}\frac{dE_{\mathrm{GW}}}{df}} \tag{6.14}$$

is the characteristic strain, $S(f)$ is the power-spectral density of the detector noise as a function of frequency f, and dE_{GW}/df is the spectral energy density of the GWs. Note that the second expression for the SNR in Eq. (6.13) has been obtained under the assumption of isotropic GW emission so that one can express the (formally) direction-dependent squared amplitudes in terms of the GW energy spectrum dE_{GW}/df.

Since the GW signal of a core-collapse supernova is, however, *not amenable to matched filtering* because of its stochastic character, the SNR formally defined by Eq. (6.13) must be interpreted with care.

The SNR still remains a useful quantity as it measures the excess power during the time of integration, as can be seen by re-expressing Eq. (6.13) in terms of the expectation value for the Fourier coefficients $\tilde{n}(f)$ of the noise over a finite time-interval Δt (the integration time for the signal), which obey (cp. Logue et al., 2012)

$$\langle \tilde{n}(f)\tilde{n}^*(f)\Delta f\rangle = S(f)/2, \tag{6.15}$$

where the factor 1/2 appears because $S(f)$ is defined as the one-sided power spectral density of the time-dependent strain noise $n(t)$. Note that the frequency spacing Δf is given by $\Delta f = 1/\Delta t$ and that Δt can be set to the length of the signal in consideration in our case. For a finite time series, where the integral in Eq. (6.13) can be replaced with a sum over the Fourier modes at discrete frequencies $f_k = k/\Delta t$ (with integer k), we then obtain,

$$(\mathrm{SNR})^2 = 8\sum_k \frac{|\tilde{h}(f_k)|^2\Delta f}{\langle|\tilde{n}(f_k)|^2\rangle\Delta f} = 8\sum_k \frac{|\tilde{h}(f_k)|^2}{\langle|\tilde{n}(f_k)|^2\rangle}. \tag{6.16}$$

For uncorrelated Gaussian noise in each frequency bin, the SNR of a prospective signal obtained from the summation over N_{bins} frequency bins is thus related to the χ^2-value for this signal as

$$\chi^2 \sim N_{\mathrm{bins}} + \mathrm{SNR}^2/2, \tag{6.17}$$

where the additional term N_{bins} comes from the contribution of the noise in each bin. Sufficiently high values of χ during a prospective supernova event (with an integration interval Δt defined by a coincident neutrino signal)* can be attributed to a physical signal; e.g. to exclude stochastic fluctuations as a source of the excess power at a confidence level of 95%, one needs

$$\mathrm{SNR}^2/8 = \chi^2 - N_{\mathrm{bins}} \gtrsim 2.3\sqrt{N_{\mathrm{bins}}} \tag{6.18}$$

*This is crucial because it is always possible to find short intervals with power excess comparable to a physical signal if the integration time is sufficiently long.

for large $N_{\rm bins}$. For a signal with power excess in a frequency band with bandwidth δf and $N_{\rm bins} = \delta f/\Delta f = \delta f\,\Delta t$, this implies the requirement

$$\mathrm{SNR} \gtrsim 4.3\,(\delta f\,\Delta t)^{1/4}, \tag{6.19}$$

for a detection of a signal in this band. This roughly corresponds to the results obtained by Flanagan & Hughes (1998) for noise monitoring in Section IIB of their paper.

Prior knowledge of the signal structure can help to identify signals with even lower SNR; Logue et al. (2012), for example, showed that a detection and identification can be possible already for SNR ~ 10 with the help of a principal component analysis of template waveforms provided that the signal structure is not too dissimilar from the template. This is in line with the weak dependence of Eq. (6.19) on the bandwidth δf.

If properly interpreted, the SNR thus remains a useful measure for the detectability of our predicted signals within the scope of this paper. Its inherent limitations provide justification for neglecting the effect of the detector orientation and the precise directional dependence of the signal by computing the SNR from the energy spectrum dE/df instead of a direction-dependent Fourier spectra of the strain. We have verified that the SNR for the low-frequency band does not vary by more than $\sim$20%, and the SNR for the high-frequency signal depends even less on the observer direction.

6.4.2. Detection prospects for simulated models

We calculate the SNR from Eq. (6.13) for the zero-detuning-high power configuration of Advanced LIGO (LIGO Laboratory & Shoemaker, 2010) and the B (Hild et al., 2008) and C (Hild et al., 2010) configurations for the Einstein telescope. We refer to these configurations as AdvLIGO, ET-B and ET-C. In order to better assess the detectability and possible inferences from the signal structure, we compute SNRs quantifying the excess power in a low-frequency band ($\mathrm{SNR}_{\rm low}$ for $20\,\mathrm{Hz} \leq f < 250\,\mathrm{Hz}$, i.e. $\delta f = 230\,\mathrm{Hz}$) and a high-frequency band ($\mathrm{SNR}_{\rm high}$ for $250\,\mathrm{Hz} \leq f < 1200\,\mathrm{Hz}$, i.e. $\delta f = 950\,\mathrm{Hz}$). SNRs for all models in those two bands for events at a distance of 10 kpc are presented in Table 6.1. Using Eq. (6.19), we obtain a detection threshold of $\mathrm{SNR}_{\rm low} \gtrsim 11$ for the low-frequency band and $\mathrm{SNR}_{\rm high} \gtrsim 15$ for the high-frequency band assuming $\Delta t = 0.5\,\mathrm{s}$. Since the critical SNR depends weakly on Δt, these fiducial values can be used for all models. SNRs for arbitrary distances can easily be obtained since the SNR is inversely proportional to the distance.

Regardless of the precise detector configuration, the SASI-dominated models s20 and s27 are clearly distinguished from the convective model s11.2 through a higher ratio $\mathrm{SNR}_{\rm low}/\mathrm{SNR}_{\rm high} > 0.65$ compared to $\mathrm{SNR}_{\rm low}/\mathrm{SNR}_{\rm high} < 0.42$. SASI-dominated models thus appear "redder" in GWs before the onset of the explosion. Based on our small sample, they also appear to be characterised by a higher SNR, but this might be incidental.

More massive progenitors with stronger neutrino heating in the gain region, stronger cooling above the PNS convection, and a larger mass in the gain region could produce a stronger GW signal, even in the absence of strong SASI activity. The ratio $\mathrm{SNR}_{\mathrm{low}}/\mathrm{SNR}_{\mathrm{high}}$, on the other hand, should be a robust indicator for the presence or absence of large-scale SASI motions.

Note that since model s20s suffers most severely from aliasing effects, the SNR in the high-frequency domain might be inaccurate. We therefore refrain from giving values for $\mathrm{SNR}_{\mathrm{high}}$ and the total SNR. The low-frequency band, on the other hand, should be unaffected by aliasing artefacts and $\mathrm{SNR}_{\mathrm{low}}$ is significantly higher than in the non-exploding models. It is possible that the enhanced low-frequency emission from the convectively unstable region of the PNS is a general feature in exploding models and we hypothesise that shock revival will be followed by GW emission with *excess power in the low-frequency band.* This is in contrast to previous studies in 2D (Murphy et al., 2009, Müller et al., 2013) where shock expansion is typically followed by an *increase in the high-frequency emission band.* If shock revival generally leads to enhanced low-frequency emission, this would obviously complicate the interpretation of a high value of $\mathrm{SNR}_{\mathrm{high}}/\mathrm{SNR}_{\mathrm{low}}$, which could *either* indicate SASI activity or the transition to an explosion.

6.4.3. Detection prospects with AdvLIGO

For a supernova at a distance of 10 kpc, it is evident that *none* of the four models could be detected by AdvLIGO based on excess signal power. Given the reduction of the typical amplitudes by a factor of $\sim$10 in 3D compared to 2D, this is not surprising. Using an approach based on simulated noise and a principal component analysis of the signal, Logue et al. (2012) and Gossan et al. (2016) already found that AdvLIGO is only marginally able to identify waveforms from 2D supernova simulations for events at distances of a few kpc.

For the SASI-dominated models (s20, s27, s20s), the excess power in the low-frequency band would become detectable at 95% confidence level at the distance of the Crab supernova ($\sim$2 kpc), as would the high-frequency component of model s20. Model s11.2, on the other hand, would not show a statistically significant power excess.

6.4.4. Detection prospects with the Einstein telescope

The situation will change drastically with the Einstein Telescope. For either configuration considered here, the excess power in both bands ought to be detectable for an event at a distance of 10 kpc, although the low-frequency component of model s11.2 would barely make it above the detection threshold for ET-C. The high SNR in both bands would permit a measurement of $\mathrm{SNR}_{\mathrm{low}}/\mathrm{SNR}_{\mathrm{high}}$ as an indicator for the GW "colour" with some confidence. Even at a distance of 20 kpc, the excess power in both the high- and low-frequency bands would still remain detectable and quantifiable in the SASI-dominated models. For the more modest goal of a mere detection, the SNR for model s20s would be high enough to observe events throughout the entire Milky Way and even out to the Large Magellanic Cloud ($\sim$50 kpc).

6.4.5. Interpretation of a prospective detection

Without a more sophisticated analysis of the time-frequency structure of a prospective detection event, only limited conclusions about the supernova core could be drawn from excess power measured by GW detectors during specific time windows. Nonetheless, a GW detection with the Einstein Telescope would be valuable for corroborating our understanding of hydrodynamic instabilities in the core in conjunction with the observed neutrino signal.

A high value of $\mathrm{SNR}_{\mathrm{low}}/\mathrm{SNR}_{\mathrm{high}}$ concurrent with a periodic modulation of the neutrino signal (Marek et al., 2009, Lund et al., 2010, Brandt et al., 2011, Tamborra et al., 2013, Müller & Janka, 2014, Tamborra et al., 2014a) would furnish solid evidence for SASI activity, and strong low-frequency emission concurrent with modulations of the neutrino signal below $\sim$50 Hz would strongly indicate that shock revival is already underway during the time window in question. While these conclusions could likely be drawn on the basis of the neutrino signal alone for nearby supernovae with a suitable orientation of the SASI spiral plane or sloshing mode, the detection of modulations in the neutrino signal for non-optimal orientations becomes difficult at distances $\gtrsim$ 10 kpc (Müller & Janka, 2014). In such cases, combining the GW and neutrino signal would likely allow stronger conclusions.

When SASI-induced modulations of the neutrino signal are not detectable due to distance, orientation, or unfavourable neutrino flavor oscillations, a detection of strong GW power in the low-frequency band would still provide evidence for *either* SASI activity (since this signal component is more robust against orientation effects than modulations of the neutrino signal) *or* the onset of strongly asymmetric accretion after shock revival. If the SNR is sufficiently high to localise the GW power excess in time relative to the onset of the neutrino signal (which roughly marks the time of bounce), it may be possible to decide between those two alternatives.

Late GW power excess after $\gtrsim$0.5 s will likely indicate the onset of the explosion without prior SASI activity, since the SASI typically reaches non-linear saturation well before this point, and since the decreasing mass in the gain region does not allow for strong late-time GW emission due to the SASI (as shown by models s20 and s27).

6.5. Conclusions

We have studied the GW signal from the accretion phase and the early explosion phase of core-collapse supernovae based on four recent 3D multi-group neutrino hydrodynamics simulations. We considered four models based on three progenitors with ZAMS masses of $11.2M_{\odot}$, $20M_{\odot}$, and $27M_{\odot}$. The three non-exploding models enabled us to study the phase between bounce and shock revival. We covered both the SASI-dominated regime (model s20, Tamborra et al., 2014a; model s27, Hanke et al., 2013), as well as the convection-dominated regime (model s11.2, Tamborra et al., 2014b). Additionally, the exploding $20M_{\odot}$ model s20s (Melson et al., 2015b,with a modified axial-vector coupling constant for neutral current scattering) illustrates changes in the GW signal in exploding models. Since our treatment of the microphysics and the neutrino transport is on par with previous works on the GW signal from 2D simulations (Marek et al., 2009, Yakunin et al., 2010, Müller et al., 2013, Yakunin et al., 2015), we were in the position to conduct a meaningful comparison of GW emission in 2D and 3D during the accretion and explosion phase for the first time. To this end, we included the $27M_{\odot}$ 2D models of Müller et al. (2012c) and Hanke et al. (2013) in our study.

Our analysis showed differences between the GW emission in 2D and 3D. The prominent, relatively narrow-banded emission at high-frequencies that is characteristic of 2D models is significantly reduced. With the reduction of the high-frequency emission, distinctive broadband *low-frequency* emission in the range between 100 Hz and 200 Hz emerges as a characteristic feature during episodes of SASI activity and during the explosion phase of model s20s. The low-frequency emission does also exist in the 2D models, but it is completely overwhelmed by the high-frequency emission. This conclusion is somewhat model dependent, because in one of our 2D models, s27-2D, high-frequency GW emission is low and the low-frequency component becomes very prominent.

We discussed these differences extensively from two vantage points: On the one hand, we investigated the underlying hydrodynamic processes responsible for GW emission and showed how the changes in the GW signal in 3D are related to critical differences in flow dynamics in 3D compared to 2D. On the other hand, we outlined the repercussions of these changes for future GW observations and sketched possible inferences that could be drawn from the detection of a Galactic event by third-generation instruments.

With regard to the hydrodynamic processes responsible for GW emission, our findings can be summarised as follows:

1. There is a high-frequency signal component that closely traces the buoyancy frequency in the PNS surface region in 2D and 3D, i.e. the roughly isothermal atmosphere layer between the PNS convection zone and the gain region acts as frequency stabiliser for forced oscillatory motions in both cases. However, the high-frequency component mostly stems from aspherical mass motions in and close to the overshooting region of PNS convection in 3D, whereas it stems from mass motion close to the

gain radius in 2D. This indicates that quasi-oscillatory mass motions at high frequencies are instigated *only by PNS convection in 3D* even during the pre-explosion phase, whereas forcing by the SASI and convection in the gain region is dominant in 2D. The resulting *amplitudes of the high-frequency component are considerably lower in 3D than in 2D.*

2. We ascribe the strong excitation of high-frequency surface g-mode oscillations in 2D to several causes: The inverse turbulent cascade in 2D leads to larger impact velocities of the downflows and creates large flow structures that can effectively excite $l = 2$ oscillations that give rise to GW emission. Braking of downflows by the forward turbulent cascade and fragmentation into smaller eddies strongly suppress surface g-mode excitation in 3D. Moreover, the spectrum of turbulent motions does not extend to high frequencies in 3D both in SASI-dominated and convection-dominated models so that the resonant excitation of the $l = 2$ surface g-mode at its eigenfrequency becomes ineffective.

3. In 3D, low-frequency GW emission in the pre-explosion phase ultimately stems from the global modulation of the accretion flow by the SASI. Because of frequency doubling and/or the contribution from the $l = 2$ mode, the typical frequencies of this component are of the order of $100 \ldots 200\,\mathrm{Hz}$, i.e. somewhat higher than the typical frequency of the $l = 1$ modes of the SASI. Mass motions in the post-shock region, the PNS surface region and the PNS convection zone all contribute to this low-frequency component, which indicates that the modulation of the accretion flow is still felt deep below the gain radius as the accreted matter settles down onto the PNS. Moreover, our analysis of the detection prospects shows that *the low-frequency component of the signal at* $\gtrsim 100\,\mathrm{Hz}$ *becomes a primary target in terms of detectability* in contrast to previous 2D results.

4. By contrast, convective models characterised by mass motions of intermediate- and small-scale like s11.2 show very little GW emission at low frequencies. The high-frequency emission, on the other hand, is excited primarily by PNS convection and is therefore less sensitive to the dominant instability (convection or SASI) in the post-shock region. *Thus, the ratio of high-frequency to low-frequency GW power can potentially be used to distinguish SASI- and convection-dominated models in the pre-explosion phase.*

5. However, strongly enhanced low-frequency emission can also occur due to a change of the preferred scale of the convective eddies in the PNS convection zone as exemplified by model s20s, where the dominant mode shifts from $l = 1$ to $l = 2$ late in the simulation. Since this does not occur in the corresponding non-exploding model s20, one can speculate that this behaviour is due to changes in the accretion flow and neutron star cooling associated with shock revival. If this behaviour is generic for exploding models enhanced GW emission may still remain a fingerprint of shock revival as it is in 2D (Murphy et al., 2009, Müller et al., 2013). With only one

explosion model available to us, this conclusion does not rest on safe ground; more 3D explosion models are needed to check whether enhanced low-frequency GW emission after shock revival is indeed a generic phenomenon.

It is obviously of interest whether future GW observations will be able to discriminate between models with such distinctively different behaviour as the ones presented here. Without an elaborate statistical analysis, only limited conclusions can be drawn concerning this point. In this paper, we confined ourselves to rough estimates based on the expected excess power in second- and third-generation GW detectors in two bands at low ($20 \ldots 250$ Hz) and high ($250 \ldots 1200$ Hz) frequency. Due to the reduction of the signal amplitudes compared to 3D, the prospects for second-generation detectors appear rather bleak; even the SASI-dominated models s20, s20s, and s27 could not be detected out further than $\sim$2 kpc with AdvLIGO at a confidence level of 95%. Third-generation instruments like the Einstein Telescope, however, could not only detect all of our models at the typical distance of a Galactic supernova ($\sim$10 kpc) and strong GW emitters like s20s out to 50 kpc; the expected signal-to-noise ratios could even be high enough to distinguish models with enhanced low-frequency emission due to SASI from convective models based on the "colour" of the GW spectrum. In conjunction with timing information and the neutrino signal, it may also be possible to distinguish enhanced low-frequency emission from the SASI from enhanced GW emission after shock revival as in model s20s.

However, more work is obviously needed to fully exploit the potential of GWs as a probe of the supernova engine in the case of "ordinary", slowly rotating supernovae for which PNS convection and the SASI are the dominant sources of GW emission. Desiderata for the future include a much broader range of 3D explosion models to determine to what extent the aforementioned features in the GW signal are generic. With waveforms from longer explosion simulations, the prospects for detecting a Galactic supernova in GWs with second generation instruments may also appear less bleak than they do now based on our biased selection that includes only one explosion model evolved to 200 ms after shock revival.

Furthermore, it is conceivable that much more information can be harvested from the GW signals than our simple analysis suggests. Several authors (Logue et al., 2012, Hayama et al., 2015, Gossan et al., 2016) have already demonstrated the usefulness of a powerful statistical machinery in assessing the detectability of supernovae in GWs and distinguishing different waveforms (e.g. from rotational collapse and hot-bubble convection, Logue et al., 2012). Peeling out the more subtle differences between SASI- and convection dominated models from GW signals in the face of greatly reduced signal amplitudes certainly presents a greater challenge, but third-generation instruments will nonetheless make it an effort worth undertaking.

The GW analysis presented in this work is based on three non-rotating progenitors, and it remains to be seen whether the findings from these simulations are generic. For GW detection, it is particularly important to ascertain whether the overall reduction of the signal from SASI and convection in 3D compared to 2D is always as strong as in our models, where the difference is a factor of ~10. This has recently been questioned by Yakunin et al. (2017), who reported considerably higher amplitudes for a $15M_{\odot}$ progenitor than in our models and found the energy emitted in GW to be similar in their 2D and 3D simulations. Considering that we obtain weaker GW signals in 3D in models that probe a variety of different regimes, and that other 3D studies (Müller et al., 2012a, Kuroda et al., 2016) predict amplitudes in line with our findings (albeit with less rigorous neutrino transport and without a 2D/3D comparison) suggests that small amplitudes $|A| \lesssim 5\,\mathrm{cm}$ are generic in 3D and that the strong amplitudes in Yakunin et al. (2017) are the exception rather than the norm and need further explanation. Nonetheless, the range of variation in GW amplitude in 3D deserves to be explored further in the future.

There are various properties of the pre-collapse cores that will (or at least could) impact the GW signal. The influence of rotation is well known: In rapidly rotating models there is a strong GW burst associated with the rebound of the core (Müller, 1982). During the post-bounce phase rotation can lead to a bar-like deformation of the core (Rampp et al., 1998, Shibata & Sekiguchi, 2005) or the development of low-mode spiral instabilities (Ott et al., 2005, Kuroda et al., 2014, Takiwaki et al., 2016). These flow patterns in turn lead to strong GW emission at frequencies determined by the rotational frequency. In addition, rotation can modulate processes already present in nonrotating models, for example prompt convection or the SASI. In the models presented by Dimmelmeier et al. (2008) and Ott et al. (2012) only models with moderate rotation rates (and nonrotating models) exhibit prompt convection. The coupling between rotation and SASI activity can lead to an enhanced growth rate of the spiral SASI mode (Blondin & Mezzacappa, 2007, Yamasaki & Foglizzo, 2008, Iwakami et al., 2009, Kazeroni et al., 2016, Janka et al., 2016). Whether a significant proportion of supernova progenitors have moderately rotating (let alone rapidly rotating) cores is unclear. Stellar evolution models that include the effects of magnetic fields predict rather slowly rotating pre-collapse cores (Heger et al., 2005). Furthermore, the angular momentum loss due to stellar winds seems to be underestimated by stellar evolution models, compared to results from asteroseismology (Cantiello et al., 2014). Predictions of the initial rotation rate of pulsars, based on their current spin-down rate and age, suggest that a large fraction of the pulsar population is born with rotation periods of the order of tens to hundreds of milliseconds (Popov & Turolla, 2012, Noutsos et al., 2013).

There is also the issue of starting the simulations from spherically symmetric progenitor models. Current GW predictions like ours rely on explicitly imposed (this study) or numerical seed perturbations to trigger the development of non-radial instabilities, and it needs to be explored further whether the level of seed perturbations is partly responsible for differences in the GW amplitudes calculated by different groups (e.g. this study and Yakunin et al. 2017). Moreover, it has been found that physical seed asymmetries in the burning shells of the progenitor can influence the shock dynamics and even help to ensure a successful explosion (Burrows & Hayes, 1996, Fryer et al., 2004, Arnett & Meakin, 2011, Couch & Ott, 2013, Müller & Janka, 2015). Any change in the initial conditions that leads to a significant change in the dynamics of the supernova core should be expected to impact the GW signal. Therefore, it will be important to keep improving the predicted GW signals, in hand with the improvement of core collapse models.

7. The effects of rotation

In the previous chapter we studied four non-rotating models of core-collapse supernovae, focusing on the underlying hydrodynamic instabilities responsible for GW emission and how these excitation mechanisms change when taking the step from 2D to 3D. With this knowledge in hand, we will now discuss the effects of rotation. In this chapter we present the GW signals from three core-collapse simulations of a 15 $M_{\odot}$progenitor (Heger et al., 2005). Of the three simulations, two of the models include rotation and in the third model rotation has been set to zero. This allows us allows us to study how the GW signal changes, for the same stellar progenitor, with rotation. Two of the three models (the fastest rotating model and the model without rotation) are dominated by strong SASI activity, while the slowest rotating model only develops weak and intermittent SASI oscillations. We can, therefore, study the influence of rotation in both the SASI dominated regime and the convective regime. The model with the strongest rotation successfully explodes and we can, therefore, also study the impact of rotation in the time after shock revival.

The study of GWs generated by the core-collapse of rotating stars has a long and rich history. The first efforts consisted of idealised calculations, such as the rotating ellipsoidal models of Thuan & Ostriker (1974), Novikov (1976), Shapiro (1977), Saenz & Shapiro (1978; 1979), and Saenz & Shapiro (1981). During the last four decades, starting in the early 80s with Müller (1982), the theoretical GW signals from multi-dimensional simulations, with ever increasing sophistication, have been extensively studied (Müller, 1982, Finn & Evans, 1990, Mönchmeyer et al., 1991, Yamada & Sato, 1995, Zwerger & Müller, 1997, Rampp et al., 1998, Dimmelmeier et al., 2001, Dimmelmeier, 2001, Dimmelmeier et al., 2002b, Kotake et al., 2003, Ott et al., 2004, Yamada & Sawai, 2004, Shibata & Sekiguchi, 2004, Cerdá-Durán et al., 2005, Saijo, 2005, Ott et al., 2005, Shibata & Sekiguchi, 2005, Kotake et al., 2006, Obergaulinger et al., 2006, Ott, 2007, Dimmelmeier et al., 2007a;b; 2008, Reisswig et al., 2011, Takiwaki & Kotake, 2011, Ott et al., 2012, Kuroda et al., 2014, Fuller et al., 2015).

Rapidly rotating models are expected to have a strong GW burst associated with core bounce, see Müller (1982) or Kuroda et al. (2014), and Fuller et al. (2015) for more recent results from 3D simulations. During the time between core bounce and shock revival, very rapid rotation can cause the inner core to deform in a bar-like manner (Rampp et al., 1998, Shibata & Sekiguchi, 2005). In slower, but still fast, rotating models, a low-mode spiral instability has been found to develop (Ott et al., 2005, Kuroda et al., 2014, Takiwaki et al., 2016). These instabilities leads to strong GW emission that results in optimistic predictions of detection prospects. The three models studied here are to slowly rotating to develop such instabilities and we will show that slow and moderate rotating progenitor do not yield the same result and that detection with current GW detectors will be difficult, even for a galactic event.

While slowly rotating models have not been well studied in 3D, there are several indications that the rotation rate of core-collapse progenitors should be slow/moderate rather than rapid (Heger et al., 2005, Beck et al., 2012, Mosser et al., 2012, Popov & Turolla, 2012, Noutsos et al., 2013, Cantiello et al., 2014, Deheuvels et al., 2014). But, even slow rotation can help facilitate the success of core-collapse simulations. The critical neutrino luminosity required to relaunch the stalled shock decreases when specific angular momentum is injected into the post-shock layer (Iwakami et al., 2014, Nakamura et al., 2014). We find that, for the rotation rates studied here, there is no significant change of the GW signal, compared to non-rotating models. While there are significant changes to the dynamics and the underlying excitation processes of the GWs, the signals from our rotating models are not qualitatively distinguishable from the non-rotating models studied in this thesis.

This chapter is structured as follows: First, we present the numerical models and describe their dynamics, we then give a description of the GW signals. In section 7.3 we describe the underlying hydrodynamic effects responsible for GW excitation and discuss how they, and consequently the GW signals, are affected by rotation. Before we discuss our results and present our conclusions, and we will assess the detection prospects of the three models and what the effects of progenitor rotation are in this regard.

7.1. Supernova Models

We present the GW signal from three models based on the progenitor of Heger et al. (2005), which is a solar-metallicity star with a ZAMS mass of $15 M_{\odot}$. The stellar evolution calculation accounted for the effects of magnetic fields and rotation and evolved the model from ZAMS to the onset of iron-core-collapse. The inclusion of magnetic fields leads to an overall reduction of the final rotation rate of the iron core, compared to calculations without magnetic fields (Heger et al., 2005). The main difference between the three models is their rotation profiles. One of the models uses the rotation profile of the progenitor (m15r), one has an enhanced rotation rate (m15fr), and in the last model the rotation rate has been set to zero throughout the star (m15nr) In Fig. 7.1 we show the rotation profiles of models m15fr, and m15fr.

- **m15fr:** The initial rotation profile of model m15fr was, by hand, set to a constant rotation rate of 0.5 rad/s throughout the inner 1731 km of the core. Beyond a radius of 1731 km the rotation rate declines linearly (Fig. 7.1). The model was simulated using the Yin-Yang grid, the two grid patches had an initial resolution of 400 cells, 56 cells, and 144 cells in the radial, polar, and azimuthal direction, respectively.

This corresponds to a 2 degree angular resolution. After the initial shock expansion halts around 60 ms post bounce the average shock radius decreases slightly. Between $\sim 80 - 160$ ms post bounce the shock front is more or less stationary. The shock starts to expand roughly 160 ms after core bounce and soon after shock revival sets in. In the time before shock revival, the post-shock flow is dominated by a strong spiral SASI mode. The SASI sets in at around ~ 100 ms post bounce. In we show volume renderings of the entropy per nucleon Fig. 7.4, which gives an impression of the flow patterns of this model.

- **m15r:** The initial rotation profile of model m15r was exactly that of the progenitor (Heger et al., 2005). The rotation profile as a function of radius can be seen in Fig. 7.1. The model was simulated using the Yin-Yang grid, the two grid patches had an initial resolution of 400 cells, 56 cells, and 144 cells in the radial, polar, and azimuthal direction, respectively. This corresponds to a 2 degree angular resolution. For the first ~ 80 ms after bounce, the evolution of the average shock radius of model m15r closely resembles that of model m15fr. However, around 100 ms after bounce the average shock radius starts to decrease. Unlike model m15fr, strong SASI activity does not develop in this model. The flow in the post-shock region is instead dominated by hot-bubble convection (see Fig. 7.5). There is, however, some low amplitude dipole deformation of the shock front (see Fig. 7.3). The average shock radius continues to decrease until ~ 200 ms post bounce when the Si-O shell interface falls through the shock. The decreased density in front of the shock reduces the ram pressure and a transient period of shock expansion occours. At ~ 240 ms post bounce the expansion subsides and the shock front once more begins to retreat, a trend which continues until the end of the simulation.

- **m15nr:** In model m15nr the initial rotation rate was set to zero at all radii. The model was simulated using the Yin-Yang grid, the two grid patches had an initial resolution of 400 cells, 28 cells, and 72 cells in the radial, polar, and azimuthal direction, respectively. Which means that model m15nr was simulated with an angular resolution that is two times coarser than the other two models (4 degrees). Initially, the shock expands and reaches a local maximum around 60 ms after bounce, from this point on the shock radius steadily decreases until the Si-O shell interface falls through the shock. The decreased accretion rate leads to a transient period of shock expansion until the shock eventually starts to recede once more. Except for the fact that the average shock radius is generally larger in model m15nr, model m15nr is similar to model m15r in terms of the evolution of the average shock radius. However, unlike model m15r, model m15nr develops strong SASI activity. In this model, the SASI activity is dominated by the sloshing mode, which develops around ~ 120 ms after core bounce and peaks around ~ 230 ms post bounce. After the peak in activity the SASI mode gradually decays towards the end of the simulation.

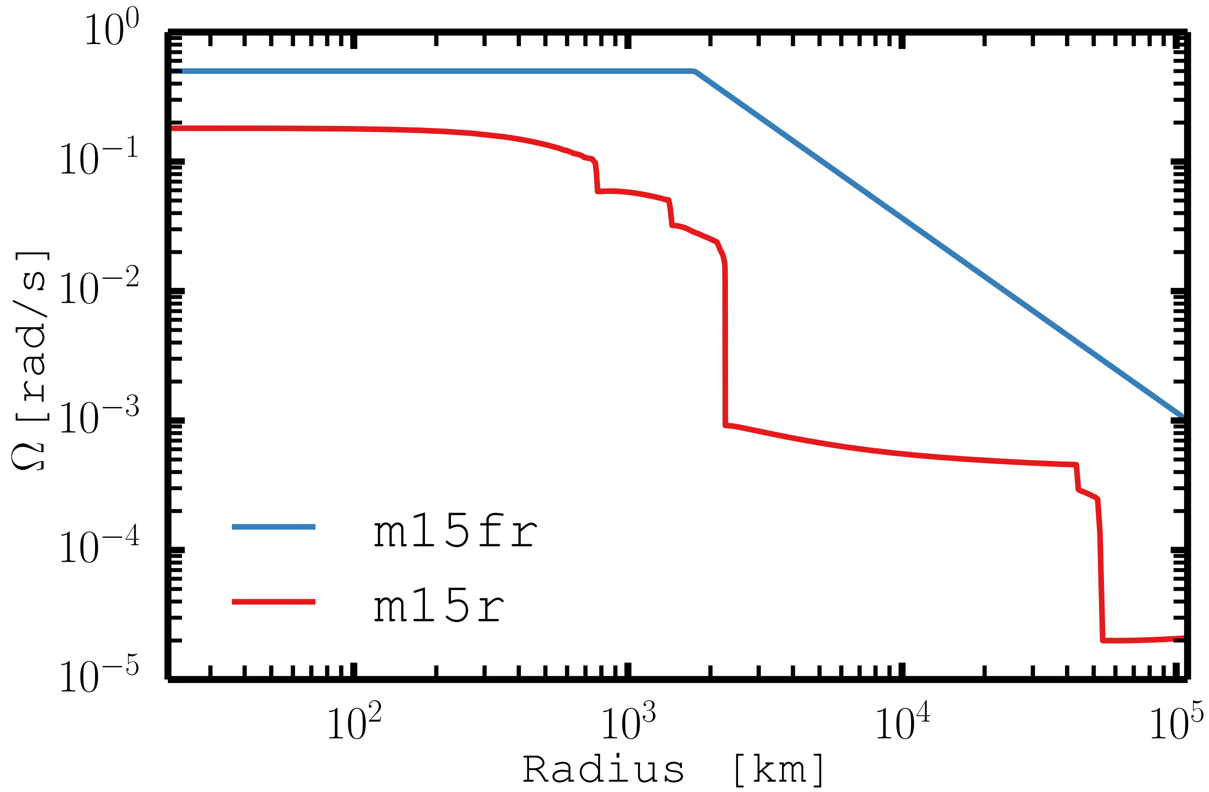

Figure 7.1.: The radial rotation profiles (in the equatorial plane) for the two rotating models. The blue line represents model m15fr and the red line represents m15r.

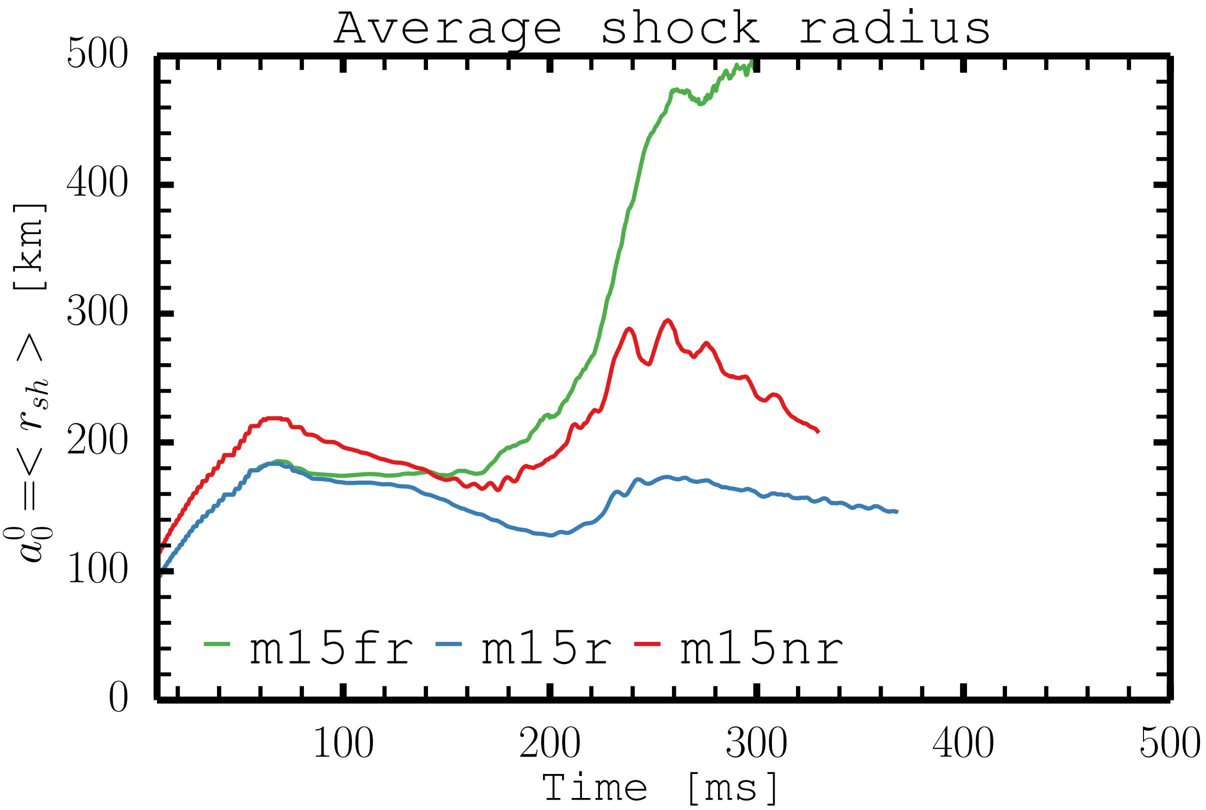

Figure 7.2.: Average shock radius for models m15fr (green), m15r (blue), and m15nr (red) as a function of time after core bounce. The average shock radius is defined as the $(l, m) = (0, 0)$ expansion coefficient of the shock surface into spherical harmonics (Eq. 6.10).

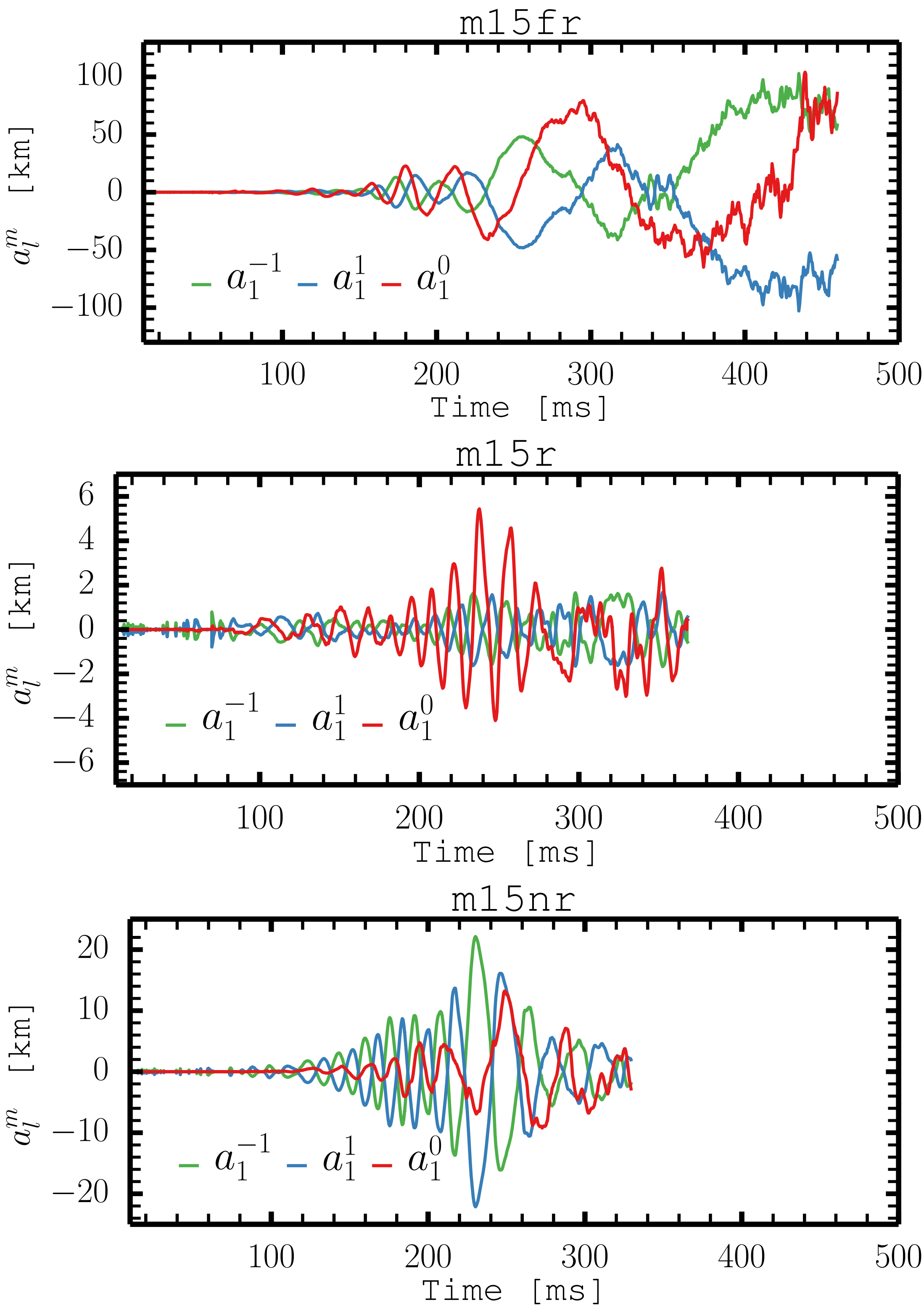

Figure 7.3.: The $(l, m) = (1, 0)$, $(1, 1)$, and $(1, -1)$ coefficients of the decomposition of the shock surface into spherical harmonics as a function of time after bounce (see Eq. 6.10). From top to bottom: Model m15fr, model m15r, and model m15nr.

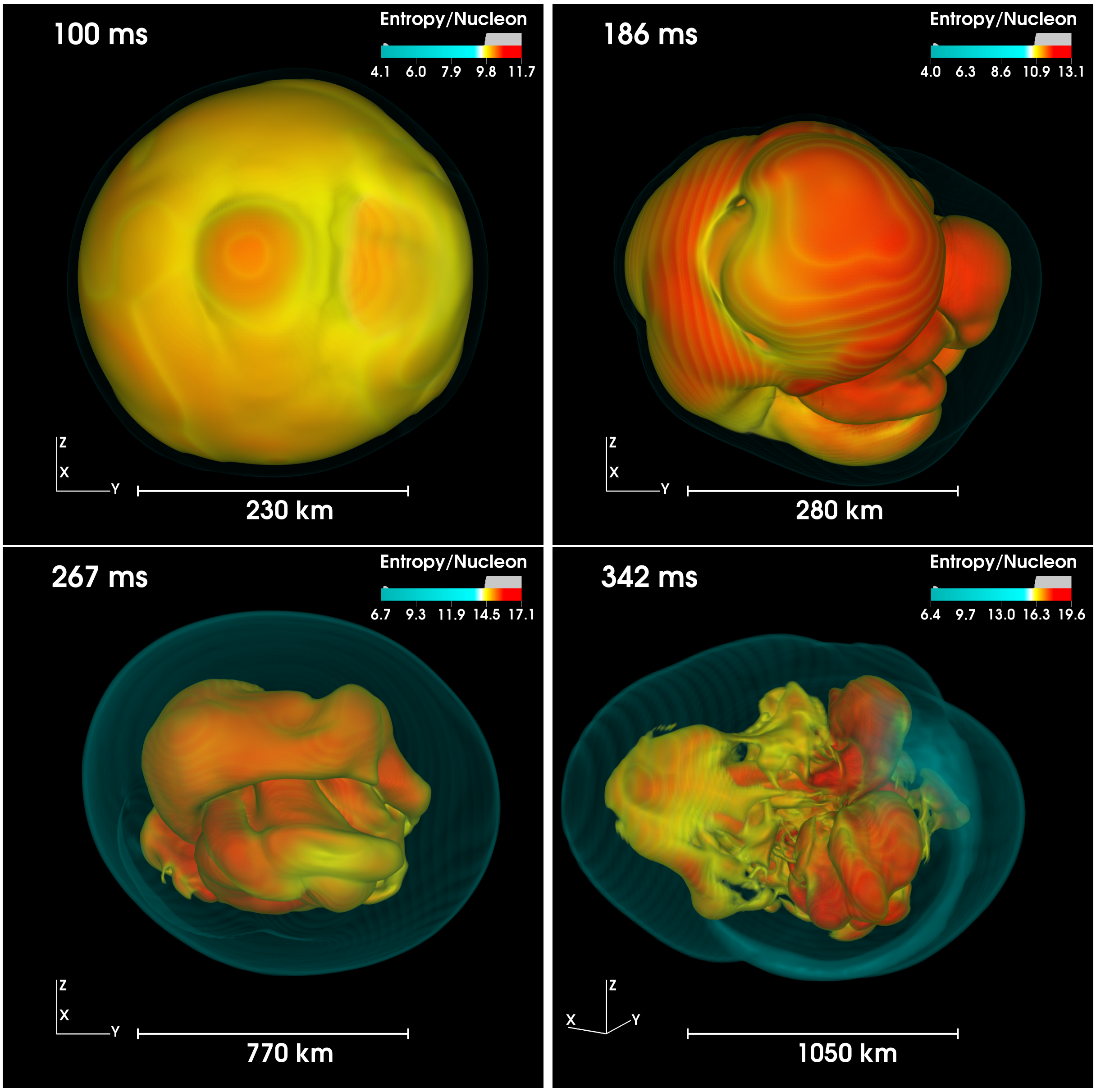

Figure 7.4.: Volume rendering of the entropy per nucleon for model m15fr. The four panels show four different times, the time after core bounce is indicated in the upper left corner of each panel. The blue surface shows the shock front. The deformation of the shock front that is indicative of SASI activity can be seen in the top right panel. In the two bottom panels we see that the average shock radius has reached large values and that runaway shock expansion is underway.

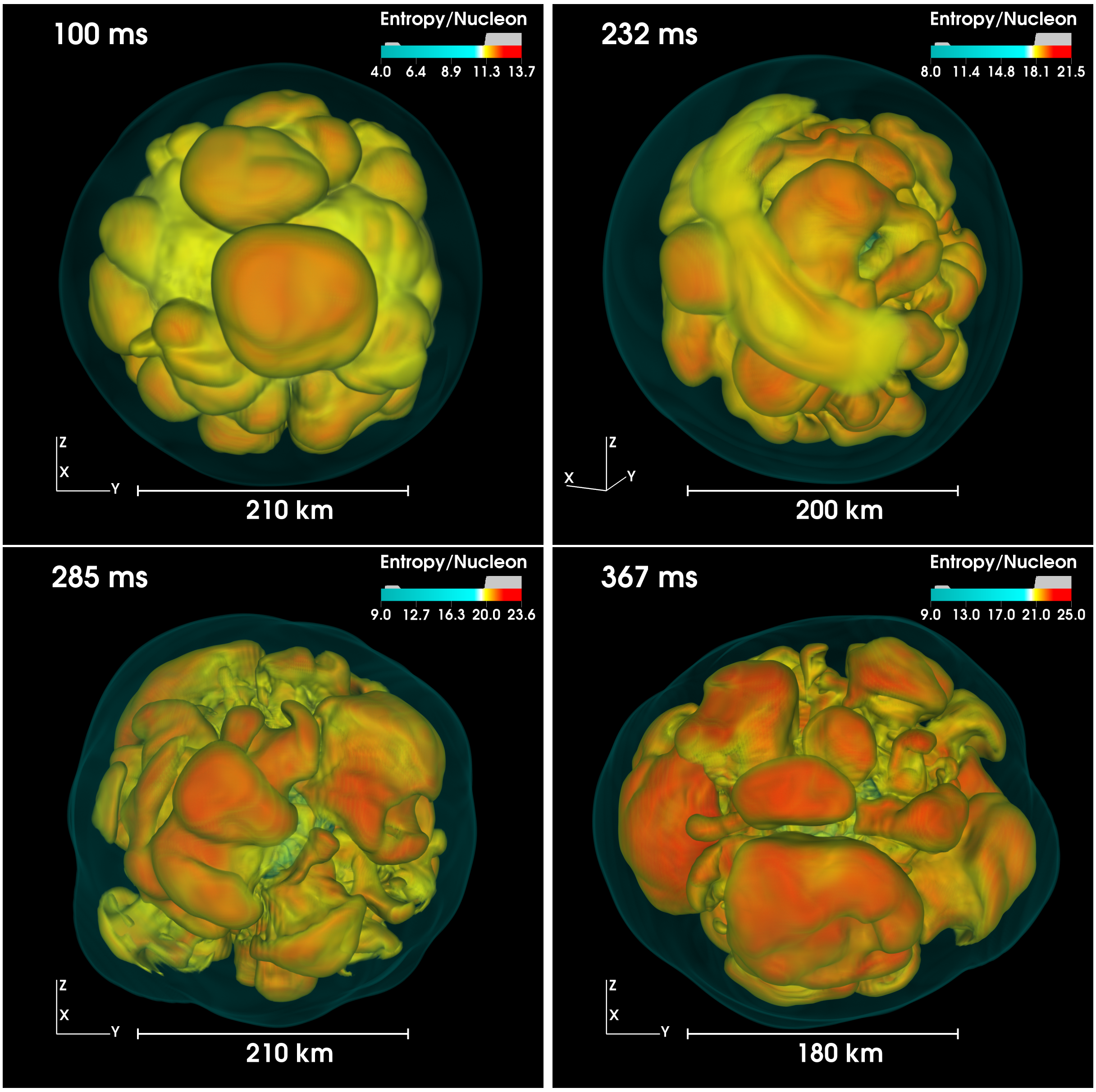

Figure 7.5.: Volume rendering of the entropy per nucleon for model m15r. The four panels show four different times, the time after core bounce is indicated in the upper left corner of each panel. The blue surface shows the shock front. In all panels we see that the flow in the region between the shock and the PNS is dominated by neutrino-driven convection, the typical mushroom shaped convective bubbles are clearly visible. However, in the top right panel we see that the convective activity is severely reduced. The yellow arc seen in the middle of the top right panel is a sign of weak SASI activity, which intermittently develops in model m15r.

7.2. Results

7.2.1. Qualitative description of the gravitational wave signals

The GW signals from the rotating models do not qualitatively differ from the signals presented in chapter 6. It is expected that GWs will be emitted during the collapse, and recoil of a rotating core. However, since the 3D simulations do not cover this phase, the GW signal produced during this phase will not be present in the waveforms from the 3D simulations. From the onset of core-collapse until around 10 ms after core bounce the models were evolved in 2D. Towards the end of this chapter we will discuss the bounce signal from the 2D simulations, but for now we will focus on the post-bounce phase.

In Fig. 7.6 we show the GW amplitudes generated by asymmetric mass motions for models m15fr, m15r, and m15nr. The two columns show the amplitudes for two different observer orientations, the right and left column represent observers situated along the x-axis (equator) and the z-axis (pole) of the Yin grid-patch, respectively. The rows are ordered by progenitor, in order of decreasing initial rotation rate, and from the top show models m15fr, m1fr, and m15nr. Vertical lines indicate episodes of strong SASI activity. The corresponding amplitude spectrograms (see Eq. 5.7) for a sliding window of 50 ms width are shown in Fig. 7.7. The spectrograms show the sum of the squared Fourier components of the cross and plus polarisation modes, $|\mathrm{STFT}[A_+]|^2 + |\mathrm{STFT}[A_\times]|^2$. Before applying the DFT we convolve the signal with a Kaiser window with shape parameter $\beta = 2.5$. Frequencies below 50 Hz and above 1100 Hz are filtered out of the resulting spectrograms.

In all three models, an initial phase of quiescence is followed by a phase of stochastic emission, during which the typical amplitudes are of the order of a few cm. The fastest rotating model, model m15fr, emits the strongest GW signal. At the same time the non-rotating model (m15nr) shows larger amplitudes than the moderately rotating model (m15r). There seems to be no clear correlation between the strength of the initial rotation rate and the strength of the GW emission. The spectrograms (Fig. 7.7) of the three models show the familiar low-frequency and high-frequency components that we also saw in the four models presented in chapter 6.

m15fr During the SASI phase of m15fr, we see a low-frequency signal component in addition to the high-frequency stochastic component. Both strong low-frequency and high-frequency emission are visible in the upper row of Fig. 7.7. The two signal components cover a broader frequency range in model m15fr than in the other two models, to the point where the two components almost overlap. After the shock starts to expand the overall GW amplitudes are strongly reduced, but both low-frequency and high-frequency emission continues until the end of the simulation.

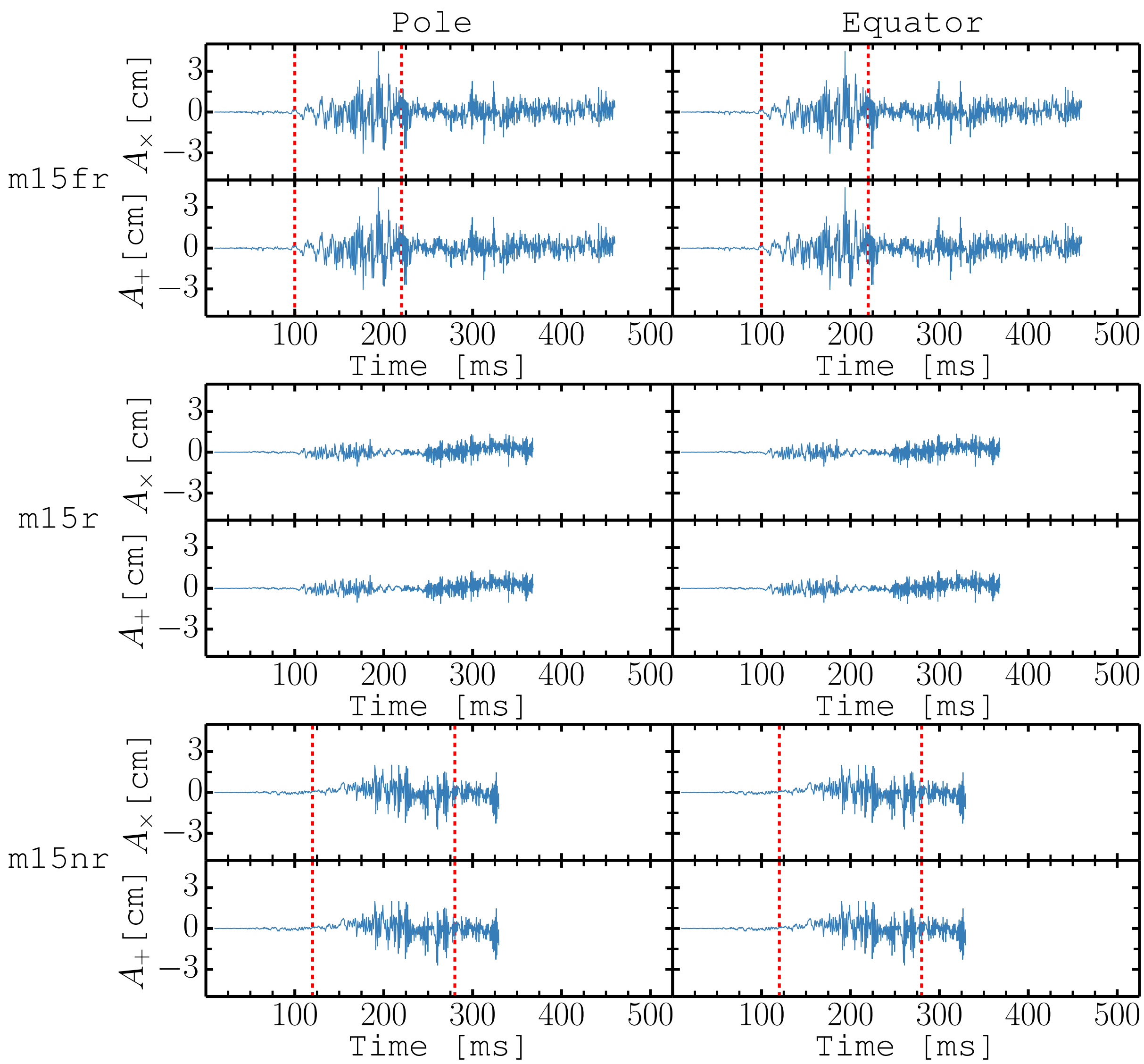

Figure 7.6.: GW amplitudes A_+ and $A_\times$ as functions of time after core bounce. For models m15fr, m15r, and m15nr, from top to bottom. The two columns show the amplitudes for two different viewing angles: an observer situated along the z-axis (pole; left) and an observer situated along the x-axis (equator; right) of the Yin grid patch, respectively. Episodes of strong SASI activity occur between the vertical red dotted lines.

m15r Of the three models, model m15r produces the weakest GW signal. The GW amplitudes never exceed a value of 1.5 cm. Furthermore, the signal is strongly reduced in the time period between 180 and 250 ms post bounce. During this time high-frequency emission completely subsides and only very weak low-frequency emission is present in the signal. Around $\sim$ 250 ms post bounce high-frequency emission sets in once more, at the same time the low-frequency emission ceases.

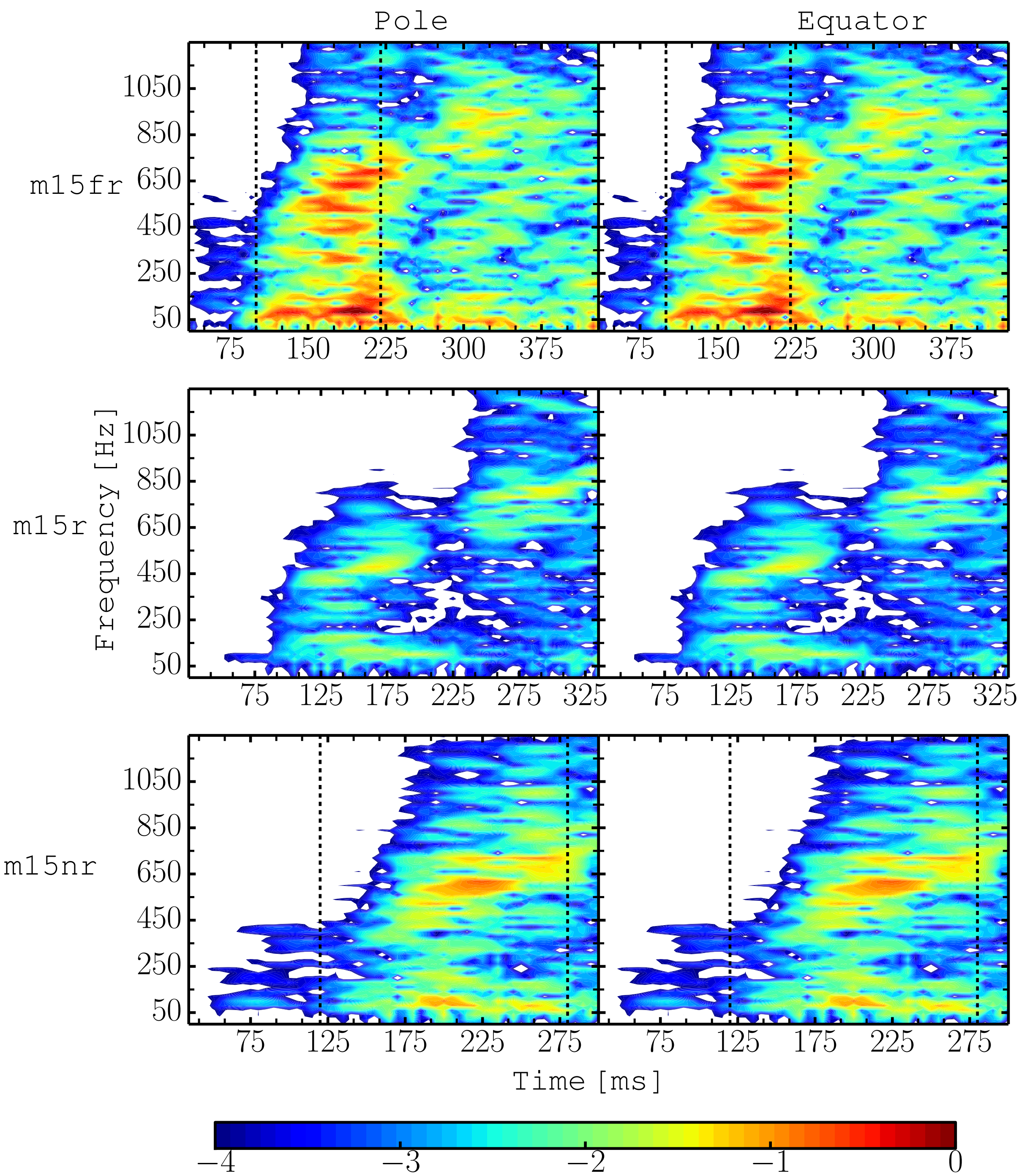

Figure 7.7.: Amplitude spectrograms for a sliding window of 50 ms and two different observer directions, summed over the two polarisation modes ($|\mathrm{STFT}[A_+]|^2 + |\mathrm{STFT}[A_\times]|^2$). The different rows show the results for models m15fr, m1fr, and m15nr. (top to bottom). The two columns shows the spectrograms for two different viewing angles, the right and left column represent observers situated along the z-axis (pole) and x-axis (equator) of the Yin grid, respectively. The time is given in ms after core bounce. Vertical lines bracket SASI episodes. All panels have been normalised by the same global factor. The colour bar is given in a logarithmic scale.

m15nr The non-rotating model is characterised by a relatively long initial quiescent phase, compared to the two rotating models. Low amplitude low-frequency GW emission sets in around ~ 125 ms after bounce. The low-frequency signal component increases in strength until reaching a maximum around 175 ms after core bounce. Approximately 25 ms after the onset of low-frequency emission, high-frequency emission develops around ~ 150 ms after core bounce. The two signal components remain present in the signal, varying in strength, until the end of the simulation.

Time-integrated energy spectra

Time-integrated energy spectra for each of the models are shown in Fig. 7.8. These are computed from the Cartesian components of the mass quadrupole tensor, according to Eq. 2.42. The time-integrated energy spectrum of model m15fr is rather flat, with strong emission over a wide range of frequencies. There is a local peak in the spectrum around $\sim 75 - 100$ Hz. The slower rotating model m15r, which does not develop strong SASI oscillations, emits much less energy at low frequencies. However, this model also exhibits a peak in the energy spectrum at frequencies similar to $\sim 75 - 100$ Hz, but this peak is much weaker than the for in model m15fr. The energy spectrum of model m15nr is a hybrid between the spectrum of the two previous models. As for model m15fr, there is a significant amount of energy radiated away by GWs below 300 Hz, but the spectrum is not as flat as the one of model m15fr.

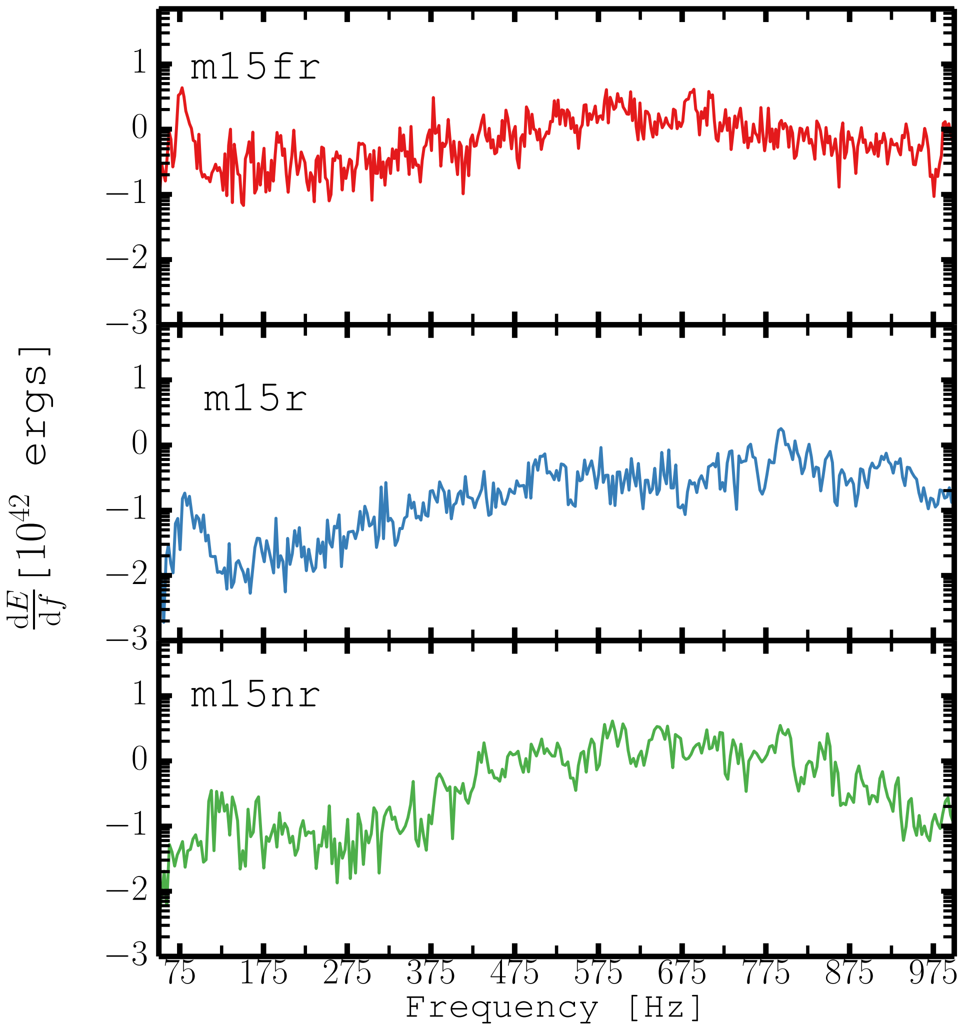

Figure 7.8.: Time-integrated GW energy spectra dE/df for models m15fr, m15r, and m15nr (top to bottom). The spectra are computed from the Fourier transform of the entire waveform without applying a window function.

7.3. Excitation of gravitational waves

In chapter 6 we studied the hydrodynamic instabilities responsible for GW emission. We found that GWs are mainly excited in four ways. SASI activity leads to a large-scale asymmetric mass distribution in the post-shock layer that directly leads to strong GW emission. In addition, the high-velocity violent downflows resulting from SASI activity perturb the PNS surface and excite non-resonant g-modes in the PNS, which in turn lead to strong GW emission. The frequency of the forced g-modes is set by the typical time scale of the SASI oscillations. High-frequency emission is caused by the propagation of resonant g-modes in the outer layers of the PNS. The typical frequency of these oscillations is given by the Brunt-Väisälä-frequency in the PNS surface. Resonant g-modes are excited in two ways. Firstly, by downdrafts from the post-shock layer impinge onto the PNS surface. Strong downflows can be created by SASI activity and overturn of convective plumes. Resonant g-modes are also excited, in the PNS surface layer, as plumes from the unstable layer beneath overshoot into the surface layer. For the four models presented in chapter 6, we found that PNS convection was the main driver of this process, while downflows from the post-shock layer provided a secondary and smaller contribution (with model dependent variations in the relative importance of the two).

These conclusions hold true for the three models presented in this chapter as well, with one notable exception. In the two rotating models, model m15fr and model m15r, the GW signal generated by PNS convection is significantly reduced. When rotation is added to the simulations a positive angular momentum gradient develops in the PNS convection layer, which acts as a stabiliser and weakens PNS convection (Janka et al., 2001). The basic physical picture is that when a buoyant plume propagates outwards its rotation rate is less than that of the surrounding medium and it experiences a weaker centrifugal force. The effect of rotation is, therefore, to exert a force acting against the outwards propagation of the plume. Angular momentum transfer by convection will eventually flatten the rotation profile within the PNS and the stabilising effect provided by rotation will gradually decrease with time.

Based solely on the stabilising effects rotation has on PNS convection we would expect an overall reduction of high-frequency GW emission in the two rotating models and that the fastest rotating model emits the weakest high-frequency signal. However, the picture is not so simple. We also have to consider the effects of the spiral SASI mode. The strong influence exerted by the spiral mode on the PNS, through a coherent large-scale modulation of the accretion flow onto the PNS, not only effectively perturbs the surface, but can also reach into the interior of the PNS and influence the convective layer of the PNS. A strong spiral SASI mode induces mass motions in the PNS at different frequencies, which is reflected in the GW signal as a “broadening” of both the low-frequency and high-frequency emission component. This happens because, as mentioned in the paragraph above, the strong downflows created by the SASI does not only excite resonant g-modes, but also force non-resonant oscillations. Model s27, which is dominated by the sloshing mode of the SASI, has a cleaner emission spectrum than for example model s20 dominated by the spiral SASI mode (see Fig. 6.3). Cleaner, here means that the emission is concentrated in narrow bands. The same behavior is seen in model m15fr and model m15r. A particular strong spiral SASI mode develops in m15fr and this model emits GWs over a wider range of frequencies than models m15nr, and m15r. The reduction of high-frequency GW emission generated by PNS convection can most clearly be seen in model m15r. Between 180 and 250 ms post bounce hot-bubble convection subsides. During this time model m15r emits virtually no high-frequency GWs. The average shock radius reaches a minimum around 200 ms post bounce, after a 70 ms long period of recession (Fig. 7.2). The small average shock radius favours SASI activity over neutrino-driven convection, and we see the development of low amplitude shock oscillations (see the middle panel of Fig. 7.3). Convection, on the other

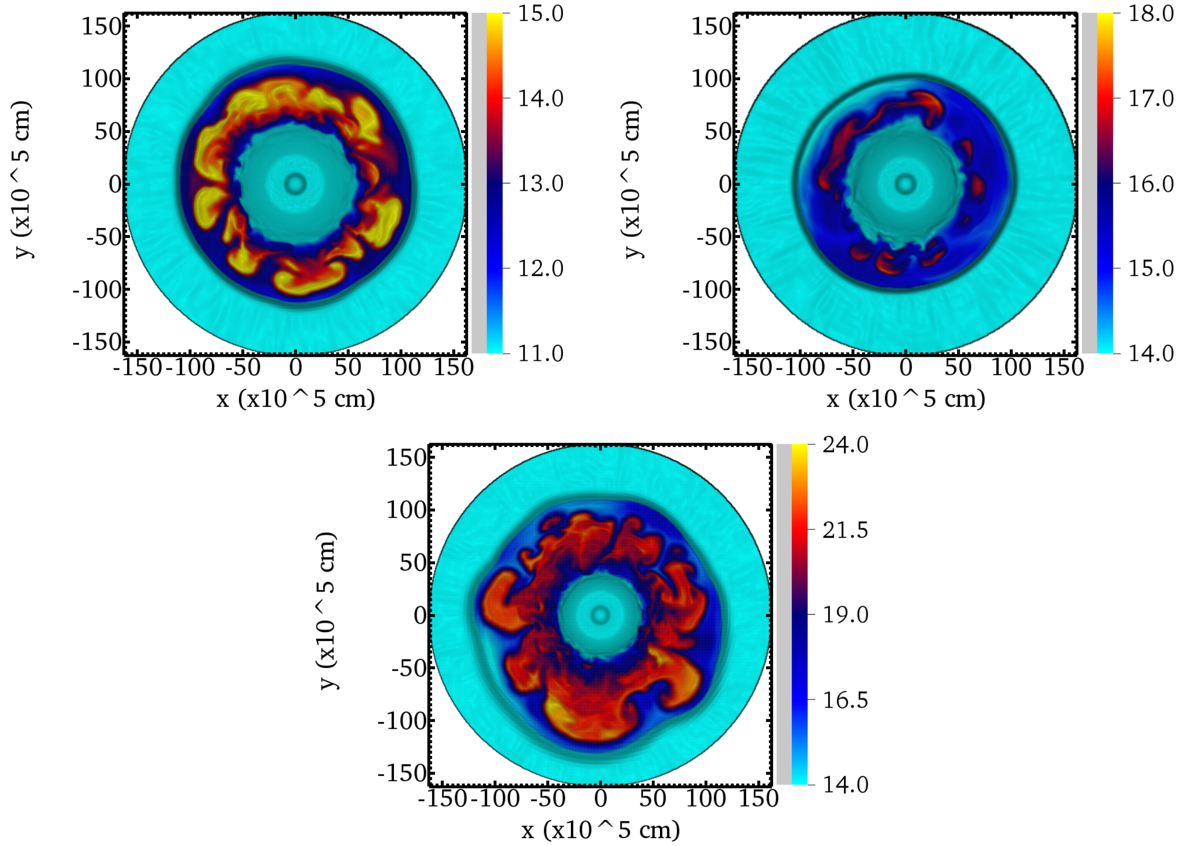

Figure 7.9.: The entropy per baryon in the xy-plane of the Yin-grid for model m15r. Shown at at 167 (top left panel), 210 (top right panel), and 343 (bottom panel) ms post bounce. The entropy is given in units of Boltzmann's constant k_b.

hand, is quenched. Fig. 7.9 shows the entropy per baryon of model m15r in the xy-plane of the Yin-grid. The three panels show snapshots taken 167 ms (top left panel), 210 ms (top right panel), and 343 ms (bottom panel) after core bounce. The top left and the bottom panels show the typical hot bubbles that are characteristic of neutrino-driven convection, but in the top right panel no such bubbles can be seen (the same behaviour can be seen in Fig. 7.5). The growth of low amplitude SASI activity and the suppression of convection in the post-shock layer is reflected in the GW signal as weak emission at low frequencies and a complete absence of the high-frequency signal component. This, naturally, means that high-frequency emission is for the most part caused by convective plumes from the post-shock layer impinging on the PNS surface.

The reduction of GWs emitted from the PNS can also be seen in model m15fr. After the onset of shock revival the accretion rate onto the central object decreases and the violent downflows created by strong SASI activity cease to exist. At the same time there is a strong reduction in the GW signal. This indicates that excitation of surface g-modes from above is the main source of high-frequency GW emission. This is in strong contrast to model s20s, where activity within the PNS increased after the onset of shock revival and consequently led to a strong increase of the GW signal amplitude. Thus the nature of PNS convection is an important factor in determining the GW signal from core-collapse supernovae.

7.4. The standing accretion shock instability, rotation, and resolution

In the models we discuss in this chapter, there is no clear connection between the development of SASI activity and the initial rotation rate of the progenitor. Model m15r, in which the rotation profile is in accord with stellar evolution calculations, does not develop strong SASI activity. In both model m15nr and model m15fr, however, a strong spiral SASI mode emerges.

Exactly how rotation influences the SASI growth rate and saturation does not seem to be a simple function of progenitor rotation rate. Recently Blondin et al. (2017) studied the effects of rotation by means of idealised hydrodynamic simulations of a standing accretion shock (in 2D and 3D). The results of Blondin et al. (2017) are in good agreement with the perturbative study of Yamasaki & Foglizzo (2008), who found that the linear growth rate of non-axisymmetric SASI modes is an increasing function of the progenitor rotation rate. However, in the non-linear regime Kazeroni et al. (2017) does not find a monotonic connection between the rotation rate and the saturation amplitude of the SASI. In fact, Fig.3 of Kazeroni et al. (2017) indicates that SASI activity may decrease with increasing rotation rate, at least at low to moderate rotation rates.

An additional complication comes from the fact that model m15nr was simulated with half the angular resolution of the other two models. The lower resolution has been found to favour the growth SASI activity, because energy accumulates at larger scales (Hanke et al., 2012). However, Abdikamalov et al. (2015) finds the opposite, and they conclude that increasing the angular resolution reduces SASI oscillations. They performed a set of general relativistic 3D hydrodynamic simulations of a 27 $M_{\odot}$progenitor with a neutrino leakage scheme to study the phase between bounce and shock revival.

Independent of whether rotation suppresses the growth of SASI activity in model m15r or SASI activity develops artificially in model m15nr because of insufficient angular resolution, the absence of strong SASI activity in model m15r reduces the overall strength of the GW signal.

Table 7.1.: Signal-to-noise ratio for models m15fr, m15r, and m15nr. Values are given for three different frequency domains, 20 . . . 250 Hz (low-frequency), 250 . . . 1200 Hz (high-frequency), and for the total frequency domain, 20 . . . 1200. The table shows values for two different detectors, AdvLIGO and the Einstein Telescope. For the latter, we calculate the SNR for two different modes of operation (ET-B and ET-C). The table shows SNRs for a source at a distance of 10 kpc. The three tables show SNRs for model m15fr, model m15r, and model m15nr (from top to bottom).

m15fr	Low	High	Total	Low/High
AdVLIGO	10.8	4.9	11.9	2.20
ET-C	133.2	67.6	149.4	1.97
ET-B	224.6	83.5	239.6	2.69

m15r	Low	High	Total	Low/High
AdVLIGO	2.6	2.4	3.5	1.08
ET-C	32.2	34.4	47.1	0.93
ET-B	53.7	41.1	67.7	1.30

m15nr	Low	High	Total	Low/High
AdVLIGO	3.5	4.3	5.5	0.81
ET-C	46.5	59.3	75.2	0.78
ET-B	74.0	72.0	103.2	1.02

7.5. Detection prospects

Following the procedure laid out in section 6.4, we calculate the possibility of detecting the GW signals from models m15fr, m15r, and m15nr. In order evaluate the possibility of differentiating between models with and without strong SASI activity (strong low-frequency emission) based on a detection of their GW signals, we compute SNRs in three frequency bands. The three bands are: the low-frequency band ($f \in [20, 250)$, $\delta f = 230$), the high-frequency band ($f \in [250, 1200)$, $\delta f = 950$), and the total frequency range ($f \in [20, 1200)$, $\delta f = 1180$). For the three bands we find, by inserting δf to Eq. 6.19 and assuming a signal length $\Delta t \sim 0.5$, detection thresholds of $\mathrm{SNR}_{\mathrm{low}} \gtrsim 11$, $\mathrm{SNR}_{\mathrm{high}} \gtrsim 15$, and $\mathrm{SNR}_{\mathrm{total}} \gtrsim 20$ for the low-frequency band, the high-frequency band, and "whole-frequency" band, respectively. As in chapter 6, we calculate the SNR from Eq. (6.13) for the zero-detuning-high power configuration of Advanced LIGO (LIGO Laboratory & Shoemaker, 2010) and the B (Hild et al., 2008) and C (Hild et al., 2010) configuration for the Einstein telescope. These configurations are referred to as as AdvLIGO, ET-B and ET-C. In the low-frequency band the SNR of model m15fr is roughly equal to that of model s20s, for all the three detector configurations. The strong spiral SASI activity and the reduced high-frequency emission, due to dampening of PNS convection by rotation, leads to a larger ratio of $\mathrm{SNR_{low}}/\mathrm{SNR_{high}}$. Model m15r shows that one has to be careful when interpreting the ratio $\mathrm{SNR_{low}}/\mathrm{SNR_{high}}$. The reduction of the high-frequency emission and the presence of, intermediate and weak SASI activity leads to ratios of $\mathrm{SNR_{low}}/\mathrm{SNR_{high}}$ which are $\sim 15-25$ higher than those of model m15nr, for all three detector configurations. However, model m15nr clearly develops much stronger SASI activity than model m15r. Hence, an excess of power in the low-frequency band might not be a clear indicator of strong SASI activity.

At a distance of 10 kpc none of our models would be detectable with AdVLIGO. For the Einstein telescope the situation is significantly better. We estimate that model m15fr should be detectable out to distances of 75 kpc, while model m15nr and model m15r could be detected at $\sim$ 20 kpc and $\sim$ 30 kpc, respectively. The B configuration of the detector shows the most promise and it can effectively increase the detection distance limits by $\sim 35-60\%$.

7.6. Core bounce signal

Because the 3D simulations only start approximately 10 ms after core bounce, the expected GW signal associated with core bounce is not present in our waveforms (Fig. 7.6). The evolution of the models from the onset of core-collapse until the start of the 3D simulations was performed in 2D, the GW amplitudes from these 2D calculations are shown in Fig. 7.10. The amplitudes were calculated according to Eq. 2.40 and we only show the amplitudes of the two rotating models, since the non-rotating model does not emit any GWs. The flattening of the core that occurs during collapse leads to a positive, and steadily increasing amplitude. The abrupt halt of the collapse, followed by the expansion of the core leads to a sudden increase in the signal, and a subsequent sharp fall towards negative values. After bounce the waveforms show the typical large oscillations associated with the ring-down of the core, see for example Müller (1982), Finn & Evans (1990), Mönchmeyer et al. (1991), Yamada & Sato (1995), Zwerger & Müller (1997). When considering the factor $1/8\sqrt{15/\pi} \approx 0.27$ in Eq. 2.39, it is clear that the bounce signal from the two models is quite weak, even compared to the emission from the post-bounce phase.

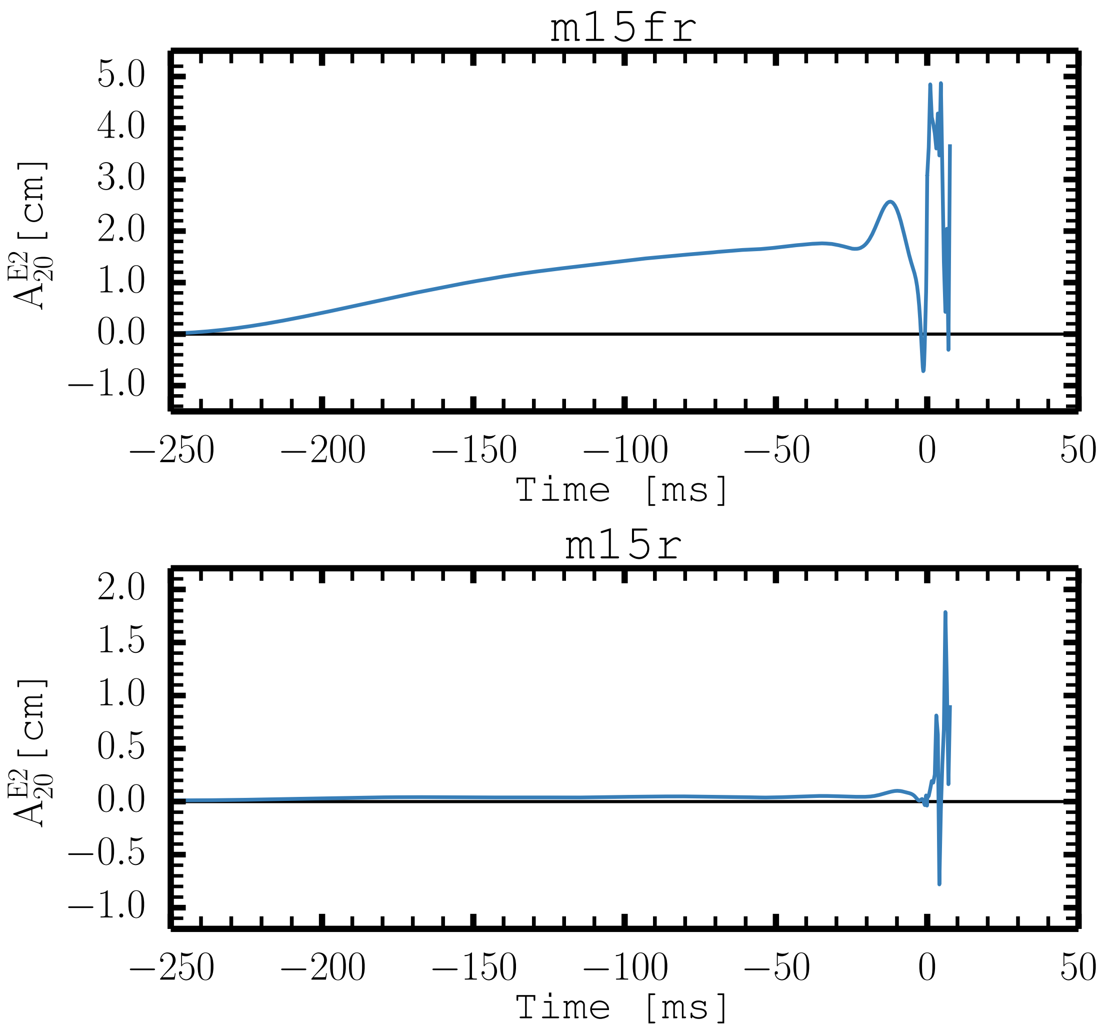

Figure 7.10.: The GW amplitudes from the 2D simulations of the collapse, and subsequent bounce of models m15fr (top), and m15r (bottom). The amplitudes were calculated according to Eq. 2.40.

7.7. Conclusion and discussion

In this chapter, we studied how progenitor rotation affects the GW signal of core collapse supernovae. We have not studied rapidly rotating models, but rather focused on the regime of moderate progenitor rotation. Our main findings are:

1. Moderate rotation does not change the frequency structure of the GW signal, compared to the signal from non-rotating models. We see the familiar two-component structure with a high-frequency and a low-frequency signal component.

2. We find that the high-frequency emission instigated by PNS convection is weaker in

the rotating models, because rotation has a stabilising effect on PNS convection and decreases the amount of energy dissipated in the overshooting region of the PNS. This becomes particularly apparent in model m15r, where we find a strong reduction of the GW amplitudes during a period of time when post-shock convection is weak. The generally weak amplitudes in this model reaffirm the fact that post-shock convection is a weak source of GW excitation, compared to PNS convection and SASI activity.

3. Of the three models presented in this chapter the fastest rotating model emits the strongest GW signal, because it develops the strongest spiral SASI mode. Based on the models presented here one should not conclude that the strength of the signal will increase with increasing progenitor rotation rate. The conclusion should instead be that the stronger the spiral mode of the SASI is the larger are the amplitudes of the GW signal. However, it remains unclear whether faster rotation leads to stronger SASI activity.

4. It should be emphasised that model m15r, where the rotation rate is exactly in accordance with stellar evolution calculations, shows the weakest GW signal.

5. Unlike model s20s, the GW signal of model m15fr decreases after the onset of shock revival. This reduction is due to the small contribution to the total signal from mass motions instigated by PNS convection.

Prior to this work, the GW signals of rapidly rotating models have been studied by several authors (Müller, 1982, Rampp et al., 1998, Shibata & Sekiguchi, 2005, Ott et al., 2005, Scheidegger et al., 2010, Kuroda et al., 2014, Takiwaki et al., 2016). A common feature of these studies is that they tend to predict rather strong emission of gravitational radiation. During the post-bounce phase, rapid rotation can lead to the development of novel flow patterns that are not observed in slowly/non-rotating models. Rampp et al. (1998) and Shibata & Sekiguchi (2005) found that very rapid rotation can lead to a bar-like deformation of the central core. In the somewhat slower rotating models of Ott et al. (2005), Kuroda et al. (2014), and Takiwaki et al. (2016) the development of a low-mode spiral instability was found. These asymmetric and rapidly rotating structures lead to strong GW emission. It is, however, not likely that a large part of the core collapse supernovae progenitors have rapidly rotating, or even moderately rotating, cores. Observations of pulsars put strong constraints on the rotation rate of core-collapse progenitors. It has been estimated that most pulsars are formed with rotation periods of a few tens to hundreds of milliseconds (Vranesevic et al., 2004, Popov & Turolla, 2012, Noutsos et al., 2013). The recent study by Kazeroni et al. (2017) concludes that the one armed-spiral instability (Ott et al., 2005, Kuroda et al., 2014, Takiwaki et al., 2016) is not able to spin down the PNS enough to make rapidly rotating progenitors compatible with the spin rate of young pulsars. Additionally, stellar evolution models which include the effects of magnetic fields predict slowly rotating stellar cores (Heger et al., 2005). Results from asteroseismology (Beck et al., 2012, Mosser et al., 2012) indicate that the cores of low-mass red giants rotate slower than what is expected from stellar evolution calculations (Cantiello et al., 2014, Deheuvels et al., 2014). According to results from asteroseismology, angular momentum loss due to stellar winds seems to play a bigger role than currently predicted by stellar evolution calculations (Cantiello et al., 2014).

The rotation rates of the two rotating models studied here are more along the lines of what is expected from state of the art stellar evolution calculations (Heger et al., 2005) and observations (Beck et al., 2012, Mosser et al., 2012, Popov & Turolla, 2012, Noutsos et al., 2013, Cantiello et al., 2014, Deheuvels et al., 2014). We find no quantitive difference in the GW signals from the rotating models, compared to those from the non-rotating models. We must, therefore, conclude that a stochastic signal with amplitudes of a few centimetres seems to be the generic core-collapse GW signal. Hench, moderate to low progenitor rotation will not significantly increase the detectability of GWs from core-collapse supernovae. Rotation can actually make it harder to detect the GW signal, because we find that rotation decreases the signal emitted due to PNS convection in model m15r and consequently makes the model harder to detect.

The fact that model m15nr, the non-rotating one, has an angular resolution that is two times lower (four versus two degrees) than that of the two other models makes it difficult to draw strong conclusions about how the low-frequency signal changes with increasing rotation. It is not clear why model m15nr develops strong SASI activity and model m15r does not. Previously, lower resolution has been found to both favour (Hanke et al., 2012) and suppress (Abdikamalov et al., 2015) the development of strong SASI activity. At the same time, it is also possible that rotation quenches the growth of SASI activity in model m15r (Kazeroni et al., 2017). This is an issue that will have to be resolved by a more systematic study, where the rotation rate and grid resolution is varied independently to study the impact of the individual effects. Another weakness of our study is that the three models all start from a spherically symmetric progenitor model. However, it is not realistic to expect the progenitor stars to be perfectly spherical symmetric objects. In fact, it has been found that asymmetries in the burning shells of the progenitor can influence the shock dynamics and even help to ensure a successful explosion (Burrows & Hayes, 1996, Fryer et al., 2004, Arnett & Meakin, 2011, Couch & Ott, 2013, Müller & Janka, 2015). Inhomogeneities in the stellar core could lead to a sizable emission of GWs during the collapse and right after core bounce. Thus, the long period of quiescence after bounce could be an artifact of the usage of spherical symmetric progenitors.

8. Conclusions

8.1. Summary and discussion

In this thesis, we have studied the GW signals from the accretion phase and the early explosion phase of core-collapse supernovae based on seven 3D multi-group neutrino hydrodynamics simulations. The seven models are based on four progenitors with ZAMS masses of $11.2M_{\odot}$, $20M_{\odot}$, $27M_{\odot}$, and $15M_{\odot}$, respectively. Two models, based on the $15M_{\odot}$ progenitor, included moderate initial rotation, while the rest of the models are non-rotating.

Broadly speaking, the GW signal from 3D simulations can be described as stochastic signals with amplitudes of few a centimetres, that consists of two distinct signal components. The first component, which is present in all of the signals, consists of emission at frequencies above 250 Hz (high-frequency emission). The typical frequency of this emission increases almost linearly as a function of time. The second component is only seen in the models where SASI activity develops. During phases of strong SASI activity emission in the range between 100 Hz and 200 Hz (low-frequency) emerges as a characteristic feature of the GW signal.

Low-frequency emission, during the accretion phase, originates from the global modulation of the accretion flow by the SASI. In the layer between the forming neutron star and the shock front, the SASI creates a coherent asymmetric mass distribution with a large quadrupole moment. The density perturbations induced by the SASI have the same temporal structure as the shock oscillations. This leads to the emission of GWs from the post-shock layer with a typical frequency which is proportional to the SASI frequency. Furthermore, strong low-frequency GWs emission is instigated when the anisotropic modulation of the accretion flow is felt by the PNS when matter is accreted onto the PNS. In the surface layer of the PNS, mass motions are forced by the strong downflows that result from SASI activity. The perturbation of the PNS surface leads to GW emission in a similar, but somewhat broader, frequency range as the emission from the post-shock layer. GW emission continues as the accreted matter is advected deeper into the PNS, since the density, and entropy perturbations are not completely erased by neutrino cooling. Density fluctuations around the one percent level are maintained even as the perturbations reaches the inner regions of the PNS. When propagating down into the interior of the PNS, these perturbations roughly maintain the frequency spectrum set by the SASI.

These conclusions are in line with the very recent study of Kuroda et al. (2016), where it is suggested that low-frequency emission is a fingerprint of SASI activity. However, we find that the exploding model s20s emits strong low-frequency GWs after the onset of shock expansion. During this time there is clearly no SASI activity. We trace this emission to the interior of the PNS and attribute it to the fact that the flow in the PNS convective layer transitions from a dipole dominated pattern to one where the quadrupole mode dominates. We speculate that this could result from changes in the accretion flow onto the PNS, or shifts in the entropy and electron fraction of the PNS.

By analysing two 2D simulations of the 27 $M_{\odot}$ progenitor, we find that low-frequency emission also exist in the 2D models. However, it is completely overshadowed by the high-frequency emission and has, therefore, not been emphasised in recent 2D studies (Marek et al., 2009, Murphy et al., 2009, Müller et al., 2013).

The typical frequency of the high-frequency component closely traces the Brunt-Väisälä-frequency of the outer layer of PNS, the roughly isothermal atmosphere layer between the PNS convection zone and the post-shock layer. In 2D this emission has been found to be the result downflows from the post-shock layer impinging onto the PNS surface (Marek et al., 2009, Murphy et al., 2009, Müller et al., 2013). However, in the 3D models studied in this work the high-frequency signal mostly originates from aspherical mass motions in the overshooting region of PNS. Convective plumes from the PNS convection zone overshoot into the convectively stable layer above. When these plumes are decelerated and overturned high-frequency GWs are emitted. Downflows from the post-shock layer contribute only weakly to the total high-frequency signal. We attribute the difference between 2D and 3D mainly to the inverse cascade of turbulent energy in 2D. In 2D energy cascades towards large and large scales which leads to the development of large downflows with impact larger velocities. These large flow structures effectively excite resonant g-mode oscillations in the PNS surface that give rise to GW emission. In 3D, braking of downflows by the forward turbulent cascade results in the fragmentation of large eddies into smaller structures and this suppress surface g-mode excitation. Furthermore, when large and medium sized eddies are broken up into smaller eddies this changes the spectrum of the turbulent mass motions in post-shock layer. This means that the spectrum of the of the forcing does not extend to high frequencies in 3D. Excitation of surface g-modes at their eigenfrequency, therefore, becomes ineffective.

In chapter 7 we studied the effect of moderate progenitor rotation, we studied three simulations of a 15 $M_{\odot}$ progenitor. Including moderate progenitor rotation does not significantly change the frequency structure or overall amplitudes of the GW signal, compared the signals from non-rotating models. We do, however, find that the high-frequency emission instigated by PNS convection is weaker in the two rotating models. Rotation acts as a stabiliser of the PNS convection layer and leads to a decrease in the amount of energy dissipated in the overshooting region PNS.

In regards to the signal strength as a function of the progenitor rotation rate, we do not find a clear trend of increasing signal strength with increasing initial rotation rate. Of the three simulations based on the 15 $M_\odot$ progenitor, the fastest rotating model emits the strongest GW signal. On the other hand, the non-rotating version emits a stronger signal than the slowest rotating model. The reason why the fastest rotating model emits the strongest GW signal is because it develops the strongest SASI oscillations. It is possible that rotation aids the development of the spiral SASI mode, but it remains unclear whether increasing the rotation rate always leads to stronger SASI activity.

The fastest rotating model emits the strongest GW signal because it develops the strongest spiral SASI mode. Based on the models presented here we can not conclude that the strength of the signal increase with increasing progenitor rotation rate. The conclusion should instead be that the strong SASI activity leads to strong GW emission. However, it remains unclear whether faster rotation leads to stronger SASI activity. In the linear regime, the growth rate of SASI modes has found to increase as a function of rotation (Yamasaki & Foglizzo, 2008, Blondin et al., 2017). However, in the non-linear regime, Kazeroni et al. (2017) does not find a monotonic connection between increasing rotation rate and the saturation amplitude SASI modes. The results of Kazeroni et al. (2017) indicates that SASI activity may decrease with increasing rotation rate, at least at low to moderate rotation rates.

We calculated the possibility of detecting the GW signals presented here. In general, we conclude that with current detectors it will be very difficult to detect the signals. The typical amplitudes are on the order of a few centimeters which are very small compared to that of other sources (such as black hole binary systems). With next generation instruments, like the Einstein telescope, detection should be possible for an event within the Milky way. Not only will it be possible to detect the events, but it will be possible to differentiate between models without and with low-frequency emission.

8.2. Uncertainties

The uncertainties of the gravitational wave signal are ultimately connected to the uncertainties of the underlying supernovae models. Recently we have seen the emergence of the first successful explosions in 3D simulations (Melson et al., 2015a;b, Lentz et al., 2015, Summa, 2017). These first explosion models prove that the delayed neutrino-driven explosion mechanism can produce explosions in full 3D. However, we are not yet at the point where 3D simulations robustly produce explosions. There are several sources of uncertainty in the current core-collapse simulations and it might be useful to divide these uncertainties into two categories.

The first category of uncertainties is related to the input physics. It has been shown that asymmetries in the burning layers of the stellar progenitor can influence the dynamics of the core-collapse. The simulations, on which the gravitational wave signal presented in this thesis are based on, all start from spherical symmetric progenitors (Burrows & Hayes, 1996, Fryer et al., 2004, Arnett & Meakin, 2011, Couch & Ott, 2013, Müller & Janka, 2015). Another example of uncertain input physics is the high-density equation of state. How matter behaves at super-nuclear densities and how neutrinos interact with the hot, and dense stellar matter is uncertain (Fischer et al., 2014, Lattimer & Prakash, 2016).

The second category concerns technical problems with the simulations. That is to say, the uncertainties connected to the current implementation of the physics included in the codes. While the ray-by-ray+ approximation implemented in PROMETHEUS-VERTEX (Rampp & Janka, 2002) is state of the art, it is still only an approximate solution of the full radiation problem. The one-dimensional approach of the ray-by-ray+ method fails to fully account for transverse fluxes and lateral radiation transport. Skinner et al. (2016) performed 2D simulations using both the ray-by-ray+ approximation and a multi-dimensional transport scheme. They found significantly different results for the two setups. Another technical problem is the issue of grid resolution. Currently, even the best resolved simulations can not hope to sufficiently resolve turbulence in the post-shock layer. It is still debate of how resolution affects the simulation outcome, and which the spatial resolution is needed to accurately simulate the core-collapse of a massive star. For a detailed discussion of the subject see Chapter 7 of Melson (2016) and references therein.

In their closing remarks Skinner et al. (2016) rather aptly write:

> *In fact, there is a rather long list of numerical challenges and code verification issues yet to be met collectively by the world's supernova modelers. The results of different groups are still too far apart to lend ultimate credibility to any one of them.*

What ultimately proves to be the solution to the explosion problem in 3D is not clear. Maybe a missing physical ingredient turns out to be the solution, or maybe there is a need for more accurate numerical solutions. A likely scenario is that the solution is a combination of the two.

Recent 3D models have shown that the neutrino-driven explosion mechanism can indeed produce successful explosion. (Melson et al., 2015b) presented a simulation of a non-rotating 20 $M_\odot$ progenitor. In this simulation the interaction rates of the neutrinos were slightly modified, resulting in a successful explosion. Similarly, a successful explosion was achieved with the help of rotation by (Summa, 2017). This indicates that we should not expect a drastic change in the dynamics of the core-collapse scenario, but rather small changes of the details in the simulations. Consequently, we should expect that the GW signals presented here, at least qualitatively, capture the essence of the gravitational radiation emitted by core collapse supernovae. Here we should mention the study of Müller et al. (2013), in which the authors found systematic shifts in the typical emission frequencies when comparing full GR simulations to pseudo-Newtonian, and Newtonian simulations. While the pseudo-Newtonian approximation of gravity that the simulations utilise is sufficient to capture the dynamics of the core-collapse, full GR simulations will be needed to determine the exact numerical value of the GW frequencies, and amplitudes.

8.3. Outlook

Future work in this field will, naturally, consist of improved predictions and studies of the GW signals produced by core-collapse simulations. As the simulations improve so will the predictions for the gravitational wave signals. We have in this thesis, rather crudely, estimated the possibilities for detecting the signals we studied. These estimates do not give us grounds for optimism. In current detectors, it would be difficult to detect even galactic events. However, it might be possible to develop more sophisticated algorithms and methods to enhance detection capabilities of the detectors. The bright electromagnetic signal associated with core-collapse supernovae gives us an advantage since it will be possible to pinpoint the location of the signal in the sky and with fairly high accuracy determine the time during which we should search for a signal in the data. In addition to the electromagnetic signal, for a closed event neutrinos will provide us with even tighter constraints on the time window. While the signal from core collapse supernova at first glance seems rather stochastic there is a significant degree of structure within the signal. This means that we can search for a particular type of signal in the detector data.

In terms of the understanding of the underlying processes responsible for GW emission in the simulations, the exact nature of the interaction between the SASI and the PNS is not yet fully understood. A more thorough, and rigorous study of how downflows affect the PNS surface is necessary to better understand both the low-frequency and the high-frequency emission. It will also be important to determine how the PNS convection layer is influenced by accretion and how this affects the high-frequency emission.

In this thesis, we have taken a first step towards studying the GW signals from slow/moderately rotating supernovae models in 3D. In the future, it will be necessary do perform more systematic studies of the effects of moderate progenitor rotation in order to determine exactly how the rotation rate of the progenitor affects the spiral SASI mode, and the GW signal.

A. List of conventions

Here we list the mathematical and physical conventions that are used in this thesis.

Indices: When Greek characters are used for indices it is understood that the indices runs from zero to three. When Latin characters are used the indices runs from one to three. We use the Einstein summation convention, which means that repeated indexes are implicitly summed over. For example, in the expression

$$f_\mu = x^i x_i y_\mu,$$

one should sum over i from one to three and $\mu = (0, 1, 2, 3)$

Kronecker-delta: The symbol δ^{ij} represents the Kronecker-delta, which is defined as follows

$$\delta^{ij} = \begin{cases} 1 & \text{if } i = j \\ 0 & \text{if } i \neq j \end{cases}$$

Flat space metric: we use the following signature for the metric tensor of flat space

$$\eta_{\mu\nu} = \begin{pmatrix} -1 & 0 & 0 & 0 \\ 0 & 1 & 0 & 0 \\ 0 & 0 & 1 & 0 \\ 0 & 0 & 0 & 1 \end{pmatrix}.$$

B. List of acronyms

GW	Gravitational wave
GWs	Gravitational waves
SASI	Standing accretion shock instability
1D	One-dimensional (Spherically symmetric)
2D	Two-dimensional (Axially symmetric)
3D	Three-dimensional (No symmetry assumptions)
EoS	Equation of state
ZAMS	Zero-age main-sequence

C. Acknowledgements

The work I have done during my time in Germany would not be possible if not for my supervisor Ewald Müller who gave me the chance to pursue my research interests. I have learned a lot from Ewald and for that I am grateful. The same can be said for Hans-Thomas Janka, who have taught me a lot about core-collapse supernovae.

The help and insights Bernhard Müller provided during the process of writing my first paper was invaluable, thank you Bernhard.

I must also thank Florian Hanke, Tobias Melson, and Alexander Summa. Without their simulations there would be no date for me to analyse.

All the members of the stellar group at MPA deserves a sincere thank you. The scientific discussion I have had with members of the group has always been very much appreciated and helpful. My colleagues have in general been more than happy to lend their expertise and help me solve problems.

I would also like to thank Michael Kachelrieß for encouraging me to apply for this PhD position.

The last three years have not been all work and no play, the best memories from München are those I have shared with the friends I have made here. You are all great. Special mention should be given to Durand, Andressa, Andy, Isabella, Dijana, Jeffrey, and Pierre. The 12.15 lunch group must also be mentioned, present and past members. Lunch has rarely been boring and I have enjoyed all the good debates.

I also appreciate the continued friendship of the friends I made in Trondheim. Even though we are spread all over the world, we still maintain regular contact and I really appreciated it.

Daria, thank you for your support and patience over the last few months. You are truly the best.

Lastly, I would like to thank my family for all the good advice and support they have given, it has been a great help to me.

Bibliography

Abbott B. P., et al., 2016, Physical Review Letters, 116, 061102

Abdikamalov E. B., Ott C. D., Rezzolla L., Dessart L., Dimmelmeier H., Marek A., Janka H.-T., 2010, Phys. Rev. D, 81, 044012

Abdikamalov E., et al., 2015, ApJ, 808, 70

Andresen H., Mueller B., Mueller E., Janka H.-T., 2016, preprint, (arXiv:1607.05199)

Arnett W. D., Meakin C., 2011, ApJ, 733, 78

Beck P. G., et al., 2012, Nature, 481, 55

Bethe H. A., 1990, Rev.~Mod.~Phys., 62, 801

Blanchet L., Damour T., Schaefer G., 1990, MNRAS, 242, 289

Blondin J. M., Mezzacappa A., 2006, ApJ, 642, 401

Blondin J. M., Mezzacappa A., 2007, Nature, 445, 58

Blondin J. M., Shaw S., 2007, ApJ, 656, 366

Blondin J. M., Mezzacappa A., DeMarino C., 2003, ApJ, 584, 971

Blondin J. M., Gipson E., Harris S., Mezzacappa A., 2017, ApJ, 835, 170

Brandt T. D., Burrows A., Ott C. D., Livne E., 2011, ApJ, 728, 8

Buras R., Rampp M., Janka H.-T., Kifonidis K., 2006a, A&A, 447, 1049

Buras R., Janka H.-T., Rampp M., Kifonidis K., 2006b, A&A, 457, 281

Burrows A., Hayes J., 1996, Physical Review Letters, 76, 352

Burrows A., Hayes J., Fryxell B. A., 1995, ApJ, 450, 830

Cantiello M., Mankovich C., Bildsten L., Christensen-Dalsgaard J., Paxton B., 2014, ApJ, 788, 93

Cappellaro E., Turatto M., 2001, in Vanbeveren D., ed., Astrophysics and Space Science Library Vol. 264, The Influence of Binaries on Stellar Population Studies. p. 199 (arXiv:astro-ph/0012455), doi:10.1007/978-94-015-9723-4˙16

Cerdá-Durán P., Faye G., Dimmelmeier H., Font J. A., Ibáñez J. M., Müller E., Schäfer G., 2005, A&A, 439, 1033

Chandrasekhar S., 1961, Hydrodynamic and Hydromagnetic Stability. Clarendon, Oxford

Colella P., Woodward P. R., 1984, extit J. Comp. Phys., 54, 174

Colgate S. A., White R. H., 1966, ApJ, 143, 626

Cordero-Carrión I., Cerdá-Durán P., Dimmelmeier H., Jaramillo J. L., Novak J., Gourgoulhon E., 2009, Phys. Rev. D, 79, 024017

Couch S. M., Ott C. D., 2013, ApJ, 778, L7

Couch S. M., Ott C. D., 2015, ApJ, 799, 5

Deheuvels S., et al., 2014, A&A, 564, A27

Dimmelmeier H., 2001, PhD thesis, Technische Universtiät München

Dimmelmeier H., Font J. A., Müller E., 2001, ApJ, 560, L163

Dimmelmeier H., Font J. A., Müller E., 2002a, A&A, 388, 917

Dimmelmeier H., Font J. A., Müller E., 2002b, A&A, 393, 523

Dimmelmeier H., Novak J., Font J. A., Ibáñez J. M., Müller E., 2005, Phys. Rev. D, 71, 064023:1

Dimmelmeier H., Ott C. D., Janka H.-T., Marek A., Müller E., 2007a, Phys. Rev. Lett., 98, 251101:1

Dimmelmeier H., Ott C. D., Janka H.-T., Marek A., Müller E., 2007b, preprint, astro-ph/0705.2675

Dimmelmeier H., Ott C. D., Marek A., Janka H.-T., 2008, Phys. Rev. D, 78, 064056:1

Dolence J. C., Burrows A., Murphy J. W., Nordhaus J., 2013, ApJ, 765, 110

Einfeldt B., 1988, extit SIAM J. Numer. Anal., 25, 294

Epstein R., 1978, ApJ, 223, 1037

Fernández R., 2010, ApJ, 725, 1563

Fernández R., 2015, MNRAS, 452, 2071

Finn L. S., 1989, in Evans C. R., Finn L. S., Hobill D. W., eds, Frontiers in Numerical Relativity. Cambridge University Press, Cambridge (UK), pp 126–145

Finn L. S., Evans C. R., 1990, ApJ, 351, 588

Fischer T., Hempel M., Sagert I., Suwa Y., Schaffner-Bielich J., 2014, European Physical Journal A, 50, 46

Flanagan É. É., Hughes S. A., 1998, Phys. Rev. D, 57, 4535

Foglizzo T., Scheck L., Janka H.-T., 2006, ApJ, 652, 1436

Foglizzo T., Galletti P., Scheck L., Janka H.-T., 2007, ApJ, 654, 1006

Foglizzo T., et al., 2015, PASA, 32, 9

Fryer C. L., Holz D. E., Hughes S. A., 2004, ApJ, 609, 288

Fryxell B., Arnett D., Müller E., 1991, ApJ, 367, 619

Fuller J., Klion H., Abdikamalov E., Ott C. D., 2015, MNRAS, 450, 414

Goldreich P., Kumar P., 1990, ApJ, 363, 694

Gossan S. E., Sutton P., Stuver A., Zanolin M., Gill K., Ott C. D., 2016, Phys. Rev. D, 93, 042002

Guilet J., Foglizzo T., 2012, MNRAS, 421, 546

Hamacher D. W., 2014, Journal of Astronomical History and Heritage, 17, 161

Hanke F., 2014, PhD thesis, Technische Universtiät München

Hanke F., Marek A., Müller B., Janka H.-T., 2012, ApJ, 755, 138

Hanke F., Müller B., Wongwathanarat A., Marek A., Janka H.-T., 2013, ApJ, 770, 66

Hayama K., Kuroda T., Kotake K., Takiwaki T., 2015, Phys. Rev. D, 92, 122001

Heger A., Woosley S. E., Spruit H. C., 2005, ApJ, 626, 350

Herant M., Benz W., Hix W. R., Fryer C. L., Colgate S. A., 1994, ApJ, 435, 339

Hild S., Chelkowski S., Freise A., 2008, preprint, (arXiv:0810.0604)

Hild S., Chelkowski S., Freise A., Franc J., Morgado N., Flaminio R., DeSalvo R., 2010, Classical and Quantum Gravity, 27, 015003

Ho P. Y., 1962, Vistas in Astronomy, 5, 127

Hoyle F., Fowler W. A., 1960, ApJ, 132, 565

Iwakami W., Kotake K., Ohnishi N., Yamada S., Sawada K., 2008, ApJ, 678, 1207

Iwakami W., Kotake K., Ohnishi N., Yamada S., Sawada K., 2009, ApJ, 700, 232

Iwakami W., Nagakura H., Yamada S., 2014, ApJ, 793, 5

Janka H.-T., 1999, ,

Janka H.-T., 2012, Annual Review of Nuclear and Particle Science, 62, 407

Janka H.-T., Müller E., 1996, A&A, 306, 167

Janka H.-T., Kifonidis K., Rampp M., 2001, in Blaschke D., Glendenning N. K., Sedrakian A., eds, Lecture Notes in Physics, Berlin Springer Verlag Vol. 578, Physics of Neutron Star Interiors. p. 363 (arXiv:astro-ph/0103015)

Janka H.-T., Melson T., Summa A., 2016, preprint, (arXiv:1602.05576)

Kageyama A., Sato T., 2004, Geochemistry, Geophysics, Geosystems, 5, n/a

Kazeroni R., Guilet J., Foglizzo T., 2016, MNRAS, 456, 126

Kazeroni R., Guilet J., Foglizzo T., 2017, preprint, (arXiv:1701.07029)

Kifonidis K., Plewa T., Janka H.-T., Müller E., 2003, A&A, 408, 621

Kotake K., Yamada S., Sato K., 2003, Phys. Rev. D, 68, 044023

Kotake K., Sato K., Takahashi K., 2006, Reports on Progress in Physics, 69, 971

Kotake K., Iwakami W., Ohnishi N., Yamada S., 2009, ApJ, 697, L133

Kotake K., Iwakami-Nakano W., Ohnishi N., 2011, ApJ, 736, 124

Kraichnan R. H., 1967, Physics of Fluids, 10, 1417

Kuroda T., Takiwaki T., Kotake K., 2014, Phys. Rev. D, 89, 044011

Kuroda T., Kotake K., Takiwaki T., 2016, ArXiv e-prints,1605.09215,

LIGO Laboratory Shoemaker D., 2010, Advanced LIGO anticipated sensitivity curves, `https://dcc.ligo.org/LIGO-T0900288/public`

Lattimer J. M., Prakash M., 2016, Phys. Rep., 621, 127

Lattimer J. M., Swesty F. D., 1991, extit Nucl.~Phys.~A, 535, 331

Lecoanet D., Quataert E., 2013, MNRAS, 430, 2363

Lentz E. J., et al., 2015, ApJ, 807, L31

Liebendörfer M., Whitehouse S. C., Fischer T., 2009, ApJ, 698, 1174

Logue J., Ott C. D., Heng I. S., Kalmus P., Scargill J. H. C., 2012, Phys. Rev. D, 86, 044023

Lund T., Marek A., Lunardini C., Janka H., Raffelt G., 2010, Phys. Rev. D, 82, 063007

Maggiore M., 2007, Gravitational Waves: Volume 1: Theory and Experiments. Oxford University Press

Marek A., Dimmelmeier H., Janka H.-T., Müller E., Buras R., 2006, A&A, 445, 273

Marek A., Janka H., Müller E., 2009, A&A, 496, 475

Melson T., 2016, PhD thesis, Technische Universtiät München

Melson T., Janka H.-T., Marek A., 2015a, ApJ, 801, L24

Melson T., Janka H.-T., Bollig R., Hanke F., Marek A., Müller B., 2015b, ApJ, 808, L42

Minkowski R., 1941, PASP, 53, 224

Mönchmeyer R., Schaefer G., Müller E., Kates R. E., 1991, A&A, 246, 417

Mosser B., et al., 2012, A&A, 548, A10

Müller E., 1982, A&A, 114, 53

Müller B., 2015, MNRAS, 453, 287

Müller E., Janka H.-T., 1997, A&A, 317, 140

Müller B., Janka H.-T., 2014, ApJ, 788, 82

Müller B., Janka H.-T., 2015, MNRAS, 448, 2141

Müller E., Fryxell B., Arnett D., 1991, A&A, 251, 505

Müller B., Janka H., Dimmelmeier H., 2010, ApJS, 189, 104

Müller E., Janka H.-T., Wongwathanarat A., 2012a, A&A, 537, A63

Müller B., Janka H.-T., Marek A., 2012b, ApJ, 756, 84

Müller B., Janka H.-T., Heger A., 2012c, ApJ, 761, 72

Müller B., Janka H.-T., Marek A., 2013, ApJ, 766, 43

Murphy J. W., Burrows A., 2008a, ApJS, 179, 209

Murphy J. W., Burrows A., 2008b, ApJ, 688, 1159

Murphy J. W., Ott C. D., Burrows A., 2009, ApJ, 707, 1173

Murphy J. W., Dolence J. C., Burrows A., 2013, ApJ, 771, 52

Nakamura T., Oohara K., 1989, in Evans, C. R., Finn, L. S., & Hobill, D. W. ed., Frontiers in Numerical Relativity. Cambridge University Press, pp 254–280

Nakamura K., Kuroda T., Takiwaki T., Kotake K., 2014, ApJ, 793, 45

Nordhaus J., Brandt T. D., Burrows A., Almgren A., 2012, MNRAS, 423, 1805

Nordlund Å., Stein R. F., Asplund M., 2009, Living Reviews in Solar Physics, 6, 2

Noutsos A., Schnitzeler D. H. F. M., Keane E. F., Kramer M., Johnston S., 2013, MNRAS, 430, 2281

Novikov I. D., 1976, Soviet Astronomy, 19, 398

Obergaulinger M., Aloy M. A., Müller E., 2006, A&A, 450, 1107

Ohnishi N., Kotake K., Yamada S., 2006, ApJ, 641, 1018

Ohnishi N., Iwakami W., Kotake K., Yamada S., Fujioka S., Takabe H., 2008, Journal of Physics Conference Series, 112, 042018

Oohara K.-i., Nakamura T., Shibata M., 1997, Progress of Theoretical Physics Supplement, 128, 183

Ott C. D., 2007, PhD thesis, Albert-Einstein-Institut, Max-Planck-Institut für Gravitationsphysik; Universität Potsdam

Ott C. D., Burrows A., Livne E., Walder R., 2004, ApJ, 600, 834

Ott C. D., Ou S., Tohline J. E., Burrows A., 2005, ApJ, 625, L119

Ott C. D., Dimmelmeier H., Marek A., Janka H.-T., Hawke I., Zink B., Schnetter E., 2007, Phys. Rev. Lett., 98, 261101:1

Ott C. D., et al., 2012, Phys. Rev. D, 86, 024026

Plewa T., Müller E., 1999, A&A, 342, 179

Popov S. B., Turolla R., 2012, Ap&SS, 341, 457

Quirk J. J., 1994, extit Int.~J.~Num.~Meth.~in~Fluids, 18, 555

Rampp M., Janka H.-T., 2002, A&A, 396, 361

Rampp M., Müller E., Ruffert M., 1998, A&A, 332, 969

Reisswig C., Ott C. D., Sperhake U., Schnetter E., 2011, Phys. Rev. D, 83, 064008

Roberts L. F., Ott C. D., Haas R., O'Connor E. P., Diener P., Schnetter E., 2016, preprint, (arXiv:1604.07848)

Saenz R. A., Shapiro S. L., 1978, ApJ, 221, 286

Saenz R. A., Shapiro S. L., 1979, ApJ, 229, 1107

Saenz R. A., Shapiro S. L., 1981, ApJ, 244, 1033

Saijo M., 2005, Phys. Rev. D, 71, 104038

Sathyaprakash B., et al., 2012, Classical and Quantum Gravity, 29, 124013

Scheck L., Kifonidis K., Janka H.-T., Müller E., 2006, A&A, 457, 963

Scheck L., Janka H.-T., Foglizzo T., Kifonidis K., 2008, A&A, 477, 931

Scheidegger S., Fischer T., Whitehouse S. C., Liebendörfer M., 2008, A&A, 490, 231

Scheidegger S., Whitehouse S. C., Käppeli R., Liebendörfer M., 2010, Classical and Quantum Gravity, 27, 114101

Shapiro S. L., 1977, ApJ, 214, 566

Shen C. S., 1969, Nature, 221, 1039

Shibata M., Sekiguchi Y.-I., 2004, Phys. Rev. D, 69, 084024:1

Shibata M., Sekiguchi Y.-I., 2005, Phys. Rev. D, 71, 024014:1

Skinner M. A., Burrows A., Dolence J. C., 2016, ApJ, 831, 81

Strang G., 1968, SIAM Journal on Numerical Analysis, 5, 506

Summa A., 2017, In preparation, Private communication

Takiwaki T., Kotake K., 2011, ApJ, 743, 30

Takiwaki T., Kotake K., Suwa Y., 2012, ApJ, 749, 98

Takiwaki T., Kotake K., Suwa Y., 2014, ApJ, 786, 83

Takiwaki T., Kotake K., Suwa Y., 2016, MNRAS, 461, L112

Tamborra I., Hanke F., Müller B., Janka H.-T., Raffelt G., 2013, Physical Review Letters, 111, 121104

Tamborra I., Raffelt G., Hanke F., Janka H.-T., Müller B., 2014a, Phys. Rev. D, 90, 045032

Tamborra I., Hanke F., Janka H.-T., Müller B., Raffelt G. G., Marek A., 2014b, ApJ, 792, 96

The LIGO Scientific Collaboration et al., 2015, Classical and Quantum Gravity, 32, 074001

Thompson C., 2000, ApJ, 534, 915

Thuan T. X., Ostriker J. P., 1974, ApJ, 191, L105

Viallet M., Meakin C., Arnett D., Mocák M., 2013, ApJ, 769, 1

Vranesevic N., et al., 2004, ApJ, 617, L139

Wilson J. R., 1985, in Centrella J. M., Leblanc J. M., Bowers R. L., eds, Numerical Astrophysics. pp 422–434

Wongwathanarat A., Hammer N. J., Müller E., 2010a, A&A, 514, A48

Wongwathanarat A., Janka H., Müller E., 2010b, ApJ, 725, L106

Wongwathanarat A., Janka H.-T., Müller E., 2013, A&A, 552, A126

Wongwathanarat A., Müller E., Janka H.-T., 2015, A&A, 577, A48

Woosley S. E., Heger A., 2007, Phys. Rep., 442, 269

Woosley S. E., Heger A., Weaver T. A., 2002, extit Rev.~Mod.~Phys., 74, 1015

Yakunin K. N., et al., 2010, Classical and Quantum Gravity, 27, 194005

Yakunin K. N., et al., 2015, Phys. Rev. D, 92, 084040

Yakunin K. N., et al., 2017, preprint, (arXiv:1701.07325)

Yamada S., Sato K., 1995, ApJ, 450, 245

Yamada S., Sawai H., 2004, ApJ, 608, 907

Yamasaki T., Foglizzo T., 2008, ApJ, 679, 607

Zwerger T., Müller E., 1997, A&A, 320, 209